The impact of weather and climate variability upon estimates of ice-sheet mass balance from satellite radar altimeters

Submitted by

Robert J. Arthern

for the degree of Ph. D. of the University of London

1997

Abstract

Satellite radar altimeters are being used to measure ice sheet mass balance by detecting changes in surface elevation. Climate variability may cause errors in these measurements by altering the structure of the snow and the penetration of the radar pulse. Three parameters describe the microwave penetration and scattering; the surface backscatter $\sigma^{o}_{\mathrm{surf}}$, the volume backscatter $\sigma^{o}_{\mathrm{vol}}$, and the extinction coefficient k_e. These parameters were measured in Antarctica using ERS-1 altimeter data and compared with satellite radiometer data, glaciological observations, and a scattering model, to determine the sensitivity of the radar echo to the snow structure. Echo distortion, caused by topographic undulations, limits the accuracy of $\sigma^{o}_{\mathrm{surf}}$, $\sigma^{o}_{\mathrm{vol}}$ and k_e. In flatter regions though, the retrieval shows that reflections at layer interfaces beneath the surface generally account for most of the backscatter. Surface reflection can cause 60% of the backscatter in low accumulation regions prone to surface crusts. Only about 1% of the total backscatter arises from volume scattering by snow grains, although this mechanism controls the magnitude of k_e. Only $\sigma^{o}_{\mathrm{surf}}$ changes on monthly timescales, through changes in the roughness and density of the surface snow. However, because of an anisotropy in snow structure in windy regions, k_e and $\sigma^{o}_{\mathrm{vol}}$ depend upon the direction of travel of the satellite, which may vary between measurements. The sensitivity of k_e and $\sigma^{o}_{\mathrm{vol}}$ to changes in accumulation rate, temperature and density is investigated, and used to calculate the errors in the mass balance which might be expected for measurement intervals of many years, and also to map accumulation rates on the plateau. By changing the rate of snow compaction, the meteorological boundary conditions can also alter the average density of the ice sheets, causing further errors in the mass balance measurement. A numerical model of time-variant snow densification was used to calculate the errors from this source. Overall, it is concluded that satellite radar altimeters are probably capable of reducing the present uncertainties in ice-sheet mass balance, but it will be essential to accompany each measurement with investigations into the climate during the measurement interval, and the preceding decades, to be certain. Similarly, it will be essential to monitor the scattering behaviour of the snow throughout each measurement.

Acknowledgements

This work was in part supported by the U.K. Natural Environmental Research Council, under grant GR3/8748. I would also like to thank Professor Wingham for his supervision, Professor Winebrenner, for offering the radiative transfer model used in chapter 3 (and much useful advice besides), Andrew Ridout for the results shown in figure 1.1 and 1.2, and Judith Proud, for some painstakingly collected data used in chapter 2. The work described here would not have been possible without the efficient system administration of Colin Johnson and his predecessor David Palmer. The greatest thanks are reserved for my family and friends for their support throughout.

Contents

1 Introduction

1.1 The importance of ice sheet mass balance. 6
1.2 Earth observation and the geodetic method. 8
1.3 Outstanding problems with the geodetic method. 9

2 Measurements of microwave scattering in Antarctica

2.1 Introduction to scattering. 15
2.2 The altimeter echo and the distribution of scattering verses depth. 17
2.3 The ERS-1 radar altimeter. 29
2.4 Recovering snow scattering parameters from ERS-1 altimeter data. 33
2.5 An assessment of the likely errors in the scattering parameters. 42
2.6 Results from Antarctica. 54
2.7 Chapter summary 58

3 The impact of changes in scattering upon the geodetic method.

3.1 Introduction to scattering changes. 60
3.2 Comparison of scattering parameters with satellite microwave radiometer data. 60
3.3 Comparison of scattering parameters with direct glaciological observations. 64
3.4 A numerical model of scattering from snow. 70
3.5 The impact of scattering upon elevation change measurements. 80
3.6 Chapter summary. 104

4 Time variant snow densification and its impact upon the geodetic method

4.1 Introduction to densification. 106
4.2 Modelling the densification of snow. 106
4.3 Numerical simulations of time variant snow densification. 109
4.4 Numerical results for Byrd station, Antarctica and Site 2, Greenland. 113
4.5 Limitations of the model. 120
4.6 Chapter summary. 121

5 Overall summary and conclusions.

5.1 Summary. 123
5.2 Conclusions. 124
5.3 Limitations and further work. 126

References 129

Appendices

Appendix A: Analytical solution to equation 2.2.37 for Gaussian Antenna pattern. 139
Appendix B: Measuring accumulation rate from space. 143
Appendix C: The transformation of equations (4.2.1) - (4.2.4). 148
Appendix D: The constitutive relationship for snow. 151

List of figures

Figure. Page
1.1 Errors in the elevation measurement. 11
1.2 The elevation and backscatter anisotropy. 11

2.1 Microwave scattering mechanisms in snow. 16
2.2 A coordinate system for altimetry. 18
2.3 The boresight direction. 18
2.4 ERS-1 waveform data. 31
2.5 The reconstructed echo. 31
2.6 An average echo. 36
2.7 The deconvolution and a non-linear fit. 36
2.8 Instrumental fluctuations in the echo. 44
2.9 Simulated ice sheet topography. 50
2.10 Simulated average echo from topographic surface. 51
2.11 The distorting effect of topography. 52
2.12 Spatial variations in surface backscatter. 56
2.13 Spatial variations in volume backscatter. 56
2.14 Spatial variations in the extinction coefficient. 57
2.15 Testing the fit of the scattering model. 57

3.1 The reflectivity at 19 GHz frequency. 62
3.2 The polarisation of 19 GHz emissivity. 62
3.3 The route of the SPQMLT3 traverse. 65
3.4 Snow conditions along the traverse. 66
3.5 Scattering parameters along the traverse. 67
3.6 Simulated density and grain size profiles. 74
3.7 Simulated microwave propagation and scattering. 75
3.8 The effect of roughness and density upon surface reflection. 77
3.9 The change in backscatter between 1992 and 1993. 77
3.10 The change in the deconvolution near Plateau station. 81
3.11 The change in scattering parameters between 1992 and 1993. 82
3.12 The change in the deconvolution in West Antarctica. 84
3.13 The anisotropy in backscatter. 86
3.14 The anisotropy in the deconvolution. 87
3.15 The anisotropy in scattering parameters. 88
3.16 Scatterometer measurements from Antarctica. 90
3.17 Variations of extinction with depth. 92
3.18 Simulated echoes for a change in surface reflection. 96
3.19 Simulated echoes for a change in extinction 96
3.20 Observations of extinction coefficient and grain growth rate. 101
3.21 Simulations of extinction coefficient and grain growth rate. 101

4.1 The density and strain rate profiles from Byrd. 112
4.2 The strain rate profile from Site 2. 112
4.3 The response of the density profile to a step change in temperature. 115
4.4 The response to a step change in accumulation rate. 115
4.5 The response to a step change in surface density. 116
4.6 The response to randomly varying accumulation rate. 118

B.1 Satellite-derived and directly measured accumulation rate. 144
B.2 Spatial variations in satellite derived accumulation rate. 145
B.3 Spatial variations in directly measured accumulation rate. 145

1. Introduction

1.1 The importance of ice sheet mass balance.

Nowadays, only two large ice sheets exist on Earth. They cover Greenland and Antarctica, and together account for 99% of the world's ice - the remainder exists mostly as smaller ice caps and mountain glaciers. At present, the Antarctic ice sheet covers an area of some 10^7 km^2, with an average thickness of about 3 km, giving it a volume of 3×10^7 km^3, and mass of order 3×10^{19} kg. For Greenland, the corresponding statistics are; area 2×10^6 km^2, thickness 2 km, volume 3×10^6 km^3 and mass 3×10^{18} kg (Warrick et al. 1995).

Changes in the mass of ice stored in Antarctica and Greenland will affect global sea levels. The available estimates of ice accumulation and loss suggest that Greenland contributes between 0.1 and 0.4 mm yr^{-1} to eustatic sea level rise (Warrick and Oerlemans 1990; Warrick et al. 1995). Conversely, there is evidence to suggest that the Antarctic ice sheet is growing, withdrawing up to 1 mm yr^{-1} from the oceans (Bentley and Giovinetto 1991; Jacobs et al. 1992). Even when the effects of thermal expansion and losses from small glaciers are taken into account, the observed sea level rise, placed at 2.4 ± 0.9 mm yr^{-1} by Peltier and Tushingham (1991), is larger than the measured contributions from Greenland and Antarctica would predict (Warrick et al. 1990). It is possible that the contribution to sea level rise from the polar ice sheets has been underestimated; whether this is the case or not will only be revealed by more accurate measurements of their mass balance.

The mass balance of the ice sheets may change in future. Coupled atmosphere and ocean general circulation models predict that within the next century, a warming of 1 to 2 K over Antarctica and 2 to 4 K over Greenland may be realised in response to increasing concentrations of infra-red absorbing gases in the atmosphere (Murphy and Mitchell 1995). Energy balance calculations for similar warming predictions show that this would increase ablation from the Greenland ice sheet, causing an estimated 60 mm sea level rise over the century, in addition to the increase from thermal expansion of the oceans (van der Wal and Oerlemans 1994). On timescales of a century or so, the loss of ice from East Antarctica is relatively insensitive to temperature increases, because temperatures are presently far below the melting point, and ice flow velocities, which determine the rate of mass loss through iceberg calving, only respond to temperature changes on timescales of many thousands of years. However, warmer temperatures would cause melting on the floating ice shelves bordering West Antarctica, perhaps precipitating their collapse. This would not affect sea level directly, because the ice shelves are already floating. However, it may cause additional losses from the inland ice if the ice shelves are currently impeding its flow (Warrick et al. 1995). Because West Antarctica rests upon bedrock below sea level it may also suffer more rapid deglaciation in response to sea level rise or increases in ocean temperatures (Huybrechts 1990).

In a warmer climate, increased ablation from the ice sheets may be offset by higher accumulation rates over Antarctica and the interior of Greenland, where precipitation is often assumed to increase with temperature (Giovinetto et al. 1990). However, precipitation is also influenced by atmospheric circulation (Bromwich 1995; Kaspner et al. 1995), and it is far from clear how this will change if global temperatures rise. A negative feedback from increased ice accumulation certainly cannot be relied upon when estimating the effect of global warming upon future sea level rise.

To summarise, the present state of balance of the ice sheets is poorly constrained. It seems likely that the mass balance of both ice sheets will change over the next century, but it is not clear whether this will tend to increase or decrease sea levels. To alleviate this uncertainty, more accurate measurements of ice sheet mass balance are needed, and should be repeated frequently to monitor any changes which occur.

1.2 Earth observation and the geodetic method.

The present large uncertainties in mass balance are caused by poor spatial and temporal sampling in measurements of ice accumulation from the atmosphere and ice wastage to the oceans (Bentley et al. 1991). Accumulation rate measurements come from a sparse network of permanently manned stations, mostly located in coastal regions, and from occasional traverses across the interior. Losses from the grounded portions of the ice sheets are obtained from measurements of the ice flux across their perimeter. In each case, the sheer size of the ice sheets ensures as much as 60% of the ice accumulation and loss is completely unobserved (Bentley et al. 1991). Furthermore, it may take decades to collate enough field measurements for even a single estimate of the mass balance, so it is impractical to measure how the mass balance is changing from year to year.

A faster and more systematic means of monitoring mass balance is provided by Earth observation satellites, which offer virtually complete coverage of the ice sheets in a matter of weeks. Rather than attempt to measure accumulation and wastage separately, a different approach has been taken: repeated surveys of the surface elevation are made using satellite radar altimeters, and the change in mass is inferred from the measured volume change (this is termed the geodetic method). The present uncertainties in mass balance are equivalent to changes in surface elevation of about ± 25 cm yr^{-1} for Greenland and about ± 5 cm yr^{-1} for Antarctica. The central question answered by this thesis is whether it is realistic to expect radar altimetry to reduce these uncertainties.

The first application of the geodetic method used the Seasat radar altimeter, operational for three months in 1978, and the Geosat radar altimeter, operational from 1985 to 1989. Zwally et al. (1989) reported an elevation increase of 23 ± 6 cm yr^{-1} for the southern tip of the Greenland ice sheet. This figure is much larger than estimates from field surveys (Reeh and Gundestrup 1985; Kostecka and Whillans 1988) and several possible reasons for this discrepancy have been suggested and ruled out (Wingham 1995); these include orbit error (Douglas et al. 1990; Zwally et al. 1990), random mass fluctuations through the temporal variability of accumulation rate (van der Veen 1993) and variations in melting (Braithwaite et al. 1994). Errors in the reference geoids now appear a likely explanation for the anomaly: reanalysis of the same data using a consistent geoid for the Seasat and Geosat data reduces Zwally's estimate to 7 cm yr^{-1}, much closer to the field observations (Davis 1995) .

Only the margins of Antarctica and the Southern tip of Greenland were surveyed by Seasat and Geosat, which covered latitudes between 72° S and 72° N. The ERS-1 satellite, launched in 1991, has extended this range to ±81°, covering most of Antarctica and virtually all of Greenland. The ERS-2 satellite, the successor to ERS-1, was launched in 1995, and a third satellite, Envisat, is scheduled for launch in 2003. The total measurement interval afforded by these satellites should approach 20 years. The ERS-1, ERS-2 and Envisat radar altimeters support an 'ice' mode, giving better performance over the undulating ice sheets than Seasat and Geosat, which were designed for oceanographic applications. This feature, together with the improved coverage and the long observation interval, makes the ERS-1, ERS-2 and Envisat satellites the most likely source of more accurate measurements of ice sheet mass balance.

1.3 Outstanding problems with the geodetic method

Although the large elevation change measured by Zwally et al. (1989) may now be attributed to geoid errors, ERS-1 data have recently revealed further problems with the geodetic method. Before considering these, it is useful to give some details of the processing applied to the data to reveal the elevation changes.

During each 35 day repeat cycle ERS-1 performs 501 orbits of the Earth, laying down a network of ground tracks. These tracks are described as ascending (increasing latitude) or descending (decreasing latitude). Elevation changes are measured at satellite crossover points, where ascending and descending tracks cross. Measurements from a repeat cycle starting at time t are compared with those from a repeat cycle starting at a later time $t+T$ so there may be many months or even years between the two elevation measurements forming a crossover.

Denoting the measured elevations by h, and using the subscripts asc and $desc$ to identify ascending and descending tracks respectively, two types of crossover differences may be formed: $h_{asc}(t+T)-h_{desc}(t)$, and $h_{desc}(t+T)-h_{asc}(t)$. Previous algorithms for determining the elevation change did not make any distinction between these two types of crossovers (Zwally et al. 1989). However Ridout (manuscript in preparation) has shown that a better cancellation of errors is achieved using the following expression to provide an estimate of the elevation change

$$\Delta_h = \frac{1}{2}\left(\overline{\left[h_{asc}(t+T)-h_{desc}(t)\right]}+\overline{\left[h_{desc}(t+T)-h_{asc}(t)\right]}\right) \tag{1.1}$$

In equation (1.1) the overbars denote separate averages of all available crossover differences of each type within a region of the ice sheet some 100 km across.

Figures 1.1 and 1.2, which show unexplained anomalies in the elevation measurement, were provided by A.L. Ridout. Figure 1.1a shows spatial variations in Δ_h across Antarctica for repeat cycles in July 1993 and July 1994. Even though the observation interval T is only one year, apparent elevation changes larger than 30 cm are observed. This is much larger than the values of 5 cm or so which would be anticipated from current mass balance estimates. In many areas, the apparent elevation change exceeds the thickness of the annual snow accumulation by a factor

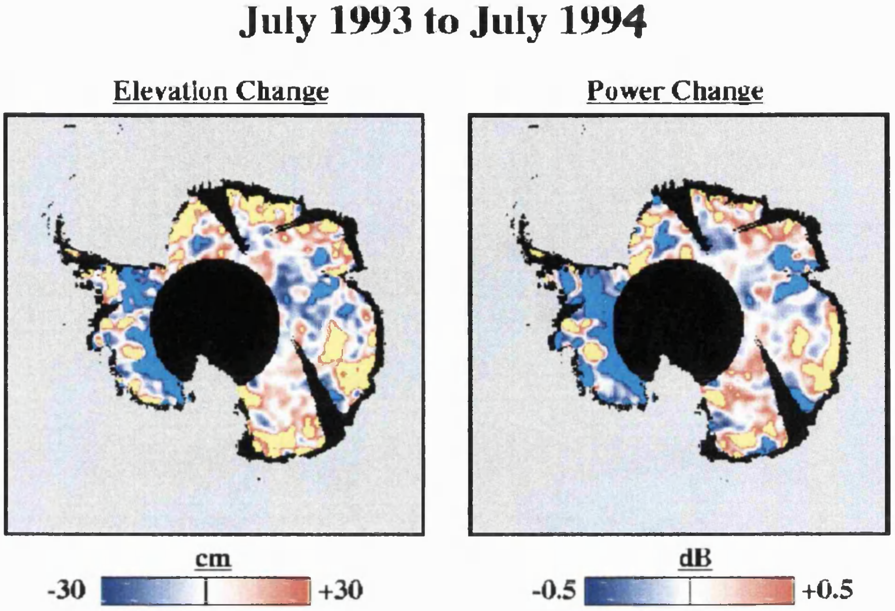

Figure 1.1a (left) the apparent change in elevation of the Antarctic ice sheet measured between July 1993 and July 1994 using the ERS-1 radar altimeter. The elevation change was calculated using equation (1.1). Areas where no data were available are shown in black.
Figure 1.1b (right) the change in backscatter over the same interval calculated using equation (1.2). Note the correlation with the elevation changes.
Provided by A.L. Ridout in advance of publication.

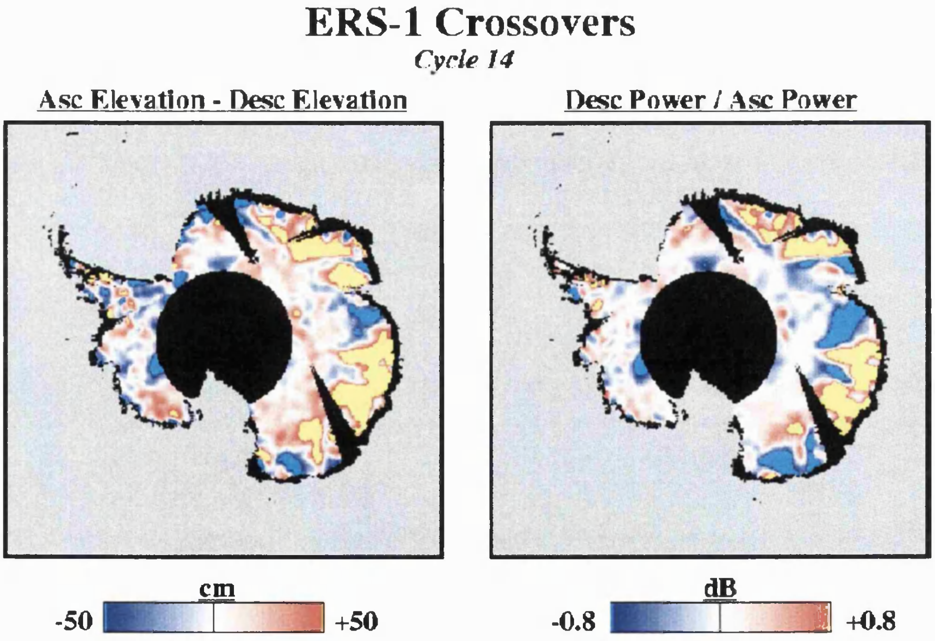

Figure 1.2a (left) the discrepancy between elevations measured on ascending and descending tracks at crossover points, calculated using equation (1.3).
Figure 1.2b (right) the discrepancy between backscatter measured on ascending and descending tracks using equation (1.4).
Provided by A.L. Ridout in advance of publication.

of two or three - it is hard to believe that such large changes truly reflect the mass balance of these regions.

Figure 1.1b shows the backscatter σ^0, measured by ERS-1, processed in exactly the same way as the elevation measurements. i.e.

$$\Sigma_h = \frac{1}{2}\left(\overline{\left[\sigma^0_{asc}(t+T) - \sigma^0_{desc}(t)\right]} + \overline{\left[\sigma^0_{desc}(t+T) - \sigma^0_{asc}(t)\right]}\right) \tag{1.2}$$

The correlation between Δ_h and Σ_h provides strong evidence that the anomaly in the elevation change measurement is caused by changes in the scattering properties of the surface. This is quite plausible because the microwaves employed by the ERS-1 radar altimeter penetrate several metres into the snow, causing a bias in the elevation measurement (Ridley and Partington 1988). If the distribution of backscatter with depth changes, an erroneous elevation change will be recorded.

Another discrepancy in the measured elevations is revealed by the quantity

$$\Delta_0 = \frac{1}{2}\left(\overline{\left[h_{asc}(t) - h_{desc}(t)\right]} + \overline{\left[h_{desc}(t+T) - h_{asc}(t+T)\right]}\right) \tag{1.3}$$

which provides a measure of the repeatability of the elevation measurements (very little elevation change should occur between measurements within the same 35 day repeat cycle). Figure 1.2a shows the spatial variation of Δ_0 across Antarctica. There are clearly regions of the ice-sheet where there is a systematic bias between elevations measured on ascending tracks compared to those measured on descending tracks.

Again, the backscatter can be processed in the same way, giving the quantity

$$\Sigma_0 = \frac{1}{2}\left(\overline{\left[\sigma^0_{asc}(t) - \sigma^0_{desc}(t)\right]} + \overline{\left[\sigma^0_{desc}(t+T) - \sigma^0_{asc}(t+T)\right]}\right) \tag{1.4}$$

which is shown in figure 1.2b. The strong correlation between Δ_0 and Σ_0 suggests that this anomaly in the elevation measurements is also connected with the scattering properties of the surface. In the remainder of this thesis, the term anisotropy is used to refer to any measurement which differs between ascending and descending tracks - so Δ_0 will be referred to as the 'elevation anisotropy' and Σ_0 as the 'backscatter anisotropy'.

Since both anomalies in the elevation measurement can be related to the backscatter, there is clearly an incentive to understand the scattering from the surface of the ice sheets, how it changes over time, and how it affects the elevation measurement. Chapter 2 describes measurements of microwave scattering and propagation within the Antarctic snowpack using the ERS-1 radar altimeter. Chapter 3 relates these variations in scattering to the snow structure, and quantifies the errors in the elevation measurement which might be expected as the snowpack responds to changes in the meteorological conditions.

Even if the problems associated with microwave scattering can be overcome, and accurate measurements of elevation change obtained, these must still be converted into estimates of mass balance. This poses another problem for the geodetic method. The density of the ice sheets cannot necessarily be assumed constant because the rate at which snow becomes denser as it is buried depends upon climatic parameters such as temperature, accumulation rate and the strength of the winds, which compact the surface layer (Alley 1987; Wilkinson 1988). If these climatic parameters vary, the resulting density changes will cause the surface elevation to change independently of the mass balance. Chapter 3 describes a numerical model of snow compaction, which was used to estimate the resulting errors in the geodetic determination of mass balance.

The changes in scattering and densification are both driven by changes in the meteorological boundary conditions at the ice-sheet surface. Chapter 4 presents some overall conclusions concerning the impact of the natural variability of the weather, and more persistent changes in climate, upon the geodetic determination of ice sheet mass balance using satellite radar altimetry.

2. Measurements of microwave scattering in Antarctica

2.1 Introduction to scattering.

It was noted in Chapter 1 that the largest source of error in the geodetic measurement is associated with changes in the microwave scattering properties of the snow. Figure 2.1 shows three possible mechanisms for generating backscatter from the ice sheets. Since the discovery by Ridley and Partington (1988) that a significant proportion of the altimeter return originates from beneath the air-snow interface, there has been some debate as to which of these mechanisms is most important (Ridley and Partington 1988; Remy and Minster 1991; Remy et al. 1995).

To date the Seasat satellite launched in 1978 has provided most of the observational data pertinent to the investigation of microwave scattering in Antarctica. This has limited the generality of conclusions which may be drawn, because Seasat only observed the margins of the ice sheet, where snow conditions are strongly influenced by gravity driven katabatic winds. In this chapter the ERS-1 altimeter is used to obtain comprehensive measurements of microwave scattering and propagation for all snow conditions found across the plateau of Antarctica. These data provide the basis for an investigation (described in chapter 3) into the relative importance of the three mechanisms shown in figure 2.1, and the contribution of each to the elevation errors of figure 1.1a and 1.1b.

After some processing, the shape of the ERS-1 radar echo reveals the distribution of backscatter as a function of depth into the snow. This allows the component of the backscatter σ°_{surf}, which arises from the reflection at the air-snow interface, to be

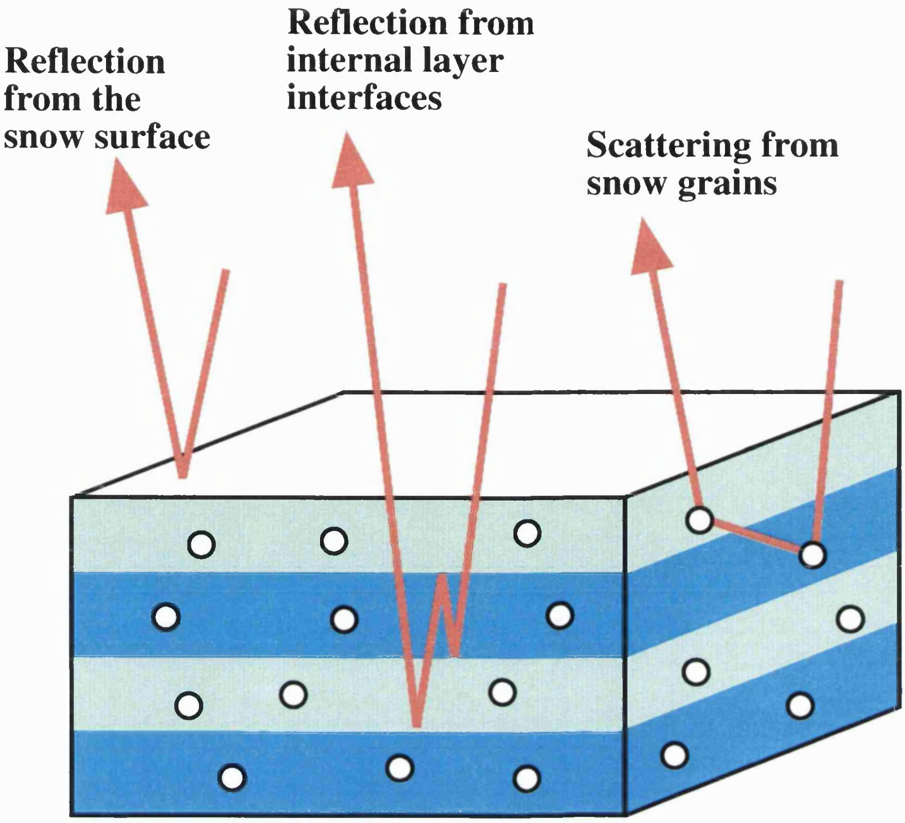

Figure 2.1 The mechanisms responsible for the altimeter echo. The microwaves may return to the altimeter through reflection at the air-snow interface, reflections at internal layer interfaces, and scattering by densely packed snow grains. Multiple reflections, multiple scattering and combinations of reflection and scattering may also occur. In this thesis, the term 'volume backscatter' is used to describe all contributions from beneath the air-snow interface.

measured separately from the component σ^{o}_{vol}, from reflections and volume scattering deeper within the snowpack. The extinction coefficient k_e, which determines the rate at which the signal is attenuated in propagating through the snow, can also be measured from the distribution of scattering with depth.

The theory behind the measurement is described in sections 2.1 and 2.2. Section 2.3 briefly describes the ERS-1 radar and its operation. Section 2.4 presents the numerical algorithms applied to the ERS-1 data to retrieve σ^{o}_{surf}, σ^{o}_{vol} and k_e, while the accuracy of this retrieval is discussed in section 2.5. Finally, in section 2.6, values of σ^{o}_{surf}, σ^{o}_{vol} and k_e, recovered from over 1000 locations across the Antarctic plateau, are presented. The observations are summarised in section 2.7.

2.2 The altimeter echo and the distribution of scattering versus depth

General expression for the altimeter echo

This section gives an overview of the relationship between the altimeter echo, the topography of the surface, and the distribution of backscatter as a function of depth. The intention is to provide a theoretical basis for the retrieval of σ^{o}_{surf}, σ^{o}_{vol} and k_e from altimeter echoes. The derivation is based upon one by Wingham (1995) and is presented here to define the notation used in later sections and make clear the approximations used.

Figure 2.2 shows the coordinate system used throughout this section. All elevations are referenced to a spherical datum of radius R (about one Earth radius), centred about a point O lying near the Earth's centre. The satellite location is described by a point M on the sphere and a height $h(M)$ radially above it.

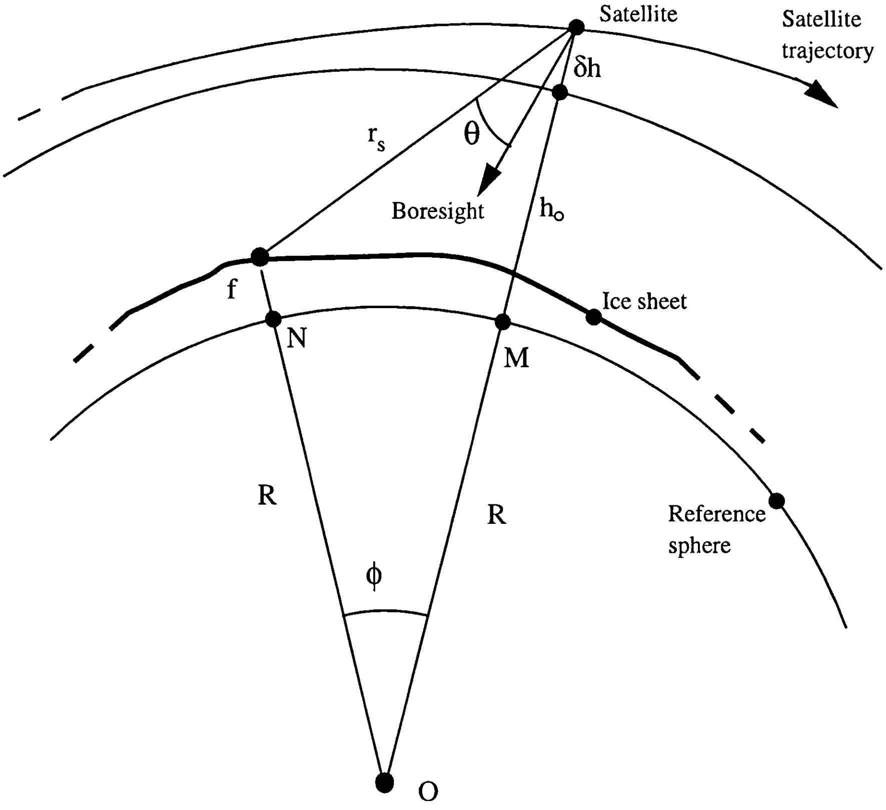

Figure 2.2 The co-ordinates used in the derivation of the altimeter echo. All elevations $f(N)$ and the satellite altitude $h_o + \delta h(M)$ are referenced to a sphere of radius R centred at O (which is close to, but not necessarily coincident with, the centre of the Earth). Note that the boresight direction need not lie in the plane NOM.

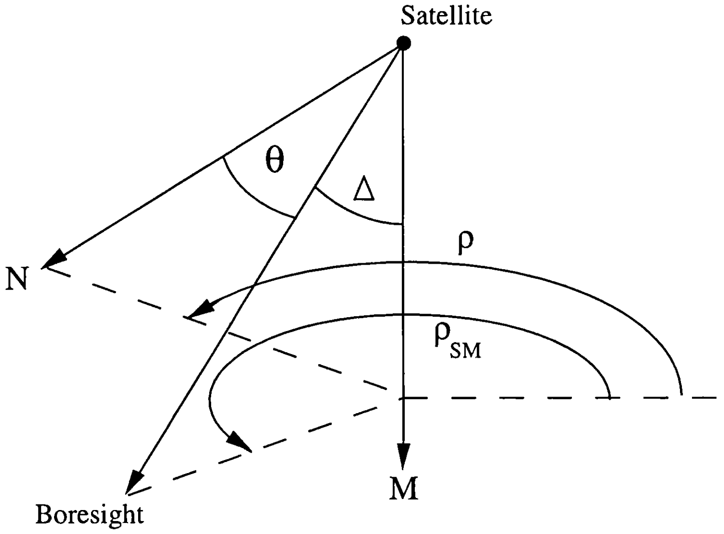

Figure 2.3 The boresight direction, defined by Δ *and* ρ_{SM}*, is assumed constant over regions about 100 km across.* Δ *and* ρ_{SM} *were calculated by assuming that the boresight direction is normal to the WGS84 ellipsoid.*

In later approximations, it is useful to write

$$h(M) = h_0 + \delta h(M) \qquad (2.2.1)$$

where $\delta h(M)$ describes small departures about the nominal operating height h_0. The surface is located at height $f(N)$ radially above points N on the sphere.

The altimeter echo can be derived by applying the radar equation (Skolnik 1970). This states that the power received from an area element of the surface dA is given by

$$dp_{surf}(t) = E_t q\left(t - \frac{2r_s}{c}\right)\frac{\lambda^2 g^2(\sin\theta)\sigma^{o}_{surf}\,dA}{(4\pi)^3 L_s r_s^4} \qquad (2.2.2)$$

where $E_t q(t)$ is the transmitted power envelope and E_t is the total energy transmitted; c is the speed of light; λ is the wavelength of the transmitted radiation; $g(\sin\theta)$ is the gain of the antenna in the direction of the surface element (an angle θ from the antenna boresight direction); σ^{o}_{surf} is the backscatter coefficient of the surface; L_s represents the power loss incurred in propagation through the atmosphere; and r_s is the range from the satellite to the area element.

Because some of the radiation is scattered from beneath the surface, the contribution from a volume element dV, a depth z beneath dA, must also be considered. Under the assumption that incidence angles are small enough that the additional range is well approximated by z (see Wingham (1995) for a more complete justification), this contribution is given by

$$dp_{vol}(t) \approx E_t q\left(t - \frac{2r_s}{c} - \frac{2z}{c_{ice}}\right)\frac{\lambda^2 g^2(\sin\theta)\sigma_v\,dV}{(4\pi)^3 L_v (r_s + z)^4} \qquad (2.2.3)$$

where σ_v is the radar cross section per unit volume of snow; c_{ice} is the speed of propagation within the snow, and L_v represents the propagation losses.

In general L_v will be larger than L_s since it includes the extinction of the signal as it propagates through the snow and passes through the air-snow interface. This attenuation is described by an extinction coefficient k_e, assumed constant within the range of depths sampled by the altimeter, and a transmission coefficient k_t so that

$$\frac{1}{L_v} = \frac{1}{L_s} k_t^2 e^{-2k_e z} \qquad (2.2.4)$$

The radar echo $p(M,t)$ is obtained by integrating equation (2.2.2) over the surface of the ice sheet and integrating equation (2.2.3) over its volume. First, however, some simplifying assumptions can be made.

Applying the cosine rule to the triangle formed by dA, O and the satellite, and then neglecting small terms, the range r_s can be approximated by

$$r_s \approx h_0 + \delta h(M) - f(N) + \frac{2R^2 \eta \sin^2 \frac{\phi}{2}}{h_0} \qquad (2.2.5)$$

where ϕ is the angle subtended by N and M at O and the dimensionless constant η is given by

$$\eta = \left(1 + \frac{h_o}{R}\right) \qquad (2.2.6)$$

The following approximations can be used to further simplify equations (2.2.2 and 2.2.3).

$$\frac{1}{r_s^4} \approx \frac{1}{(r_s + z)^4} \approx \frac{1}{h_0^4} \tag{2.2.7}$$

Also, spherical trigonometry can be used to show that

$$\sin\theta \approx \frac{2R}{h_0}\left[\sin^2\frac{\phi}{2} + \frac{h_0^2}{R^2\eta^2}\sin^2\frac{\Delta}{2} + \frac{h_0 \sin\Delta}{2R\eta}\sin\phi\cos(\rho - \rho_{SM})\right]^{\frac{1}{2}} \tag{2.2.8}$$

where the coordinates $[R, \rho, \phi]$ locate N in a spherical coordinate system, centred at O, and with axis of rotation along OM; ρ_{SM} is the azimuthal angle of the boresight direction in the same coordinate system, and Δ is the angle between the boresight and the axis OM (see figure 2.3). The angles Δ and ρ_{SM} can be calculated by assuming that the boresight direction is normal to the ellipsoid.

Finally, it can be assumed that the surface slopes of the ice sheet are small enough that

$$dA \approx dS_N \tag{2.2.9}$$

where dS_N is the spherical projection of dA onto the sphere, and that the depth of penetration is small enough that, for the range of depths contributing to the echo,

$$dV \approx dz\, dS_N \tag{2.2.10}$$

The approximations (2.2.5 to 2.2.10) are accurate enough that, provided δh and f are smaller than about 100 m, the relative errors introduced into $p(M,t)$ will be of order 10^{-2} (see Wingham (1995) for details of the derivation and accuracy of each approximation). Applying these approximations and integrating, using the substitution $\tau \equiv 2z/c_{ice}$, gives the following expression for the echo.

$$p(M,t) \approx \frac{E_t \lambda^2}{(4\pi)^3 h_0^4 L_s} \int_{-\infty}^{\infty} d\tau\, s(t-\tau) \iint_{N \in Sphere} dS_N \quad .$$

$$g^2\left(\frac{2R}{h_0}\left[sin^2\frac{\phi}{2} + \frac{h_0^2}{R^2\eta} sin^2\frac{\Delta}{2} + \frac{h_0\, sin\,\Delta}{2R\eta} sin\,\phi\, cos(\rho - \rho_{\mathrm{SM}}) \right]^{\frac{1}{2}} \right) \quad \cdot \qquad (2.2.11)$$

$$q\left(\tau - \frac{4R^2\eta}{ch_0} sin^2\frac{\phi}{2} + \frac{2f(N)}{c} - \frac{2h_0}{c} - \frac{2\delta h(M)}{c} \right)$$

The function s is given by

$$s(t) = \begin{cases} \sigma^{\mathrm{o}}_{\mathrm{surf}}\delta(t) + \sigma^{\mathrm{o}}_{\mathrm{vol}} c_{ice} k_e\, exp\left[-c_{ice} k_e t\right], & t \geq 0 \\ 0, \quad t < 0 \end{cases} \qquad (2.2.12)$$

where δ is the Dirac delta function and the integrated volume backscatter $\sigma^{\mathrm{o}}_{\mathrm{vol}}$ is defined as follows to ensure that $\sigma^{\mathrm{o}}_{\mathrm{surf}} + \sigma^{\mathrm{o}}_{\mathrm{vol}} = \sigma^{\mathrm{o}}$, the total backscatter.

$$\sigma^{\mathrm{o}}_{\mathrm{vol}} = \frac{\sigma_v k_t^2}{2k_e} \qquad (2.2.13)$$

Physically, s may be regarded as the distribution of backscatter with depth (expressed in terms of the propagation delay in the snow); the first term describes the reflection from the air snow interface, the second the exponentially decaying contribution from the volume. There is no scattering from above the surface so s is zero for negative propagation delays.

Separating short scale and long scale topography

It is useful to separate the topography f into a short scale component f_{short}, which varies on a length scale much smaller than the altimeter footprint, and a remaining long scale component f_{long} so that

$$f = f_{short} + f_{long} \tag{2.2.14}$$

The effect of the short scale topography upon the echo shape can be found by considering the quantity $u = -2f_{short}/c$ to be a random variable with probability density function D_{short}. Because f_{short} varies on scales much shorter than the altimeter footprint, its effects are well averaged, even in a single echo. Substituting equation (2.2.14) into equation (2.2.11) and taking the expected value gives

$$\begin{aligned} p(M,t) \approx \frac{E_t \lambda^2}{(4\pi)^3 h_0^4 L_s} \int_{-\infty}^{\infty} d\tau\, s(t-\tau) \int_{-\infty}^{\infty} du\, D_{short}(u) \iint_{N \in Sphere} dS_N \quad . \\ g^2 \left(\frac{2R}{h_0} \left[sin^2 \frac{\phi}{2} + \frac{h_0^2}{R^2 \eta} sin^2 \frac{\Delta}{2} + \frac{h_0 \, sin\,\Delta}{2R\eta} sin\,\phi\, cos(\rho - \rho_{SM}) \right]^{\frac{1}{2}} \right) \quad \cdot \\ q \left(\tau - u - \frac{4R^2\eta}{ch_0} sin^2 \frac{\phi}{2} + \frac{2 f_{long}(N)}{c} - \frac{2h_0}{c} - \frac{2\delta h(M)}{c} \right) \end{aligned} \tag{2.2.15}$$

The longer scale topography f_{long} varies too slowly across the footprint for its effect upon the echo shape to be modelled as a well averaged random process. Most previous investigations have assumed that this topography varies on scales much larger than the altimeter footprint. Then, for all points N where the antenna gain g is non-negligible,

$$f_{long}(N) \approx f_{long}(M) \tag{2.2.16}$$

This allows the altimeter echo to be written as a convolution of four terms as follows

$$p(M,t+t_0(M)) \approx \int_{-\infty}^{\infty} d\tau\, s(t-\tau) \int_{-\infty}^{\infty} du\, D_{short}(u) \int_{-\infty}^{\infty} dv q(v) I(\tau - \nu - u) \tag{2.2.17}$$

where

$$I(t) = \frac{E_t \lambda^2}{(4\pi)^3 h_0^4 L_s} \iint_{N \in Sphere} dS_N\, \delta\left(t - \frac{4R^2\eta}{ch_0} sin^2 \frac{\phi}{2}\right). \\ g^2\left(\frac{2R}{h_0}\left[sin^2\frac{\phi}{2} + \frac{h_0^2}{R^2\eta^2} sin^2\frac{\Delta}{2} + \frac{h_0\, sin\,\Delta}{2R\eta} sin\,\phi\, cos(\rho - \rho_{SM})\right]^{\frac{1}{2}}\right) \tag{2.2.18}$$

is the impulse response of the reference sphere - c.f. the impulse response of a flat surface calculated by Brown (1977). In equation (2.2.17) the origin of time delay is redefined to correspond to the time of arrival $t_0(M)$ from the point on the surface f_{long} which is closest to the satellite. If the approximation (2.2.16) is satisfied then

$$t_0(M) \approx \frac{2h_0}{c} + \frac{2\delta h(M)}{c} - \frac{2f_{long}(M)}{c} \tag{2.2.19}$$

and equation (2.2.17) follows from equation (2.2.15).

If the approximation (2.2.16) is not satisfied, the echo shape will be distorted from the simplified model defined by equation (2.2.17). The approximation was introduced by Brown (1977) to describe altimeter echoes recorded over the oceans, and there is every reason to expect it to fail over the undulating topography of the ice sheets. This fact has not generally been acknowledged so it is worth investigating the nature of the distortion. If approximation (2.2.16) does not hold then

$$p(M,t+t_0(M)) \approx \int_{-\infty}^{\infty} d\tau\, s(t-\tau) \int_{-\infty}^{\infty} du\, D_{short}(u) \int_{-\infty}^{\infty} dv q(v) I_M(M, \tau - \nu - u) \tag{2.2.20}$$

where

$$I_M(M,t)=\frac{E_t\lambda^2}{(4\pi)^3 h_0^4 L_s}\iint_{N\in Sphere} dS_N\delta\left(t-\frac{4R^2\eta}{ch_0}sin^2\frac{\phi}{2}+\frac{2f_{long}(N)}{c}-\frac{2h_0}{c}-\frac{2\delta h(M)}{c}+t_0(M)\right).$$
$$g^2\left(\frac{2R}{h_0}\left[sin^2\frac{\phi}{2}+\frac{h_0^2}{R^2\eta^2}sin^2\frac{\Delta}{2}+\frac{h_0\,sin\,\Delta}{2R\eta}sin\,\phi\,cos(\rho-\rho_{\mathrm{SM}})\right]^{\frac{1}{2}}\right)$$

(2.2.21)

The nature of the distortion becomes clearer by writing equation (2.2.20) in the form

$$p(M,t+t_0(M))\approx\int_{-\infty}^{\infty}d\tau\, s(t-\tau)\int_{-\infty}^{\infty}du\, D_{short}(u)\int_{-\infty}^{\infty}dv q(v)\int_{-\infty}^{\infty}dw\, D_{long}(M,w)I(\tau-v-u-w)$$

(2.2.22)

where

$$D_{long}(M,t)=\int_{-\infty}^{t}d\tau\; K_r(t-\tau)I_M(M,\tau)$$

(2.2.23)

and the resolvent kernel K_r satisfies $K_r(t)=0$, for all $t<0$, and

$$\delta(t)=\int_{-\infty}^{t}d\tau K_r(t-\tau)I(\tau)$$

(2.2.24)

otherwise. Equation (2.2.22) is identical to equation (2.2.17), except for the convolution with the function $D_{long}(M,t)$, which accounts for the distortion of the echo by the long scale topography. Because $t_0(M)$ is defined to be the time of arrival from the closest point on the surface f_{long}, it follows, using approximation (2.2.15), that

$$\frac{4R^2\eta}{ch_0}sin^2\frac{\phi}{2}+\frac{2f_{long}(N)}{c}-\frac{2h_0}{c}-\frac{2\delta h(M)}{c}+t_0(M)\;>\;0$$

(2.2.25)

from which it can be shown that $D_{long}(M,t) = 0$ for all $t < 0$. This implies that, when the time origin is taken as the first arrival time from f_{long} - as it has been conventionally by the use of a retracking algorithm (Ridley et al. 1988; Partington et al. 1989; Davis and Moore 1993) - the long scale topography always causes the redistribution of power towards later times in the echo. Microwave penetration into the snow also skews the distribution of arrival time in favour of later arrivals, so there is obviously scope for confusing the effects of penetration with the distortion of the echo introduced by the long scale topography.

To see how serious the confusion between penetration and topography may become, it would be useful to calculate the distortion kernel D_{long}. However, because $I_M(M,t)$ and $t_0(M)$ depend upon f_{long} in a complicated fashion, it is difficult to evaluate D_{long} analytically for a general case. At one extreme, when f_{long} is constant, the approximation (2.2.16) holds everywhere with equality; then $D(M,t) = \delta(t)$ and equations (2.2.17) and (2.2.22) become identical. It is reasonable then to suppose that there will be little effect upon the echo shape when the long scale topography has small amplitude, long wavelength or both. Section 2.5 describes some numerical simulations which provide quantitative bounds on the wavelengths and amplitudes for which the assumption (2.2.16) is justified - first though, the theory and methodology behind the estimation of $\sigma^{o}_{\mathrm{surf}}$, $\sigma^{o}_{\mathrm{vol}}$ and k_e is presented, so that the errors in the retrieval of these parameters can be discussed in the light of the simulations.

Averaging the echoes

It is impractical to estimate $\sigma^{o}_{\mathrm{surf}}$, $\sigma^{o}_{\mathrm{vol}}$ and k_e from a single echo. This is because of noise on the echoes, and because individual echoes are generally more distorted by topography than their spatial average. The spatially averaged echo $\bar{p}$ can be defined as follows

$$\overline{p}(t) = \iint\limits_{M \in Sphere} dS_M \, W(M) \, p(M, t + t_0(M)) \tag{2.2.36}$$

where W is a spatially varying weighting function, which confines the averaging to the region of interest. The altimeter boresight direction, defined by ρ_{SM} and Δ, will vary slightly between echoes, but for pointing inaccuracies typical of ERS-1, these parameters may be assumed constant over survey regions of order 100 km in diameter (Wingham 1995). With this approximation, substituting equation (2.2.22) into equation (2.2.36) provides

$$\overline{p}(t) = \int_{-\infty}^{t} d\tau \, I(t-\tau) \overline{r}(\tau) \tag{2.2.37}$$

where

$$\overline{r}(t) = \int_{-\infty}^{t} d\tau \, s(t-\tau) \int_{-\infty}^{\infty} du \, D_{short}(u) \int_{-\infty}^{\infty} dv q(v) \overline{D}_{long}(\tau - v - u) \tag{2.2.38}$$

and

$$\overline{D}_{long}(t) = \iint\limits_{M \in Sphere} dS_M \, W(M) \, D_{long}(M, t) \tag{2.2.39}$$

Equation (2.2.37) is a linear Volterra integral equation of the first kind, which may be solved to obtain $\overline{r}$ using

$$\overline{r}(t) = \int_{-\infty}^{t} d\tau \, K_r(t-\tau) \overline{p}(\tau) \tag{2.2.40}$$

where K_r is the resolvent kernel defined by equation (2.2.24). The reason that $\bar{r}$ (which is hereafter referred to as the deconvolution) is a useful quantity can be seen more clearly by defining

$$J(\tau) = \int_{-\infty}^{\infty} du\, D_{short}(u) \int_{-\infty}^{\infty} dv q(v) \overline{D}_{long}(\tau - v - u) \tag{2.2.41}$$

so that equation (2.2.38) becomes

$$\bar{r}(t) = \int_{-\infty}^{t} d\tau\, s(t-\tau) J(\tau) \tag{2.2.42}$$

From equation (2.2.42) it is clear that $\bar{r}$ can be regarded as a measurement of s, with resolution determined by the width of the function J. The width of J depends upon the widths of q, D_{short} and $\overline{D}_{long}$ through the convolution (2.2.41). For typical altimeters the width of q is less than 0.5 m (in terms of range); the width of D_{short} is determined by the amplitude of small scale roughness which rarely exceeds 0.5 m; while the numerical simulations described in section 2.5 reveal that, for the flatter regions of the ice sheet, $\overline{D}_{long}$ is also narrower than 0.5 m. In the flatter regions then, the function $\bar{r}$ will reveal the scattering behaviour with a depth resolution somewhat better than 1 m.

Resolution of 1m in depth is an order of magnitude finer than the penetration depth (the scale upon which s decays), so simply inspecting $\bar{r}$ will reveal the behaviour of s. In particular, the contributions from the reflection at the air-snow interface and from the volume beneath may be distinguished from each other. Under the additional assumption that J is approximately Gaussian, which is investigated further in section 2.5, this resolution proves sufficient to obtain useful estimates of σ^0_{surf}, σ^0_{vol} and k_e. Section 2.4 describes the retrieval of these parameters from ERS-1 radar altimeter data. Several features of this procedure are specific to the design and operation of the ERS-1 altimeter, so this is described first in the following section.

2.3 The ERS-1 satellite radar altimeter

The ERS-1 altimeter is a nadir pointing, Ku band, frequency modulated radar. The antenna transmits linearly polarised microwaves within a narrow beam with 3dB-full-beamwidth 1.3°. For the nominal operating altitude of 800 km, this gives the instrument a circular footprint some 20 km in diameter. The power backscattered from this footprint is measured as a function of time delay, using the same antenna for reception as transmission. For typical surface geometries, the illuminated area on the ground is limited by the pulse duration, not the antenna gain pattern: the altimeter is described as pulse limited.

The ERS-1 altimeter has two modes with different range resolutions. In both modes, pulse compression is used to increase the range resolution for a given signal to noise ratio (Ulaby et al. 1986). The transmitted pulse is a frequency modulated 'chirp', of duration $20\mu s$ and central frequency 13.8 GHz. For the high resolution 'ocean' mode, the chirp bandwidth is 330 MHz, giving an effective pulse duration of 3.02 ns, and range resolution of about 0.5 m. The lower resolution 'ice' mode has bandwidth 82.5 MHz, effective pulse duration 12.12 ns, and range resolution of about 2 m.

The echo is obtained from the power spectrum of an analogue signal obtained by 'dechirping' the return from the surface (Ulaby et al. 1986). First, the analogue signal is passed through a 3.2 MHz bandwidth filter to prevent aliasing during sampling - it will be seen later that the characteristics of this 'IF filter' affect the echo shape. Next, the signal is attenuated by an automatic gain control (AGC) mechanism to prevent saturation of the analogue to digital converters which sample the signal. Finally, the digital signal is processed by a fast Fourier transform (FFT) algorithm and the square modulus taken to give 64 samples of echo power spaced at 50 kHz intervals. This spacing can be converted into time delay using the rate of frequency modulation during chirp transmission: the sample spacing is 3.02 ns for ocean mode and 12.16 ns for ice mode.

The echoes are recorded at a rate of 1020 Hz and successive blocks of 50 are averaged on-board before being telemetered to Earth. The telemetered echo samples are referred to as waveform data; an example is shown in figure 2.4. Because of the finite cut-off of the IF filter response, some of the echo power is aliased and appears in the first few samples of the echo. The time delay interval spanned by the 64 samples is known as the range window and is about 200 ns (30 m) wide in ocean mode and about 800 ns (120 m) in ice mode.

An on-board processor implements a tracking algorithm which ensures that the range window brackets the first return from the surface. The time delay corresponding to the centre of the range window is telemetered along with the waveform data, and the AGC attenuation; together, this information allows the echo power to be reconstructed as a function of time delay.

In general, the surfaces reflecting power back to the satellite are rough enough that the phase of returns from different scatterers within the footprint is random and uniformly distributed between 0 and 2π. Under these circumstances the received power is an exponentially distributed random variable (Ulaby et al. 1986). Even after fifty echoes are averaged together on board, the waveform data are still subject to high noise levels (see figure 2.4 again). This noise is called speckle noise, and in normal operation it dominates thermal noise from the receiver electronics.

Several corrections must be applied to the telemetered range to account for propagation delays within the atmosphere. An 'ionospheric' correction is applied to

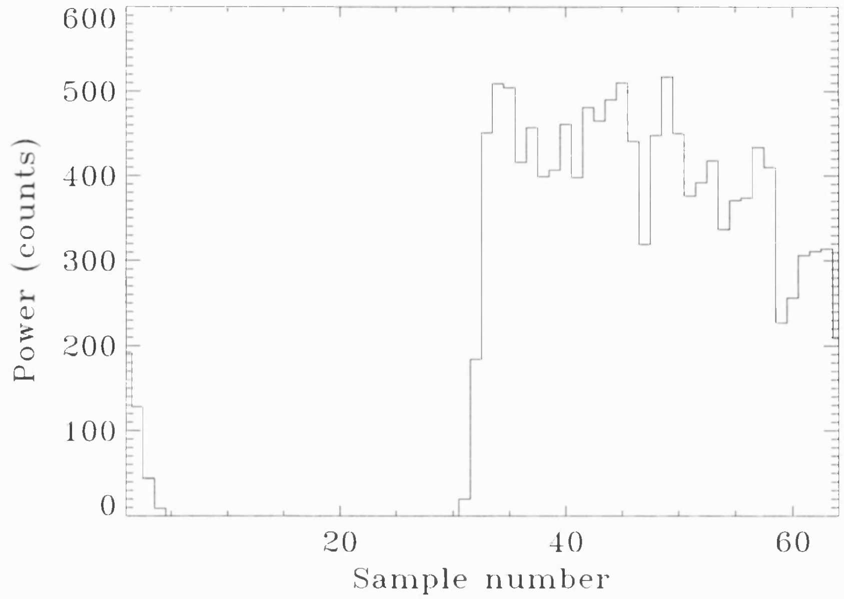

Figure 2.4 An example of the waveform samples telemetered by ERS-1. The steep leading edge locates the first return from the surface. Later samples show power from successively greater time delay, and hence range. Note that, because the surface is rough, returns are received from off nadir directions (large ranges) and superpose with random phase to give considerable noise levels, even after on-board averaging. The aliased samples are visible on the far left.

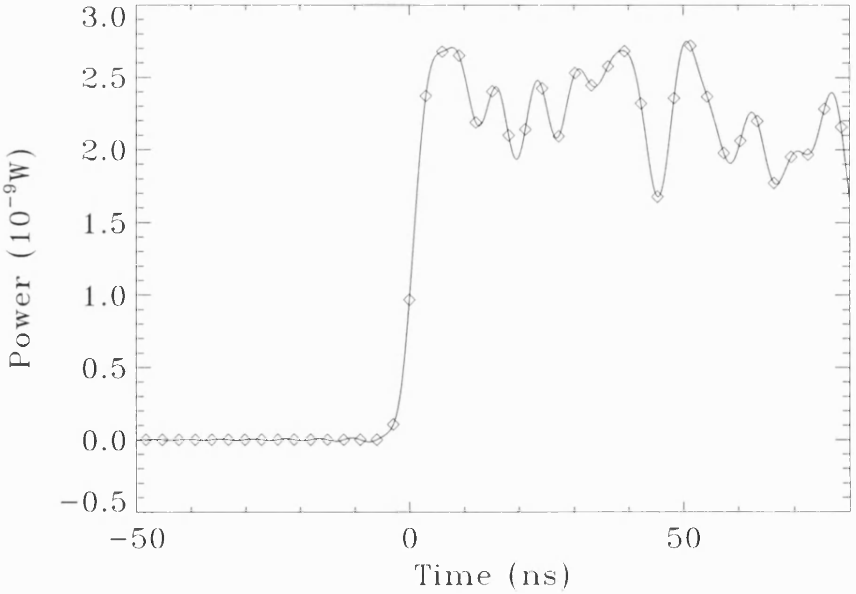

Figure 2.5 The continuous echo power reconstructed from the discrete waveform data, shown in figure 2.4, and the AGC value. The time delay is referenced to the leading edge position using the OCOG threshold retracking algorithm.

correct for the effects of free electrons in the ionosphere. The free electron content is predicted for the satellite location, taking into account the time of day, season and sunspot activity. The resulting correction to range is typically 2 - 20 cm (Cudlip et al. 1994).

Two further corrections, the 'wet tropospheric' and 'dry tropospheric' corrections, are applied to account for propagation delays at lower altitudes. The 'wet tropospheric' correction is proportional to the vertically integrated water vapour content of the atmosphere, which is predicted by weather forecasting models. Over ice sheets the magnitude of the wet tropospheric correction is typically less than 10 cm. The propagation delay caused by the dry air is corrected by the 'dry tropospheric' correction which depends upon the surface pressure (from weather forecasting models) and the latitude. At about 2.5 m the dry tropospheric correction is larger than the wet tropospheric correction but is generally known to within 1 cm (Cudlip et al. 1994). There is also a correction for the propagation delay and the attenuation of the signal caused by rain. However, for the regions of Antarctica considered here, it never rains, so the 'liquid water' range correction was omitted and an atmospheric attenuation L_s of 0 dB was assumed (i.e. $L_s=1$).

To obtain the satellite position, the satellite is sporadically tracked by a network of satellite-laser-ranging stations. In conjunction with this tracking, numerical models which incorporate the forces on the satellite due to gravity, atmospheric drag and solar radiation are used to compute the orbit throughout the mission. The orbit solutions provide the latitude and longitude of the sub-satellite point and the satellite altitude above a reference ellipsoid (WGS84) which approximates the figure of the Earth. The orbit solutions also allow the measured range to be corrected for the Doppler shift, caused by the vertical component of the satellite velocity. Because the frequency modulation during chirp transmission is linear, this Doppler shift would otherwise cause a proportional error in the range measurement.

There has been a vast improvement in the accuracy of ERS-1 orbit solutions over the last five years or so, to the degree that orbit errors are now much smaller than the elevation errors shown in figures 1.1 and 1.2. The accuracy of the satellite orbit is therefore no longer the limiting error in the application of the geodetic method, as it has been for previous measurements using Seasat and Geosat.

2.4 Recovering snow scattering parameters from ERS-1 altimeter data

Reconstructing the radar echo from the telemetry

At a set of locations M_k $(k = 1, 2, \ldots, N_k)$, the altimeter records N_l waveform samples WF_{kl} $(l = 1, 2, \ldots, N_l)$. The attenuation AGC_k (in dB), and the time delay TD_k to the centre of the range window are also telemetered. A combined correction to time delay COR_k accounts for all propagation delays in the atmosphere and the Doppler error. The time delays corresponding to individual waveform samples t_{kl} are then given by

$$t_{kl} = TD_k + COR_k + \Delta_t (l - l_c) \tag{2.4.1}$$

where Δ_t is the spacing between samples and I_c is the sample corresponding to the centre of the range window.

Within the range window, the continuous echoes $p(M_k, t)$ are well approximated by a bandwidth-limited function $\hat{p}(M_k, t)$ defined by

$$\hat{p}(M_k, t) = C_g \left[\sum_{l=N_a+1}^{N_l} \mathrm{WF}_{kl} \frac{\sin \omega_N (t - t_{kl})}{\omega_N (t - t_{kl})} + \sum_{l=1}^{N_a} \mathrm{WF}_{kl} \frac{\sin \omega_N (t - t_{kl} - N_l \Delta_t)}{\omega_N (t - t_{kl} - N_l \Delta_t)} \right] \tag{2.4.2}$$

where $\omega_N = \pi/\Delta_t$ is the Nyquist frequency of the sampling (Papoulis 1991). The aliased waveform samples $(1,2,..N_a)$ are shifted by $N_l\Delta_t$ to the end of the echo rather than the start: this reduces errors arising from the sudden truncation of the waveform data. The normalisation constant C_g is given by

$$C_g = C_0.10^{\left(\frac{1}{10}\mathrm{AGC}_k\right)} \tag{2.4.3}$$

where C_0 depends upon the gain of the receiver, and upon the conversion factor between counts (the units of WF_{kl}) and Watts. For the ERS-1 ocean mode data used in this thesis, $C_0 = 1.54 \times 10^{-15}$ Watts per count. Figure 2.5 shows the echo reconstructed from the waveform data shown in figure 2.4.

Averaging the echoes

The integration over location in equation (2.2.36) can be approximated by a sum to give the following approximation to $\bar{p}$

$$\tilde{p}(t) = \sum_{k=1}^{N_k} \tilde{W}(M_k)\hat{p}\big(M_k, t + t_0(M_k)\big) \tag{2.4.4}$$

where

$$\tilde{W}(M_k) = \frac{W(M_k)}{\sum_{k=1}^{N_k} W(M_k)} \tag{2.4.5}$$

Following Wingham (1995), the form adopted for the weighting function W was

$$W(M) = C\exp\left(\frac{1-\cos\phi_{SM}}{\tan^2\frac{\phi_w}{2}}\right) \tag{2.4.6}$$

This weighting function restricts the region over which the echoes are averaged to an area centred on a point S and subtending an angle of ϕ_w at O. ϕ_{SM} is the angle subtended at O by the satellite location M and the centre of the weighted region S. A value of 8×10^{-3} was used for ϕ_w giving a weighted region about 100 km across. The constant C is chosen such that the integral of W over the sphere is unity

In equation (2.4.4), the time origin $t_0(M_k)$ corresponds to the time of arrival of a return from the closest point on the surface f_{long}. This was estimated using the Offset Centre of Gravity (OCOG) threshold retracking algorithm (Bamber 1994). The time origin was set at the first waveform sample exceeding the 10% retracking threshold, i.e.

$$t_0(M_k) = \min\{t_{kl}\} \text{ such that } WF_{kl} > 0.1\left[\frac{\sum_{i=N_a}^{N_l} WF_{ki}^4}{\sum_{i=N_a}^{N_l} WF_{ki}^2}\right]^{\frac{1}{2}} \tag{2.4.7}$$

Figure 2.6 shows an average echo recorded in Antarctica (75 S, 15 E). Compared to the individual echo shown in figure 2.5, which was recorded in the same region, the fluctuations on the average echo are substantially reduced.

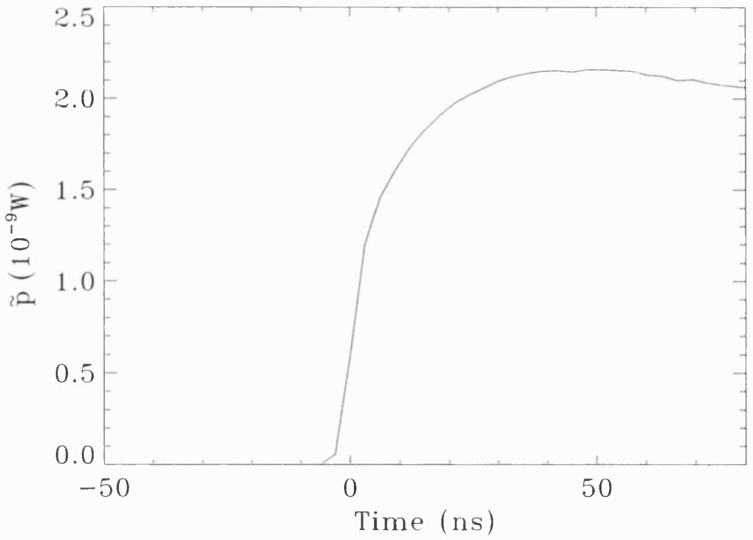

Figure 2.6 An average echo recorded from Dronning Maud Land (75 S, 15 E). Compared to the individual echo shown in figure 2.5, which was recorded in the same region, the fluctuations on the average echo are substantially reduced. The characteristic rounded shape is typical of echoes from ice sheets, where scattering from beneath the surface occurs.

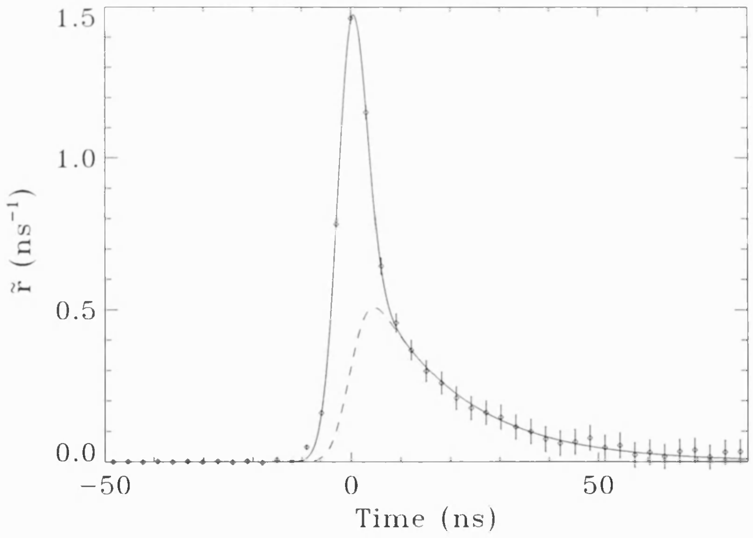

Figure 2.7 The deconvolution obtained from the average echo shown in figure 2.6. The deconvolution shows the separate contributions from the reflection at the air-snow interface (pronounced peak), and the subsurface scattering and reflections (exponentially decaying tail). The largest time delay shown (80 ns) equates to about 10 m depth. The model defined by equation (2.4.24) and the volume component of this model (the second term in the equation) are shown separately using solid and dashed line respectively. The error bars were calculated according to section 2.5.

It is noted, in passing, that the method for determining the average elevation of a region, presented in Wingham (1995), does not define the origin $t_0(M)$ as the first return from f_{long}, but as the first return from the sphere. To use this method equation (2.4.7) is simply replaced with $t_0(M_k) = 2(h_0 + \delta h(M_k))/c$, which can be determined from the ellipsoidal satellite coordinates and the geometry of the chosen reference sphere. With this choice of origin, it can be shown using equations (2.2.39), (2.2.21) and (2.2.23) that the distortion $\overline{D}_{long}$ is simply the distribution of the quantity $-2f_{long}/c$ across the weighted region. This is desirable for determining the average elevation (Wingham 1995), but, because the amplitude of f_{long} is typically ten metres or more, this choice of origin gives very poor resolution of the scattering function s, so is not suitable for the investigation into scattering described here.

Solving the integral equation

The integral equation (2.2.37) was solved numerically by the method of moments, using orthogonal sinc functions to span the solution space. (Subsequently an analytical solution was developed, and this is described in Appendix A). The numerical method seeks a bandwidth limited function $\tilde{r}$ which closely approximates the deconvolution $\bar{r}$. Because $\tilde{r}$ is bandwidth limited, it may be expressed in terms of discrete samples $\tilde{r}(t_j)$ as follows (Papoulis 1991).

$$\tilde{r}(t) = \sum_{j=1}^{N_l} \tilde{r}(t_j) \frac{\sin \omega_n (t - t_j)}{\omega_n (t - t_j)} \tag{2.4.8}$$

where $t_l = (l - l_c)\Delta_t$. Substituting $\tilde{p}$ (from equation 2.4.4) and $\tilde{r}$ (from equation 2.4.8) for $\bar{p}$ and $\bar{r}$ in equation (2.2.37) gives the following discrete representation of the integral equation

$$\tilde{\mathbf{p}} = \mathbf{A}\tilde{\mathbf{r}} \tag{2.4.9}$$

where elements i and j of the vectors $\tilde{\mathbf{p}}$ and $\tilde{\mathbf{r}}$ are the samples $\tilde{p}(t_i)$ and $\tilde{r}(t_j)$ respectively, and the elements a_{ij} of the matrix $\mathbf{A}$ are given by

$$a_{ij} = \int_{-\infty}^{t_i} d\tau \, I(t_i - \tau) \frac{\sin \omega_N (\tau - t_j)}{\omega_N (\tau - t_j)} \tag{2.4.10}$$

The discrete equivalent to the inverse equation (2.4.40) is then

$$\tilde{\mathbf{r}} = \mathbf{A}^{-1} \tilde{\mathbf{p}} \tag{2.4.11}$$

where $\mathbf{A}^{-1}$ denotes the inverse of $\mathbf{A}$.

The matrix $\mathbf{A}$ was obtained by evaluating the integral (2.4.10) numerically for each a_{ij}. The function $I(t)$ was evaluated analytically for a Gaussian approximation to the antenna gain g measured by Torres (1990) (see appendix A, equations A.3 - A.7 for the result). The integrand is negligible for sufficiently negative τ, and this allows the infinite lower limit to be replaced with a finite limit. The integration was performed by Gaussian quadrature, with the order of the quadrature scheme increased until a relative accuracy of 10^{-7} was obtained for each of the a_{ij}.

Singular value decomposition (SVD) was used to obtain the inverse $\mathbf{A}^{-1}$ and to determine whether the system of equations (2.4.9) was well conditioned. The SVD was performed using Numerical Algorithms Group (NAG) software. For any matrix $\mathbf{A}$, this routine calculates matrices ψ, ϕ and λ such that

$$\mathbf{A} = \psi \lambda \phi^{\mathrm{T}} \tag{2.4.12}$$

The matrices ψ and ϕ are orthonormal and the matrix λ is diagonal. The superscript T denotes the transpose. The elements of $\mathbf{A}$ are thus

$$a_{ij} = \sum_{k=1}^{N_l} \psi_{ik} \lambda_k \phi_{kj} \tag{2.4.13}$$

Because ψ and ϕ are orthonormal, the elements a_{ji}^{inv} of $\mathbf{A}^{-1}$ can immediately be written

$$a_{ji}^{inv} = \sum_{k=1}^{N_l} \phi_{jk} \lambda_k^{-1} \psi_{ki} \tag{2.4.14}$$

If any of the λ_k are zero, the matrix $\mathbf{A}$ is singular. A measure of ill conditioning is given by the ratio of the largest to the smallest λ_k. For the inversions performed here, this ratio was typically about 200, indicating that $\mathbf{A}$ is not singular, nor so ill conditioned that $\tilde{\mathbf{r}}$ is corrupted by rounding errors in $\mathbf{A}$ from the numerical evaluation of equation (2.4.10).

In practice, it is useful to replace equation (2.4.14) with a regularised inverse matrix $\mathbf{A}_{reg}^{-1}$ with elements a_{ji}^{reg} given by

$$a_{ji}^{reg} = \sum_{k=1}^{N_l} \phi_{jk} \frac{\lambda_k}{\lambda_k^2 + d^2} \psi_{ki} \tag{2.4.15}$$

where d is much smaller than the largest λ_k. This filters out terms in the expansion where λ_k is much smaller than d, reducing the range resolution of the deconvolution. The practical benefits are twofold; the noise levels on the deconvolution are reduced, and the impact of the sidelobes of the sinc function is lessened. The regularised deconvolution $\tilde{\mathbf{r}}_{reg}$ is given by

$$\tilde{\mathbf{r}}_{reg} = \mathbf{A}_{reg}^{-1} \tilde{\mathbf{p}} \tag{2.4.16}$$

For the inversions described in this thesis, d was set to 1% of the largest λ_k, giving a resolution of about 6 ns in time delay (about 1m in range). The regularised deconvolution will be used throughout the remainder of this thesis, although the subscript *reg* will be dropped. The deconvolution obtained from the average echo of figure 2.6 is shown in figure 2.7. The narrow, peaked return, from the reflection at the air-snow interface, is clearly visible, as is the exponentially decaying contribution from reflections and scattering at greater depth. The determination of the error bars is described later. Figure 2.7 also shows a least squares model fit, used to extract the parameters $\sigma^{\mathrm{o}}_{\mathrm{surf}}$, $\sigma^{\mathrm{o}}_{\mathrm{vol}}$ and k_e. This procedure is described in the next section.

Obtaining the scattering parameters

Assuming Gaussian forms for q and D_{short} and negligible influence from the long scale topography

$$q(t) \approx \frac{1}{\gamma_q\sqrt{\pi}} exp\left[-\left(t-\bar{t}_q\right)^2 / \gamma_q^2\right] \tag{2.4.17}$$

$$D_{short}(t) \approx \frac{1}{\gamma_{short}\sqrt{\pi}} exp\left[-\left(t-\bar{t}_{short}\right)^2 / \gamma_{short}^2\right] \tag{2.4.18}$$

$$D_{long}(t) \approx \delta\left(t-\bar{t}_{long}\right) \tag{2.4.19}$$

Using these approximations, the convolution (2.2.41) can be evaluated analytically, giving the following Gaussian approximation for J

$$J(t) \approx \frac{1}{\gamma\sqrt{\pi}} exp\left[-\left(t-\bar{t}\right)^2 / \gamma^2\right] \tag{2.4.20}$$

where

$$\gamma = \sqrt{\gamma_q^2 + \gamma_{short}^2} \qquad (2.4.21)$$

$$\bar{t} = \bar{t}_q + \bar{t}_{short} + \bar{t}_{long} \qquad (2.4.22)$$

Using the approximation (2.4.20), the integral in equation (2.4.24) can be carried out analytically giving the following five parameter model for $\bar{r}$

$$\bar{r}(t) \approx y\left(t; \sigma^{o}_{surf}, \sigma^{o}_{vol}, k_e, \gamma, \bar{t}\right) \qquad (2.4.23)$$

where

$$\begin{aligned} y\left(t; \sigma^{o}_{surf}, \sigma^{o}_{vol}, k_e, \gamma, \bar{t}\right) \; &= \; \frac{\sigma^{o}_{surf}}{\gamma\sqrt{\pi}} e^{-\frac{(t-\bar{t})^2}{\gamma^2}} + \\ \frac{\sigma^{o}_{vol} c_{ice} k_e}{2} exp&\left(\frac{\gamma^2 c_{ice}^2 k_e^2}{4} - c_{ice} k_e (t - \bar{t})\right)\left[1 + erf\left(\frac{(t-\bar{t})}{\gamma} - \frac{\gamma c_{ice} k_e}{2}\right)\right] \end{aligned} \qquad (2.4.24)$$

The parameters $\sigma^{o}_{\mathrm{surf}}$, $\sigma^{o}_{\mathrm{vol}}$, k_e, γ and $\bar{t}$ were estimated by fitting the model y to the deconvolution $\tilde{r}$ using the Levenberg-Marquardt method (Press et al. 1986). This method seeks values of $\sigma^{o}_{\mathrm{surf}}$, $\sigma^{o}_{\mathrm{vol}}$, k_e, γ and $\bar{t}$ which minimise the value of χ^2 defined by

$$\chi^2 = \sum_{i=1}^{N_l} \left(\tilde{r}_s(t_i) - y\left(t_i; \sigma^{o}_{\mathrm{surf}}, \sigma^{o}_{\mathrm{vol}}, k_e, \gamma, \bar{t}\right)\right)^2 \qquad (2.4.25)$$

The main concern of this chapter is the scattering behaviour of the snow, and this is parameterised fully by the subset of three parameters $\sigma^{o}_{\mathrm{surf}}$, $\sigma^{o}_{\mathrm{vol}}$ and k_e. Figure 2.7 shows the fit to the deconvolution. Both terms of the fitted function y are shown separately: $\sigma^{o}_{\mathrm{surf}}$ is the integral of the surface term; $\sigma^{o}_{\mathrm{vol}}$ is the integral of the volume term, and the product $c_{ice} k_e$ determines the decay constant; dividing this product by

$c_{ice}=2.35\times10^8$ ms^{-1}, which is appropriate for typical snow densities (Matzler 1996) gives an estimate of k_e. The values obtained from figure 2.7 were $\sigma^o_{\rm surf}$=9.3 dB, $\sigma^o_{\rm vol}$=11.1 dB and k_e=0.23 m^{-1}.

2.5 An assessment of the errors in the scattering parameters

The effects of speckle noise and instrumental fluctuations

Because of speckle noise, there will be errors in the average echo $\tilde{p}$, the deconvolution $\tilde{r}$, and the retrieved estimates of $\sigma^o_{\rm surf}$, $\sigma^o_{\rm vol}$ and k_e. This section is concerned with the magnitude of these errors.

Because the echo power is exponentially distributed, an unbiased estimate of the variance of the speckle noise $v(M,t)$, affecting the telemetered echo $p(M,t)$, is given by

$$\left\langle v^2(M,t)\right\rangle = \frac{p^2(M,t)}{N_{av}+1} \tag{2.5.1}$$

where the angled brackets denote the expected value and N_{av} is the number of echoes averaged on-board to obtain $p(M,t)$. In designing the altimeter, the sampling rates in time delay and distance along track are chosen so that the speckle noise is largely decorrelated between samples, so that

$$\left\langle \mathrm{v}(M_k,t_l)\mathrm{v}(M_{k'},t_{l'})\right\rangle \approx \frac{p^2(M_k,t_l)}{N_{av}+1}\delta_{kk'}\delta_{ll'} \tag{2.5.2}$$

in which $\delta_{ll'}$ is the Kronecker delta. Under these circumstances, an estimate for the speckle variance $\hat{\sigma}^2_{\tilde{p}}$ on the average echo samples $\tilde{p}(t_i)$ is given by

$$\hat{\sigma}^2_{\bar{p}}(t_i) = \sum_{k=1}^{N_k} \tilde{W}^2(M_k)\frac{\hat{p}^2(M_k,t_l)}{N_{av}+1} \tag{2.5.3}$$

Figure 2.8a shows an average of 40,000 echoes from the South Pacific $(45-50°\text{S},\ 90-120°\text{W})$ - the ocean provides a more homogenous target than the ice sheets, enabling averages to be formed from a greater number of echoes over a wider area, so reducing speckle noise. An expanded view of the trailing edge is shown in figure 2.8b along with an exponential fit to the data. The average echo exhibits fluctuations on the trailing edge too large to be explained by speckle noise: the error bars are 95% confidence intervals calculated using equation (2.5.3).

Virtually identical fluctuations were reproduced using different ERS-1 data over different areas of ocean, indicating that they are an instrumental artefact. The most likely cause for the fluctuations is slight variations in the response of the IF filter mentioned in section 2.3. Corrections for these 'IF fluctuations' are supplied with the ERS-1 altimeter data and were applied; however, they obviously do not remove all of the variance. The standard deviation of the remaining IF fluctuations was found to be about 0.5% of the echo power, independently of the number of echoes averaged. This figure was obtained by calculating the variance of the departures from the exponential fit, and subtracting the variance expected due to speckle.

Combining the variances of IF fluctuations and speckle noise, the total variance $\sigma^2_{\bar{p}}$ becomes

$$\sigma^2_{\bar{p}}(t_i) = \hat{\sigma}^2_{\bar{p}}(t_i) + \left(0.005\tilde{p}(t_i)\right)^2 \tag{2.5.4}$$

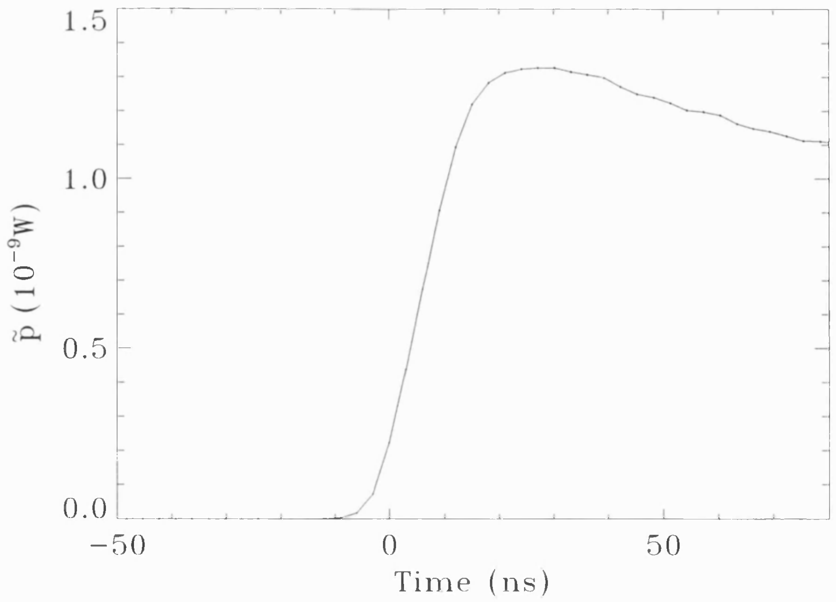

Figure 2.8a An average echo from the South Pacific. Even though 40,000 echoes were included in the average, fluctuation in power remain (see magnified section in figure 2.8b).

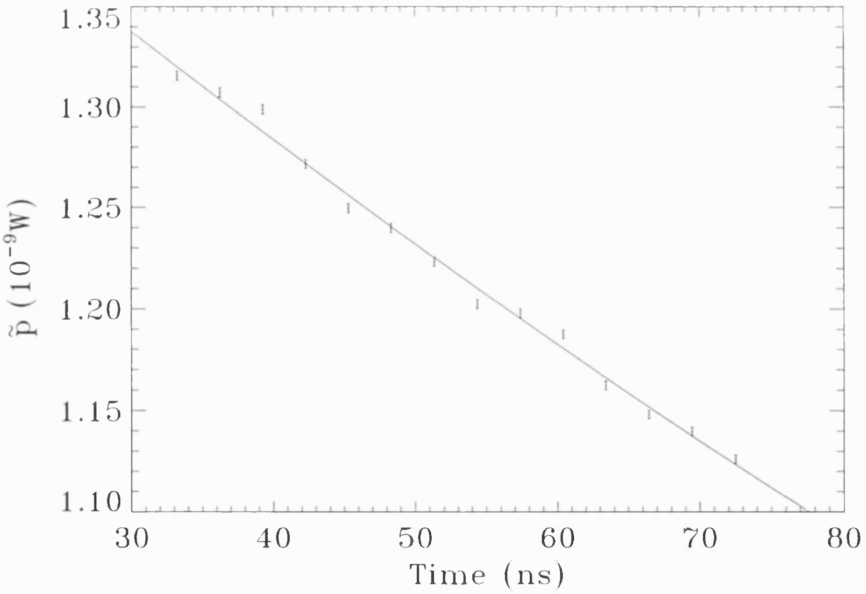

Figure 2.8b The fluctuations of figure 2.8a magnified and compared with an exponential fit (solid line). The fluctuations are too large to be explained by speckle noise (see the 95% confidence intervals for speckle, shown as error bars); they are also repeatable for different areas of ocean, which suggests they are an instrumental artefact.

Neither speckle noise nor the residual IF fluctuations are strongly correlated between samples, so, using equations (2.4.15 and 2.4.16), an estimate for the variance $\sigma_{\tilde{r}}^2$ on the samples $\tilde{r}(t_j)$ is given by

$$\sigma_{\bar{r}}^2\left(t_j\right)=\sum_{i=1}^{N_l}\left(a_{ji}^{reg}\right)^2\sigma_{\bar{p}}^2\left(t_i\right) \tag{2.5.5}$$

The errors in the retrieval of $\sigma_{\text{surf}}^{\text{o}}$, $\sigma_{\text{vol}}^{\text{o}}$ and k_e were estimated by Monte-Carlo simulation as follows. The fitted function $y(t;\sigma^0,\sigma_v,k_e,\gamma,t_c)$ was evaluated at each t_i and a random number $\rho\left(t_i\right)$was added to provide a simulated, noisy deconvolution. The errors on $\tilde{r}(t_j)$ are not necessarily uncorrelated between samples, so, to ensure that the correlation between the $\rho\left(t_i\right)$ was realistic, they were evaluated thus

$$\rho(t_i)=\sum_{j=0}^{N}a_{ij}^{reg}\vartheta_j \tag{2.5.6}$$

where the ϑ_j were uncorrelated, normally distributed, random numbers representing the uncorrelated speckle on the original echo samples $\tilde{p}\left(t_i\right)$. Using equation (2.5.6) simulates the processing applied by equations (2.4.15) and (2.4.16). The ϑ_j were generated with zero mean and standard deviation of $\sigma_{\bar{p}}^2\left(t_j\right)$ given by equation (2.5.4).

An ensemble of twenty simulated deconvolutions was generated and the non-linear least squares estimation procedure was applied to each, giving twenty sets of parameters $\sigma_{\text{surf}}^{\text{o}}$, $\sigma_{\text{vol}}^{\text{o}}$ and k_e. The standard deviation of the twenty values provides an estimate of the likely errors in each parameter. For the fit shown in figure 2.7, the 95% confidence intervals on each parameter are $\sigma_{\text{surf}}^{\text{o}}=9.3\pm0.2$ dB, $\sigma_{\text{vol}}^{\text{o}}=11.1\pm0.1$ dB and $k_e=0.23\pm0.01$ m^{-1}.

The number of simulated deconvolutions for which χ^2 is smaller than the value obtained by fitting to the actual deconvolution $\tilde{r}$ can be used to test the hypothesis that the discrepancy between $\tilde{r}$ and y is caused by speckle and IF fluctuations. If all twenty provide lower values of χ^2, then one can reject this hypothesis at the 95% significance level, and there must be some other source of error.

For the fit shown in figure 2.7, only two of the simulated deconvolutions gave lower χ^2 values, so the departure of the data from the model fit can confidently be attributed to speckle and IF fluctuations alone. In other areas the hypothesis was rejected (see figure 2.15). One possible cause for this is the distortion of the echoes introduced by topography. This would cause the approximation (2.4.20), and the model equation (2.4.24), to become inaccurate. This possibility is examined in the next section, using numerical simulations of the echoes over topographic surfaces.

Quantifying the effects of long scale topography

The estimation of $\sigma^{\circ}_{\text{surf}}$, $\sigma^{\circ}_{\text{vol}}$ and k_e was tested by numerically simulating 400 echoes over various computer generated random surfaces f_{long}. An average echo $\tilde{p}_{sim}$ was formed from the simulated echoes, and a deconvolution $\tilde{r}_{sim}$ determined. The simulations reveal the departure of J from the Gaussian form assumed by equation (2.4.20) and the resulting errors in $\sigma^{\circ}_{\text{surf}}$, $\sigma^{\circ}_{\text{vol}}$ and k_e. This section describes these calculations in more detail.

To evaluate equation (2.2.15) numerically, it is useful to replace the (ρ, ϕ) coordinate system with a Cartesian system (x, y), defined as follows

$$\begin{aligned} x &= x(M) + 2R\cos(\rho - \rho_{\text{SM}})\sin\frac{\phi}{2} \\ y &= y(M) + 2R\sin(\rho - \rho_{\text{SM}})\sin\frac{\phi}{2} \end{aligned} \tag{2.5.7}$$

A grid (x_n, y_m) was then defined such that

$$\begin{aligned} x_n &= nd, \quad n = 1, 2, \ldots, N_x \\ y_m &= md, \quad m = 1, 2, \ldots, N_y \end{aligned} \tag{2.5.8}$$

The spacing d between grid points was set equal to 100 m. N_x and N_y were both set equal to 1024 so the grid covered an area about 100 km by 100 km - similar to the weighted regions used for the real data. The individual echoes were simulated using the following expression, which was derived by substituting equations (2.5.7) into (2.2.15) and replacing integrals by sums over the discrete grids (x_n, y_m) in space and t_l in time delay

$$p_{sim}(t_i + t_0(M_k)) = \frac{E_t \lambda^2 d^2 \Delta_t}{(4\pi)^3 h_0^4 L_s} \sum_{l=1}^{N_l} \tilde{s}(t_i - t_l) \sum_{n=1}^{N_x} \sum_{m=1}^{N_y} g^2 \left(\frac{\sqrt{(x_n - x(M_k))^2 + (y_m - y(M_k))^2}}{h_0} \right) \cdot$$
$$D\left(t_l - \frac{\left((x_m - x(M_k))^2 + (y_n - y(M_k))^2\right)\eta}{ch_0} + \frac{2 f_{long}(x_n, y_m)}{c} - \frac{2h_0}{c} - \frac{2\delta h(M_k)}{c} + t_0(M_k) \right) \tag{2.5.9}$$

In equation (2.5.9) the convolution of the Gaussian approximations to D_{short} and q has been carried out analytically giving

$$D(t) = \frac{1}{\sqrt{\pi(\gamma_q^2 + \gamma_{short}^2)}} exp\left[-t^2 / (\gamma_q^2 + \gamma_{short}^2)\right] \tag{2.5.10}$$

The convolution with s is approximated numerically using

$$\tilde{s}(t_i - t_l) = \begin{cases} \dfrac{\sigma^{\circ}_{\mathrm{surf}} \delta_{il}}{\Delta_t} + \sigma^{\circ}_{\mathrm{vol}} c_{ice} k_e \, exp\left[-c_{ice} k_e (t_i - t_l)\right], & t_i \geq t_l \\ 0, \quad t_i < t_l \end{cases} \tag{2.5.11}$$

The value of $t_0(M_k)$ was set equal to the minimum time delay to the surface f_{long}, given by

$$t_0(M_k) = \min_{\forall n,m}\left(\frac{\left((x_n - x(M_k))^2 + (y_m - y(M_k))^2\right)\eta}{ch_0} - \frac{2f_{long}(x_n, y_m)}{c} + \frac{2h_0}{c} + \frac{2\delta h(M_k)}{c}\right) \tag{2.5.12}$$

Some simulations were performed where the value of $t_0(M_k)$ from equation (2.5.12) was adjusted by applying the OCOG retracking algorithm to the simulated echoes, but this made very little difference to the results.

Having simulated the echoes, an average echo was constructed as follows

$$\tilde{p}_{sim}(t_i) = \sum_{k=1}^{N_k} \tilde{W}(M_k) p_{sim}(t_i + t_0(M_k)) \tag{2.5.13}$$

where the 400 altimeter locations M_k were chosen to lie on a 20 by 20 rectangular grid with spacing 4 km between grid points. The weighting function $\tilde{W}(M_k)$ was calculated using equation (2.4.6), with the point S lying at the centre of the grid representing the simulated terrain. For Gaussian distributed, uncorrelated $f_{long}(x_n, y_m)$, the average echo can be calculated analytically using equations (2.2.37) - (2.2.39) and Appendix A, equations (A.4) - (A.7): the difference between equation (2.5.13) and the analytical solution was less than 1%.

The simulated deconvolution was found using

$$\tilde{r}_{sim}(t_j) = \sum_{i=1}^{N_l} a_{ji}^{reg} \tilde{p}_{sim}(t_i) \tag{2.5.14}$$

Substituting equations (2.5.9) and (2.5.13) into equation (2.5.14) it is apparent that

$$\tilde{r}_{sim}(t_j) = \Delta_t \sum_{l=1}^{N_l} \tilde{s}(t_j - t_l) \tilde{J}_{sim}(t_l) \tag{2.5.15}$$

with

$$\tilde{J}_{sim}(t_l) = \sum_{i=1}^{N_l} a_{li}^{reg} \sum_{k=1}^{N_k} \tilde{W}(M_k) \frac{E_t \lambda^2 d^2}{(4\pi)^3 h_0^4 L_s} \sum_{n=1}^{N_x} \sum_{m=1}^{N_y} g^2 \left(\frac{\sqrt{(x_n - x(M_k))^2 + (y_m - y(M_k))^2}}{h_0} \right) \cdot$$

$$D\left(t_i - \frac{\left((x_m - x(M_k))^2 + (y_n - y(M_k))^2\right)\eta}{ch_0} + \frac{2f_{long}(x_n, y_m)}{c} - \frac{2h_0}{c} - \frac{2\delta h(M_k)}{c} + t_0(M_k) \right) \tag{2.5.16}$$

Equation (2.5.15) is the discrete equivalent of equation (2.2.42) and $\tilde{J}_{sim}(t_l)$ is a discretely sampled approximation to the function J. Thus, inspection of $\tilde{J}_{sim}(t_l)$ will reveal the distorting effect of the simulated topography f_{long}.

To obtain the random surfaces f_{long}, a two dimensional array of uncorrelated, Gaussian-distributed random numbers (one for each of the grid elements defined by equation 2.5.8) was convolved with a two dimensional Gaussian representing the desired autocorrelation function. The convolution was performed by multiplying the Fourier transforms of the uncorrelated array and the autocorrelation function, taking the inverse Fourier transform and normalising the result so that the desired variance was achieved. To prevent aliasing, the uncorrelated array was multiplied by a Gaussian window function before its Fourier transform was taken. All Fourier transforms were obtained with an FFT algorithm. Figure 2.9 shows an example of a random surface generated in this way with autocorrelation length of 5 km and standard deviation 10 m - typical values for the Antarctic plateau. The altimeter locations M_k and the dimensions of the footprint are also shown.

Figure 2.10 shows the average echoes $\tilde{p}_{sim}$ and the deconvolutions $\tilde{r}_{sim}$ obtained from the surface shown in figure 2.9. The scattering was simulated using values σ^{o}_{surf}=7 dB, σ^{o}_{vol} = 10 dB and k_e=0.1 m^{-1}. In figure 2.11 the corresponding $\tilde{J}_{sim}$ is shown, along with other examples for different autocorrelation lengths and standard deviations. In all plots, the case $f_{long} = 0$ is shown for comparison. The prediction of section 2.2 that

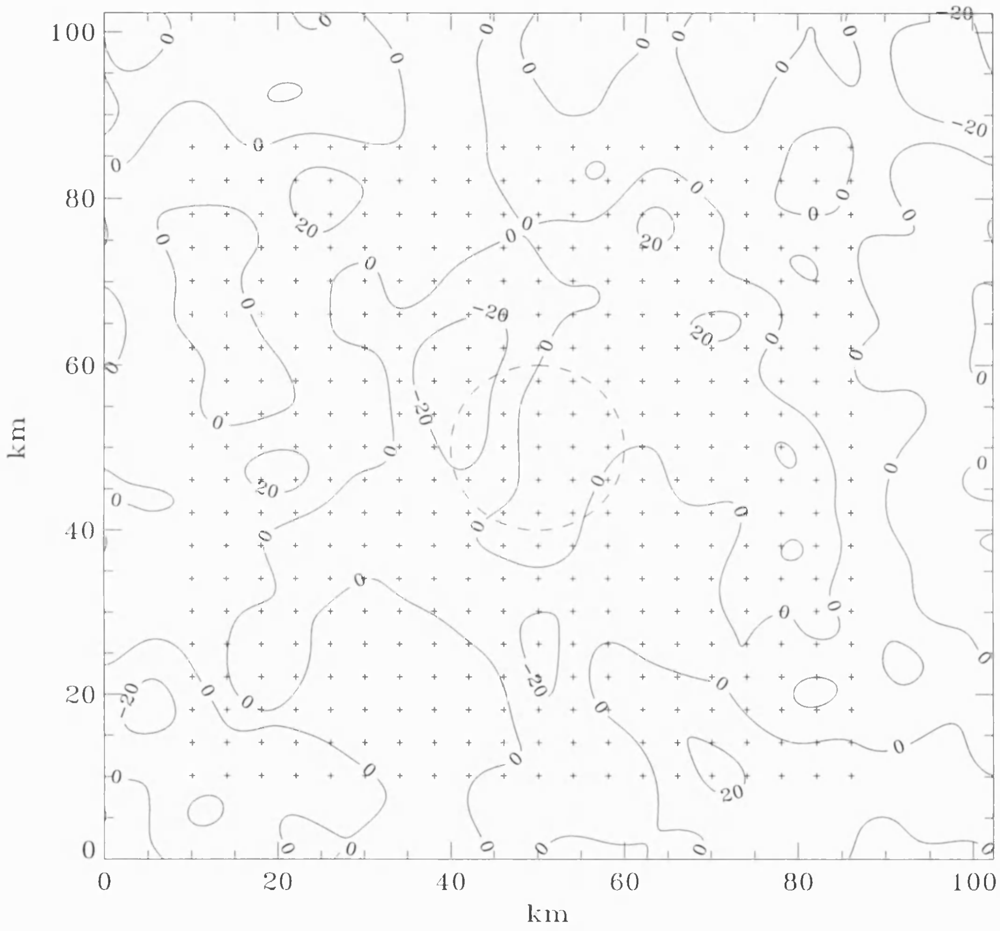

Figure 2.9 Simulated ice sheet topography with standard deviation of 10 m and autocorrelation length of 5 km. The simulated altimeter locations are shown as crosses and the dimensions of the beam-limited footprint as a dashed circle.

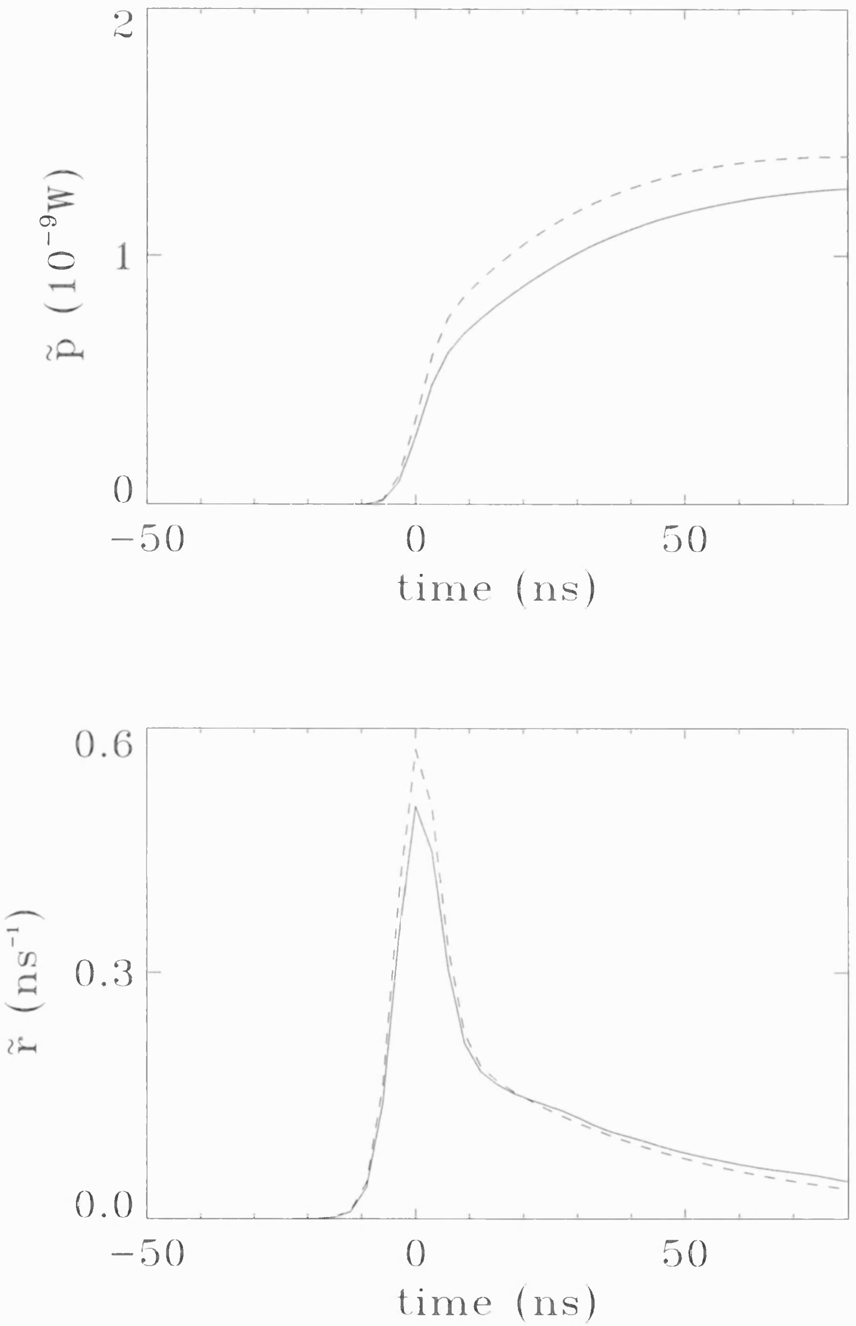

Figure 2.10 The average of the 400 simulated echoes from the locations shown in figure 2.9 (solid line). The deconvolution is shown beneath (solid line). The dashed lines show the results when the amplitude of the long scale topography is set to zero. The undulations cause power to be redistributed to later times - the effect mimics a smaller reflection at the air-snow interface, more sub-surface scattering and, a shallower decay.

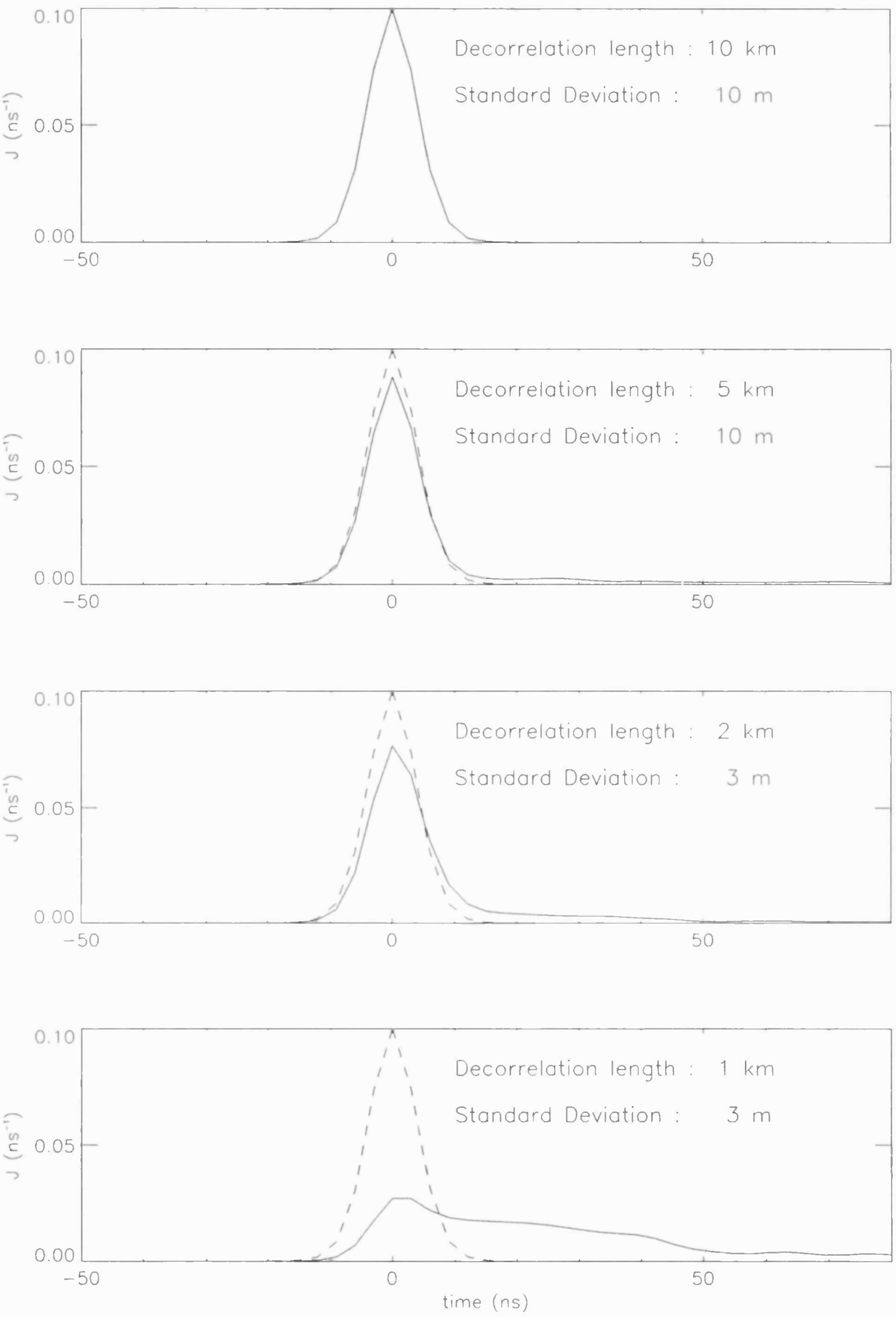

Figure 2.11a-d. The departures of J *from Gaussian for various horizontal scales and amplitudes of simulated undulations. The distortion for the surface shown in figure 2.9 is shown in figure 2.11b. Longer wavelength undulations (figure 2.11a) cause less distortion, while shorter wavelength undulations (figure 2.11c) cause comparable distortion even for smaller amplitudes. The distortion becomes extreme for very short wavelength undulations figure 2.11d. The dashed lines show the distortion free case when the amplitude of the undulations is zero.*

the long scale topography causes power to be shifted to later in the echo is borne out by the simulations. The distortion is very small for undulations on a horizontal scale of 10 km and amplitude of order 10 m, becoming much more significant for shorter wavelength undulations. For 1 km undulations of a few metres amplitude, the assumption that J is Gaussian is gravely inaccurate.

The non-linear least-squares fitting procedure described in section 2.4 was used to derive values of σ^{o}_{surf}, σ^{o}_{vol} and k_e from the $\tilde{r}_{sim}$ calculated for various f_{long}. When J departs from a Gaussian, the redistribution of power to later times causes σ^{o}_{surf} to be underestimated, and σ^{o}_{vol} overestimated. There will also be an error in the retrieved value of k_e. Table 2.1 shows the errors in each parameter for the surface shown in figure 2.9 and four different scattering parameterisations.

Table 2.1 The errors in σ^{o}_{surf}, σ^{o}_{vol} *and* k_e *caused by the topographic undulations shown in figure 2.9 for various scattering conditions.*

Scatttering			Errors		
σ^{o}_{surf} (dB)	σ^{o}_{vol} (dB)	k_e (m^{-1})	σ^{o}_{surf} error (dB)	σ^{o}_{vol} error (dB)	k_e error (m^{-1})
4	7	0.1	-1.7	0.3	-0.015
10	7	0.1	-0.8	1.4	-0.008
4	7	0.3	-1.3	0.5	-0.059
10	7	0.3	-0.9	1.3	-0.083

The results of these simulations suggest that, for undulations typical of those found in Antarctica and Greenland, the major source of error in estimates of σ^{o}_{surf}, σ^{o}_{vol} and k_e is a systematic error due to the topography of the ice sheets - the errors shown in table 2.1 are larger than the errors caused by speckle noise and IF fluctuations. The errors in σ^{o}_{surf} and σ^{o}_{vol} are likely to be 1 dB or so, and errors in k_e between 10-20%. Errors of similar magnitude or smaller were observed for the cases shown in figures 2.11a and 2.11c. For the case shown in figure 2.11d the errors were much larger.

Because the magnitude of the topographic error is sensitive to the amplitude and horizontal scale of undulations, it is difficult to quantify this error unless precise (~1m accuracy), high resolution (~1 km) information about the topography in an area is available. However, it will be shown in the next chapter that studying time varying signals can overcome this problem and reveal directly the distortion of the echoes by the long scale topography.

2.6 Results from Antarctica

Dates and locations of the ERS-1 data used

The methods described in section 2.4 were applied to ERS-1 data from cycles 87, 89 and 97 of the 35 day repeat phase of the mission. Table 2.2 shows the dates of the start and end of each of these cycles. For these cycles, the altimeter was operated in the higher bandwidth ocean mode, even over Antarctica, enabling the reflection from the surface to be distinguished from the exponentially decaying contribution from the volume - this is an essential requirement for the successful retrieval of σ^{o}_{surf}, σ^{o}_{vol} and k_e which was not met by deconvolutions obtained using the lower bandwidth ice mode echoes.

Table 2.2 The dates of the ERS-1, ocean-mode, 35 day repeat cycles used.

35 day repeat cycle	Start date	End date
87	14 / 08 / 1992	18 / 09 / 1992
89	23 / 10 / 1992	27 / 11 / 1992
97	30 / 07 / 1993	03 / 09 / 1993

The ERS-1 data were taken from 1195 regions in Antarctica, each 100 km across. The regions were selected in relatively flat areas of the plateau to minimise the errors from topographic distortion of the echoes. A different reference sphere was used for each region, with each sphere broadly coincident with the local slope of the ice sheet. This allowed f to be constrained to less than 100m everywhere - a necessary condition for the use of approximations 2.2.5 to 2.2.10 (Wingham 1995). The central coordinates and radii of 1195 suitable spheres were provided by J.J Proud; their derivation is described in Proud (manuscript in preparation).

The boresight direction (Δ, ρ_{SM}) was calculated at the centre of each region by assuming it to be normal to the WGS84 reference ellipsoid. It was found that different value of h_0 were needed for each sphere to constrain δh to values smaller than about 100 m everywhere. These h_0 were determined by converting the ellipsoidal satellite coordinates into a cartesian system with origin at the centre of each sphere O, finding the average distance between O and the satellite for a representative selection of data, and subtracting the radius of the sphere.

Spatial variations in the scattering parameters

Spatial variations in scattering were studied using data from cycle 87. Values of $\sigma^{\text{o}}_{\text{surf}}$, $\sigma^{\text{o}}_{\text{vol}}$ and k_e were retrieved for each of the 1195 regions. The other cycles were used to study temporal changes in scattering (see chapter 3).

Figure 2.12 shows the retrieved $\sigma^{\text{o}}_{\text{surf}}$ values. The values range from about -8 dB to over 13 dB. Low values are observed in Wilkes Land and Mizuho Plateau where katabatic winds are strongest (see figure 2.18 for the locations of regions mentioned by name). The highest values are observed in Dronning Maud Land. Figure 2.13 shows the retrieved $\sigma^{\text{o}}_{\text{vol}}$ values. The spatial variations are less than for $\sigma^{\text{o}}_{\text{surf}}$, ranging from about 4 dB to 16 dB. In most areas $\sigma^{\text{o}}_{\text{vol}}$ is larger than $\sigma^{\text{o}}_{\text{surf}}$, indicating that most

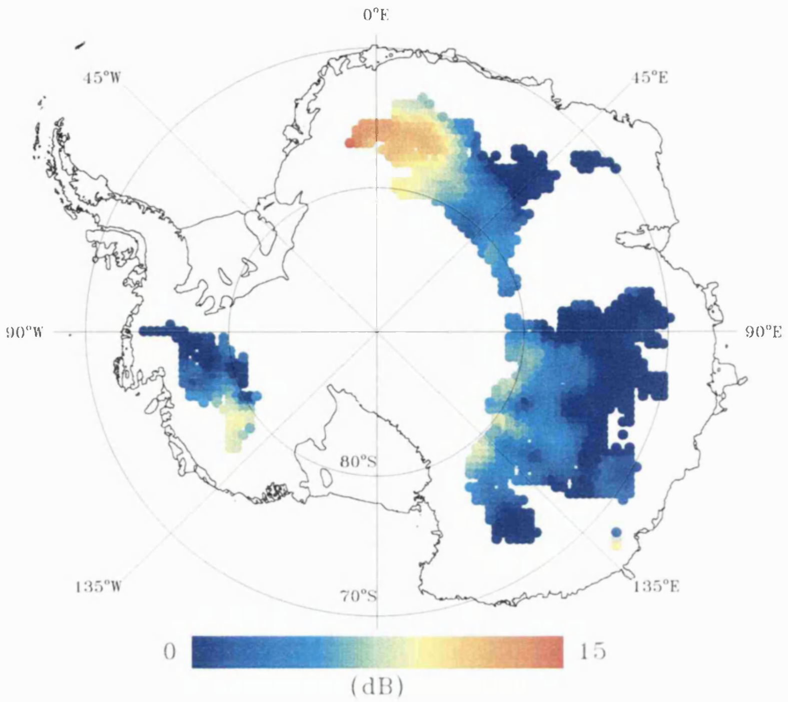

Figure 2.12 Spatial variations in surface reflection σ^{o}_{surf}*, September 1992.*

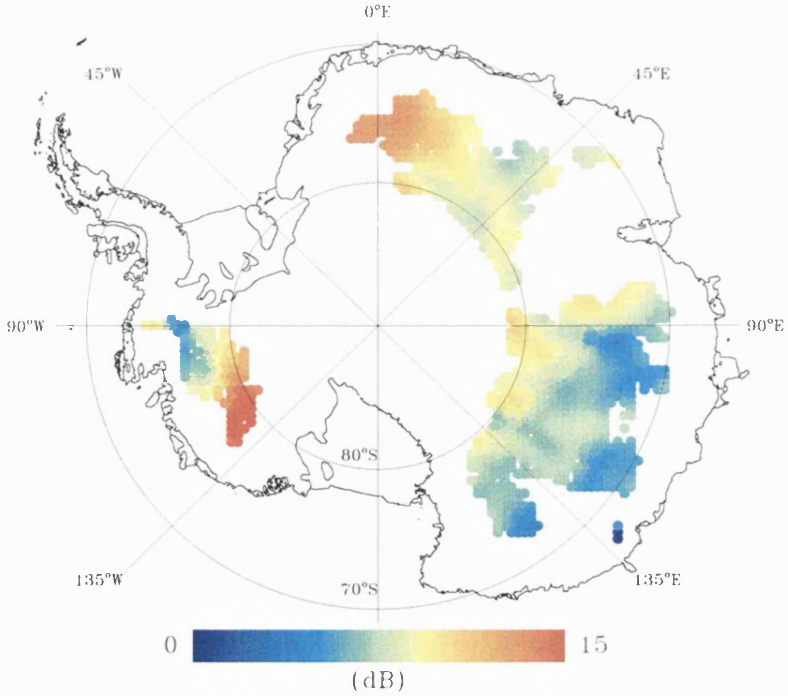

Figure 2.13 Spatial variations in subsurface scattering σ^{o}_{vol}*, September 1992.*

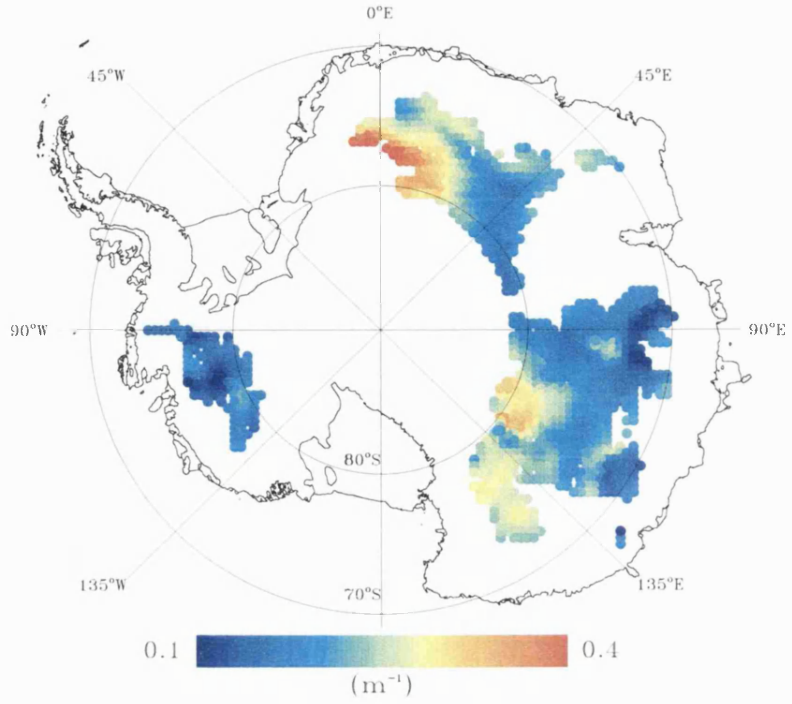

Figure 2.14 Spatial variations in extinction coefficient k_e*, September 1992.*

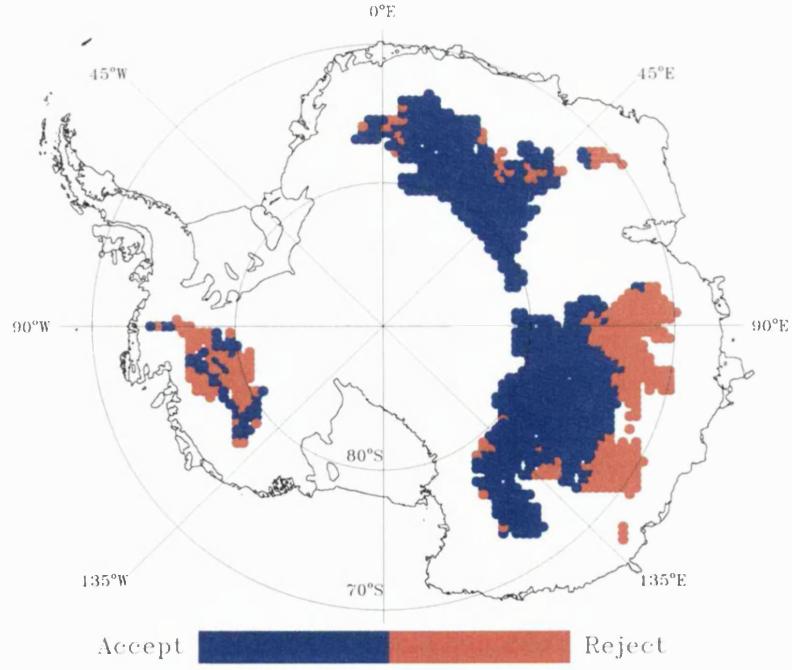

Figure 2.15 Results of testing the hypothesis that the discrepancy between the deconvolutions and the model equation (2.4.24) is caused only by speckle noise and instrumental fluctuations.

of the received power is scattered from beneath the air snow interface rather than reflected from it. The largest percentage of the backscatter attributed to surface reflection is 60%, in Dronning Maud Land. As with $\sigma^{o}_{\mathrm{surf}}$, the lowest $\sigma^{o}_{\mathrm{vol}}$ values are found in the Wilkes Land and Mizuho Plateau regions and the highest in Dronning Maud Land and West Antarctica. Figure 2.14 shows the retrieved values of k_e. The extinction coefficient varies by a factor of four over the ice sheet, from about 0.1 m^{-1} to about 0.4 m^{-1}. The highest values are seen in Dronning Maud Land. Low values are seen in West Antarctica.

Figure 2.15 shows the results of the 'goodness of fit' test performed during the retrieval of the parameters (as described in section 2.4). The areas shown in red are those locations where the test failed at the 95% level of significance. In these areas the model defined by equation (2.4.21) does not fit the data within the expected errors calculated using equation (2.5.5). In the more undulating regions of the ice sheet, such as West Antarctica, the failure of the model is probably because the function J is not well approximated by a Gaussian. This conclusion is supported by the simulations described in section 2.5, and by the time varying observations described in the next chapter. In other areas, such as Wilkes Land and Mizuho Plateau, the model fails to fit the data because the decay in scattering with depth is not exponential - this observation is also returned to in the next chapter.

2.7 Chapter summary

On the plateau of Antarctica the majority of the backscattered power usually originates from beneath the air-snow interface. However, the extended coverage of ERS-1 does reveal regions where the surface reflection accounts for up to 60% of the total backscatter. The spatial variation in $\sigma^{o}_{\mathrm{surf}}$, $\sigma^{o}_{\mathrm{vol}}$ and k_e is considerable. The snow structure in regions of strong katabatic wind is markedly different from other locations on the Antarctic plateau. These spatial variations cannot be explained by speckle noise, instrumental fluctuations or errors introduced by the undulating topography. For typical wavelengths and amplitudes of undulations, the latter is the dominant source of error in measurements of $\sigma^{o}_{\mathrm{surf}}$, $\sigma^{o}_{\mathrm{vol}}$ and k_e.

The spatial variations observed in this chapter must be caused by changes in snow structure brought about by differences in the weather and climate across the ice sheet. In the next chapter, these data are used to establish whether the snow structure and scattering properties could change between elevation measurements and to quantify the errors this would cause in the geodetic determination of ice sheet mass balance.

3. The impact of changes in scattering upon the geodetic method

3.1 Introduction to possible scattering changes

To reveal which changes in snow structure will affect the scattering and cause errors in the geodetic method, it is important to quantify the relative importance of the three mechanisms shown in figure 2.1. To this end, the measured parameters σ^{o}_{surf}, σ^{o}_{vol} and k_e were compared with dual polarisation satellite microwave radiometer data (section 3.2), with observations from snowpits (section 3.3), and with the predictions of a numerical model of microwave radiative transfer in snow (section 3.4).

The changes in backscatter shown in figures 1.1b and 1.2b, were investigated using ERS-1 data and the methods described in chapter 2 (section 3.5). Other changes in scattering which may occur on timescales too long to be observed directly are also considered in section 3.5. In each case, the aim is to explain the link between the scattering changes and the elevation error, and to make some predictions about the potential accuracy of elevation changes measured by radar altimeters operating over ice sheets.

3.2 Comparison with passive microwave data

The Scanning Multi-Channel Microwave Radiometer (SMMR) operated from 1978 to 1987, measuring brightness temperatures at 50° incidence angle. The radiometer supported several frequency channels, each measured at horizontal and vertical polarisation. The Nimbus 7 satellite carrying the radiometer was in a near polar orbit which provided almost total coverage of the polar regions every three days. The SMMR radiometer was superseded by the Special Sensor Microwave/Imager

(SMM/I) radiometer in 1987. SMM/I carried similar frequency channels except the lowest frequency 6.6 GHz channel was not included.

Brightness temperatures are affected by the physical temperature of the emitting snow and by its scattering properties. To study the scattering properties in isolation a mean emissivity $\varepsilon_\alpha(\nu)$ was defined as follows (Zwally 1977),

$$\varepsilon_\alpha(\nu) = \frac{\overline{T_{B\alpha}(\nu)}}{\overline{T}} \tag{3.2.1}$$

where $\overline{T_{B\alpha}(\nu)}$ is the mean brightness temperature from SSM/I data ($\alpha = h, v$ is the polarisation and ν is the frequency). $\overline{T}$ is the mean physical temperature at each site, and was calculated from the 6.6 GHz SMMR brightness temperatures using the following formula (D.P. Winebrenner; manuscript in preparation)

$$\overline{T} \approx \frac{\overline{T_{Bv}(6.6GHz)}}{\left(1.0026 - 0.4613\dfrac{\overline{T_{Bv}(6.6GHz)} - \overline{T_{Bh}(6.6GHz)}}{\overline{T_{Bv}(6.6GHz)} + \overline{T_{Bh}(6.6GHz)}}\right)} \tag{3.2.2}$$

Before using equation (3.2.2), a calibration correction of 7 K was added to $\overline{T_{Bv}(6.6GHz)}$ - this offset was determined by comparing SMMR and ground based radiometric observations of melting snow (D.P. Winebrenner; manuscript in preparation). After this calibration, equation (3.2.2), which is based upon calculations using a layered-medium, microwave scattering model, is accurate to a few K.

Modelling and empirical investigations (Fily and Benoist 1991; Surdyk and Fily 1995) show that areas of large grain size are revealed by high values of reflectivity $r_v = 1 - \varepsilon_v$, particularly at the 19 GHz and 37 GHz frequencies, and that areas where the snowpack is strongly stratified or where the reflection from the surface is strong

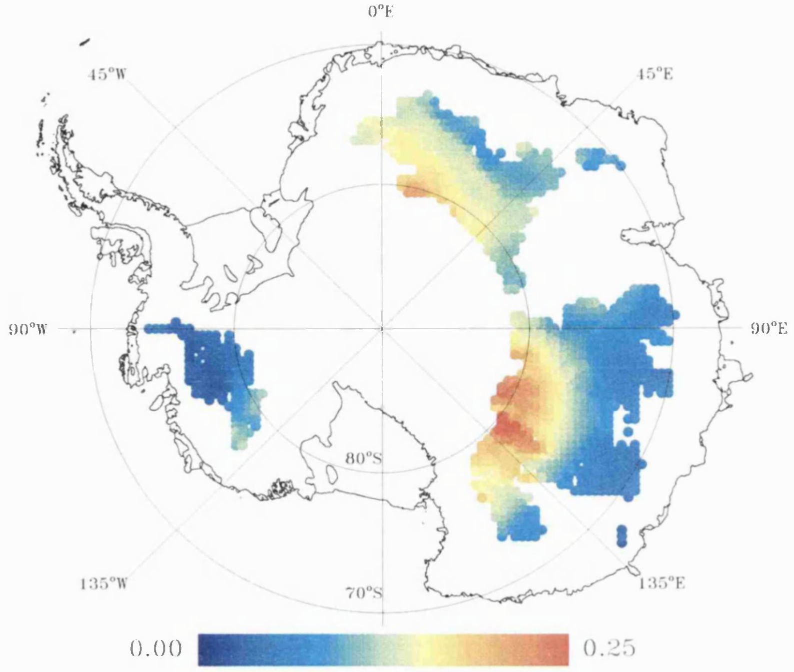

Figure 3.1 Spatial variations in the vertically polarised reflectivity, r_v(19 GHz).

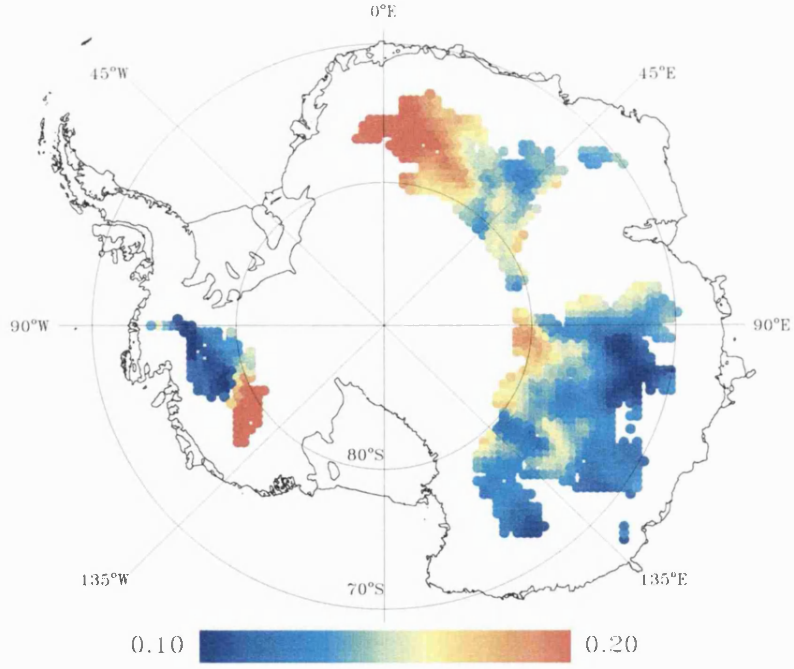

Figure 3.2 Spatial variations in the emissivity polarisation, Δ_{vh}(19 GHz)

are revealed by high values of the polarisation difference $\Delta_{vh} = \varepsilon_v - \varepsilon_h$. The parameters r_v(19 GHz) and Δ_{vh}(19 GHz) are shown in figures 3.1 and 3.2.

Table 3.1 The correlation matrix for parameterisations of the scattering from the satellite radiometer and the altimeter . All correlations are significant at the 95% level.

	r_v(19 GHz)	Δ_{vh}(19 GHz)	σ^o_{surf}	σ^o_{vol}	k_e
r_v(19 GHz)	1.0	0.3	0.5	0.2	0.6
Δ_{vh}(19 GHz)	-	1.0	0.8	0.9	0.4
σ^o_{surf}	-	-	1.0	0.7	0.5
σ^o_{vol}	-	-	-	1.0	0.1
k_e	-	-	-	-	1.0

Table 3.1 shows the correlations between r_v(19 GHz), Δ_{vh}(19 GHz), σ^o_{surf}, σ^o_{vol} and k_e. The strongest correlations are between σ^o_{surf}, σ^o_{vol} and Δ_{vh}(19 GHz) (compare figures 2.12, 2.13 and 3.2) and between r_v(19 GHz) and k_e (compare figures 2.14 and 3.1). This suggests that the backscatter is largely due to reflections taking place at the air-snow interface or at layers of different density, while the dominant mechanism causing extinction is scattering by the closely packed snow grains. It is reasonable that scattering by snow grains causes large extinction with depth, but low backscatter, because the scattered radiation is virtually isotropic, so only a small fraction is received by the altimeter. On the other hand, reflections from the horizontal layer interfaces are predominantly directed towards the satellite, so large backscatter is achieved for relatively little extinction.

3.3 Comparison with direct glaciological observations

In locations which have been visited by scientific expeditions, direct observations of the physical structure of the snowpack are available. Between December 5, 1967 and January 29, 1968, a series of 18 snowpits, each in excess of 2m deep, were dug by researchers from the Ohio State University (OSU) (Breuck 1968). The pits were spaced at intervals of about 80 km along the third leg of the South Pole to Queen Maud Land traverse (SPQMLT3). Figure 3.3 shows the route taken.

For each snowpit, measurements of snow density were made at 10 cm depth intervals. The maximum and minimum grain diameter in each 10 cm layer was also recorded. The accumulation rate for each pit was found by identifying layers contaminated by fallout from atomic bomb tests in the South Pacific in the 1950s. These measurements allow a fuller investigation of the relationship between the climate at a site, the physical structure of the snow, and its scattering properties.

Figure 3.4 shows the elevation, temperature, accumulation rate and the maximum grain diameter (averaged over samples from depths between 1 and 2 m) along the SPQMLT3 route. In considering the scattering properties of the snow, the diameter of the largest grains is more relevant than that of the smallest grains because large grains have a disproportionately higher radar cross section (West et al. 1993). The grain size increases along the route, as the elevation falls and the temperature increases - this is consistent with the knowledge that grains grow faster under higher temperatures (Maeno and Ebinuma 1983). The increase is not monotonic however, a maximum is observed at about 500 km, where the accumulation rate is very low. Here, the grains are buried slowly, and spend longer in the near-surface layer, where large temperature gradients promote crystal growth (Gow 1969; Colbeck 1983).

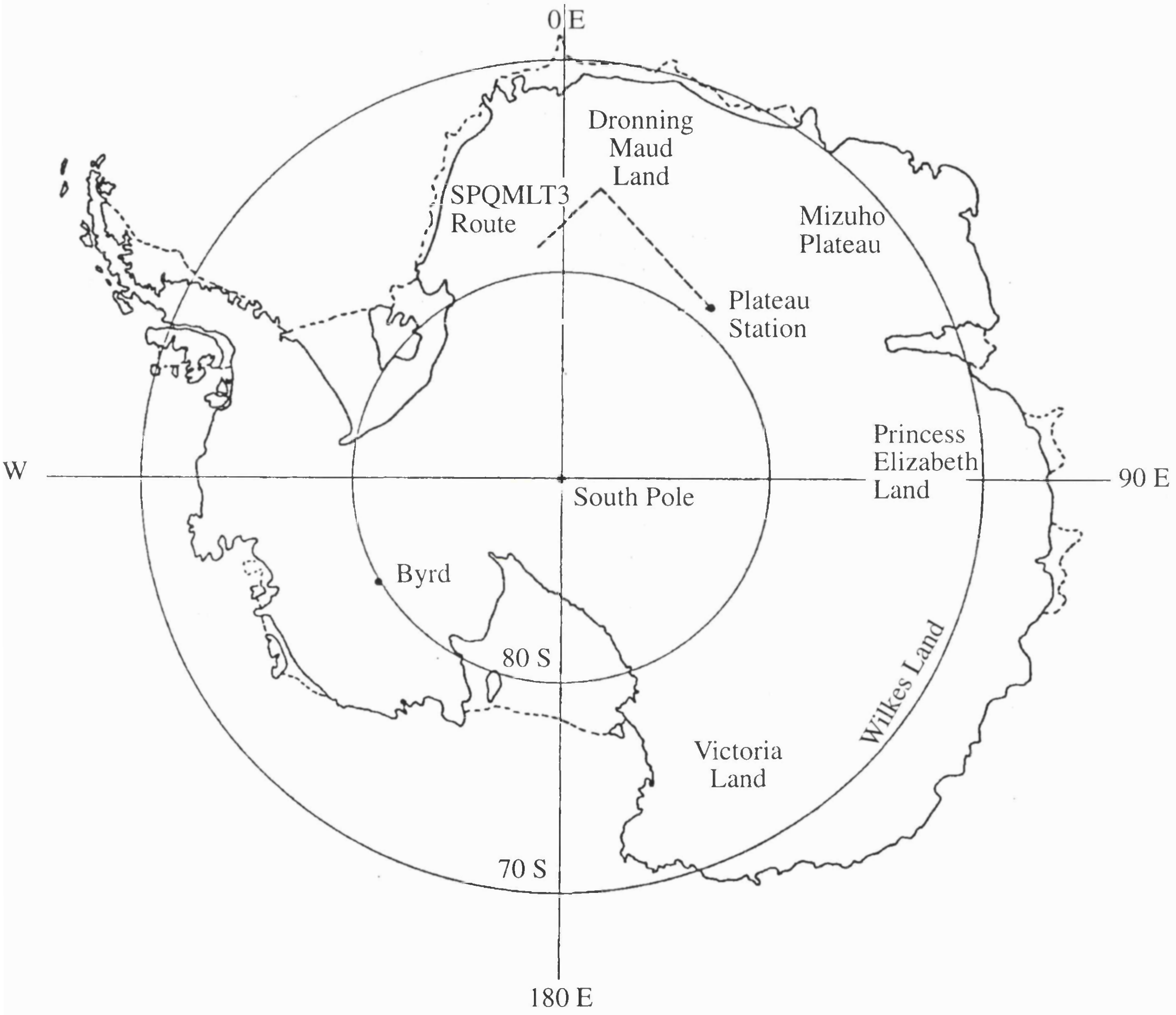

Figure 3.3 The route of the South Pole to Queen Maud Land Traverse (SPQMLT) and other locations mentioned in the text.

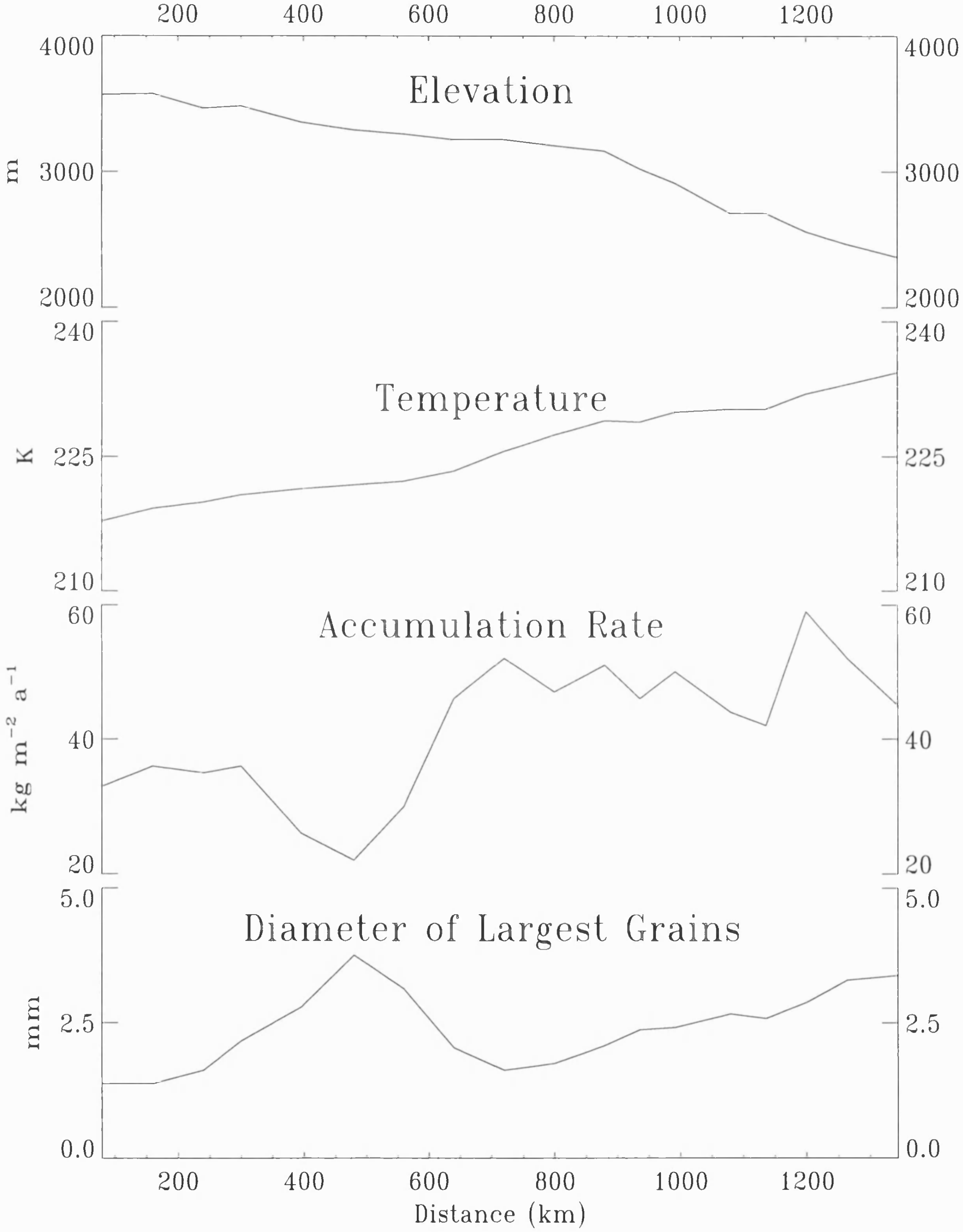

Figure 3.4 Variations in elevation, temperature, accumulation rate and the diameter of large grains along the third leg of the SPQMLT route.

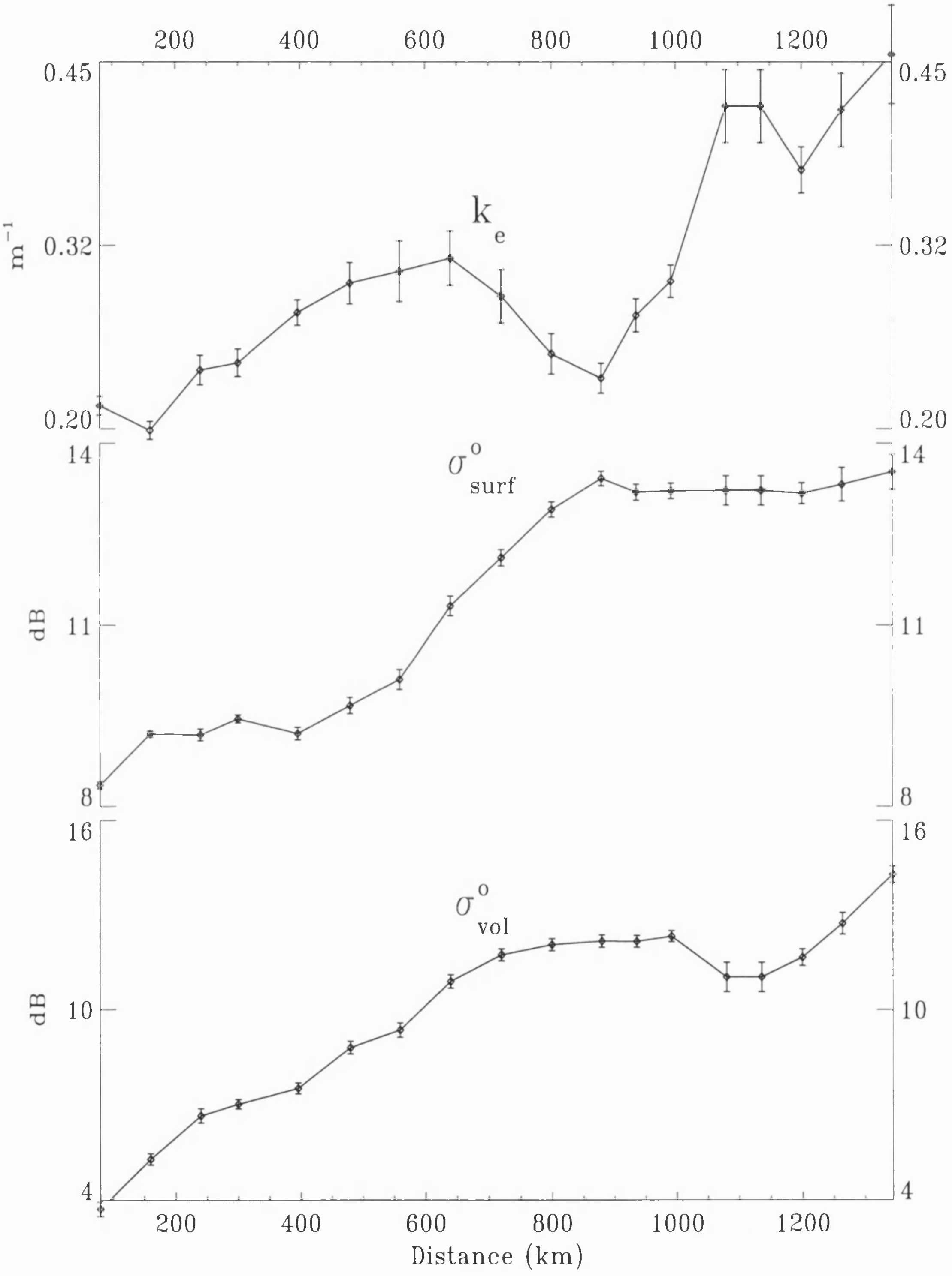

Figure 3.5 Variations in k_e, σ^o_{surf} *and* σ^o_{vol} *along the third leg of the SPQMLT route.*

Figure 3.5 shows the retrieved values of k_e, σ^o_{surf} and σ^o_{vol} along the route. The values of k_e show a similar trend to the grain size with a local maximum at about 600 km distance. The correlation coefficient between k_e and the grain diameter is 0.74, which is significant at the 95% level. There are several reasons why a lower correlation coefficient might be anticipated. Firstly, snow-pit data are local measurements while the values of k_e are representative of an area some 100 km across. Secondly, the properties of the snow may have changed since 1968. Thirdly, there will be errors in k_e, caused by speckle and by topographic undulations. Finally, the extinction may be affected by reflections at layer interfaces, or changes in density. Bearing these possible sources of decorrelation in mind, the significant correlation suggests that the size of snow grains is an important factor in determining the extinction coefficient of the snow.

As well as the 2 m deep snowpits, a series of shallower pits were dug at more frequent intervals along the same route. These observations are described in (Rundle 1971). Until 500 km the 1967 surface layer is described as 'generally soft and fine grained'. Figure 3.5 shows that in 1992 σ^o_{surf} from this leg of the traverse is relatively low. Between 500 and 800 km the surface layer is described as 'generally fine grained, but varying considerably in hardness between pits, from very hard wind-packed layers to extremely soft, undisturbed snow'. Figure 3.5 shows intermediate values of σ^o_{surf} over this leg of the traverse. Over the final leg of the traverse, from 800 to 1350 km, Rundle reports that 'frequently, there was no fine material at the surface'. Here σ^o_{surf} is at its highest. The correspondence between the different surface types described by Rundle and the σ^o_{surf} values reveals that the reflection from soft, fine grained snow is less than from wind-packed layers, unless, of course, the large scale spatial distribution of these types of snow has reversed since the SPQMLT3 traverse, which seems unlikely.

Rundle also describes the extent of subsurface layering along the traverse. Over the first 500 km, the surface layer was 'separated from lower, slightly coarser material by a thin hard layer, a series of fine crusts, or, occasionally, by a single crust'. Beyond 300 km the stratigraphy became 'more complex, with more intensive as well as extensive crust development' until about 800 km. Beyond 800 km, crust development became 'so extensive that interpretation (of annual layering) in the field was extremely difficult'. This increase in the development of buried crusts along the route is reflected in the increase of σ^{o}_{vol} shown in figure 3.5. There is no evidence for the local maximum of σ^{o}_{vol} which might be expected at about 500 km if scattering by snow grains were the dominant mechanism for scattering from beneath the surface.

To summarise, the field data from the SPQMLT3 traverse support the conclusions arrived at through studying the passive microwave data. Reflections at the air-snow interface and at buried crusts and other layer interfaces seem to account for most of the backscatter, while scattering from snow grains seems more important in attenuating the microwaves with depth than in returning power to the altimeter. These conclusions are necessarily tentative, since they are based only upon empirically observed correlations, which may turn out to be misleading - for instance, layers of large depth hoar crystals are often found beneath hard crusts (Alley et al. 1990; Colbeck 1983), so it is difficult to determine empirically whether an increase in backscatter is caused by scattering from the large crystals or by reflection from the crust. To test these conclusions more rigorously, a numerical model of electromagnetic scattering from snow was employed.

3.4 A numerical model of microwave scattering from snow.

The passive microwave data and the field data suggest that scattering models of the altimeter echo from dry snow should incorporate scattering from closely packed snow grains, reflections from internal layer interfaces and the reflection at the air-snow interface. Such a model has recently been developed by D. P. Winebrenner of the University of Washington (UW). In this section, the predictions of the UW scattering model are compared with the empirical observations.

The UW model treats microwave scattering from snow grains using Dense Medium Radiative Transfer (DMRT) theory, which models the snow structure as a suspension of spherical ice grains in air (Tsang et al. 1985). DMRT explicitly accounts for correlations between the positions of neighbouring grains, giving accurate predictions of radiative transfer for typical snow densities, without empirical correction. Previous models, which assumed independent scattering centres, required an empirical correction coefficient to match radiometric observations (Comiso and Zwally 1982).

Another advantage of the UW model over earlier scattering models is the inclusion of a stratified density profile through the snowpack. This allows reflections at interfaces between layers of different density to be incorporated using the numerical technique of invariant embedding (Tsang et al. 1985). Invariant embedding allows the inclusion in the model of multiple reflections, multiple scattering events, and combinations of reflection and scattering. A brief description of the methods employed by the model is given below.

The model solves the dense medium radiative transfer equation (Tsang et al. 1985; Ishimaru 1978)

$$\cos\theta\frac{\partial}{\partial z}\bar{\boldsymbol{I}}(z,\theta,\phi)=-\kappa_e\bar{\boldsymbol{I}}(z,\theta,\phi)+\int_0^{\pi}\sin\theta' d\theta'\int_0^{2\pi}d\phi'\bar{\bar{\boldsymbol{P}}}(\theta,\phi,\theta',\phi')\bar{\boldsymbol{I}}(z,\theta',\phi') \tag{3.4.1}$$

to find the specific intensity $\bar{\boldsymbol{I}}(z,\theta,\phi)$ within each layer. $\bar{\boldsymbol{I}}(z,\theta,\phi)$ is a vector, with elements comprised of the four Stokes parameters which describe the intensity and polarisation of the radiation (Tsang et al. 1985). Depth is denoted by z, and propagation direction by $(\theta,\ \phi)$, where θ is the angle from vertical and ϕ is the azimuthal direction: $\theta=0$ corresponds to radiation propagating vertically downward. $\bar{\bar{\boldsymbol{P}}}$ is the scattering phase matrix, which determines the scattering from direction $(\theta',\ \phi')$ into direction $(\theta,\ \phi)$. The local extinction coefficient within the layer is denoted by κ_e. In each layer, $\bar{\bar{\boldsymbol{P}}}$ and κ_e are calculated using the expressions given by West et al. (1993), which depend upon the density and the distribution of grain sizes assigned to the layer.

Following Ishimaru (1978), the specific intensity is decomposed into a 'reduced specific intensity' $\bar{\boldsymbol{I}}_r(z,\theta,\phi)$ and a 'diffuse specific intensity' $\bar{\boldsymbol{I}}_d(z,\theta,\phi)$, so that $\bar{\boldsymbol{I}}=\bar{\boldsymbol{I}}_r+\bar{\boldsymbol{I}}_d$ everywhere. Within each layer, the reduced intensity $\bar{\boldsymbol{I}}_r(z,\theta,\phi)$ is defined to be the solution to the equation

$$\cos\theta\frac{\partial}{\partial z}\bar{\boldsymbol{I}}_r(z,\theta,\phi)=-\kappa_e\bar{\boldsymbol{I}}_r(z,\theta,\phi) \tag{3.4.2}$$

The boundary conditions for $\bar{\boldsymbol{I}}_r(z,\theta,\phi)$ at the upper and lower interfaces of each layer satisfy plane-wave, Fresnel reflection and transmission for the discontinuity in effective permittivity.

The method of invariant embedding (Tsang et al. 1985) is used to propagate the solution for $\bar{\boldsymbol{I}}_r(z,\theta,\phi)$ throughout the stack of layers, taking account of all possible reflections between interfaces. The incident plane-wave intensity at the top of the stack provides the upper boundary condition $\bar{I}_r(z=0^+,\theta=0,\phi)$, where the superscript + indicates the value just above the air-snow interface at $z=0$. The lower boundary condition is supplied by the assumption that, beyond a certain depth z_{max}, the snowpack can be replaced by a homogenous half-space so that $\bar{I}_r(z=z_{max}^-,\theta=\pi,\phi)$ is zero. Because the intensity is attenuated with depth, the simulated, layered snowpack can always be made deep enough to accommodate this assumption.

The solution for $\bar{I}_d(z,\theta,\phi)$ is obtained by substituting $\bar{I}=\bar{I}_r+\bar{I}_d$ into equation (3.4.1) and solving the resulting equation numerically, making use of the previously determined solution for $\bar{I}_r(z,\theta,\phi)$. The boundary conditions at all layer interfaces are solved by invariant embedding, in a similar fashion to that used for $\bar{I}_r(z,\theta,\phi)$, except that the boundary conditions appropriate for reflection and transmission of a spreading wavefront are used at each interface instead of those for a plane wave. It is this difference in boundary conditions which makes the decomposition into $\bar{I}_r$ and $\bar{I}_d$ necessary.

Physically, the reduced intensity $\bar{I}_r(z,\theta,\phi)$ describes the propagation and reflections of the incident plane wave, including its attenuation by absorption and scattering. Thus, the reduced specific intensity emerging at the top of the simulated snowpack, $\bar{I}_r(z=0^+,\theta=\pi,\phi)$ reveals the contribution to the altimeter signal from reflections at the air-snow interface and internal layer interfaces (including multiple reflections). The diffuse intensity $\bar{I}_d(z,\theta,\phi)$, on the other hand, describes the propagation and reflections of all radiation which has been scattered at least once by snow grains within the snowpack. Thus $\bar{I}_d(z=0^+,\theta=\pi,\phi)$ reveals the contribution from scattering (including multiple scattering and all combinations of scattering and reflection).

The parameters describing the snowpack were taken from a traverse across Victoria Land (Stuart and Heine 1961). These data were more suitable for driving the scattering model than those recorded on the SPQMLT3 traverse, because, rather than sampling every 10 cm, the thickness and density of each identifiable layer within the snowpack were recorded. The density profile is well represented by a stochastic process with mean layer density 400 kg m^{-3}, standard deviation of layer densities 40 kg m^{-3}, and exponentially distributed layer thicknesses with a mean of 7 cm. The density is assumed homogenous within each layer. Five classifications of grain size (I to V) were distinguished in the snowpit. Table 3.2 shows the frequency of occurrence of each classification in the depth range 2-3 m (the frequencies are weighted by the thickness of each layer classified).

Table 3.2 Frequency of various snow grain classifications for the snowpit at 72S, 141E (from data in Stuart and Heine 1957).

Classification	Diameter (mm)	Frequency
I	0.0 - 0.5	68%
II	0.5 - 1.0	10%
III	1.0 - 2.0	15%
IV	2.0 - 3.0	5%
V	3.0 - 4.0	2%

Smaller grains (mostly class I) were reported in the upper metre but for simplicity the probabilities of table 3.2 were assumed to apply throughout the snowpack. For each of the classifications I to V, a grain size distribution was simulated using a log-normal distribution (Papoulis, 1991) with mean equal to the mid point of the range given in table 3.2 and standard deviation equal to 0.35 times the mean - this gives a more plausible population of grains for each classification than a uniform distribution between the two limits. Figure 3.6 shows an example of the simulated density and grain size profiles.

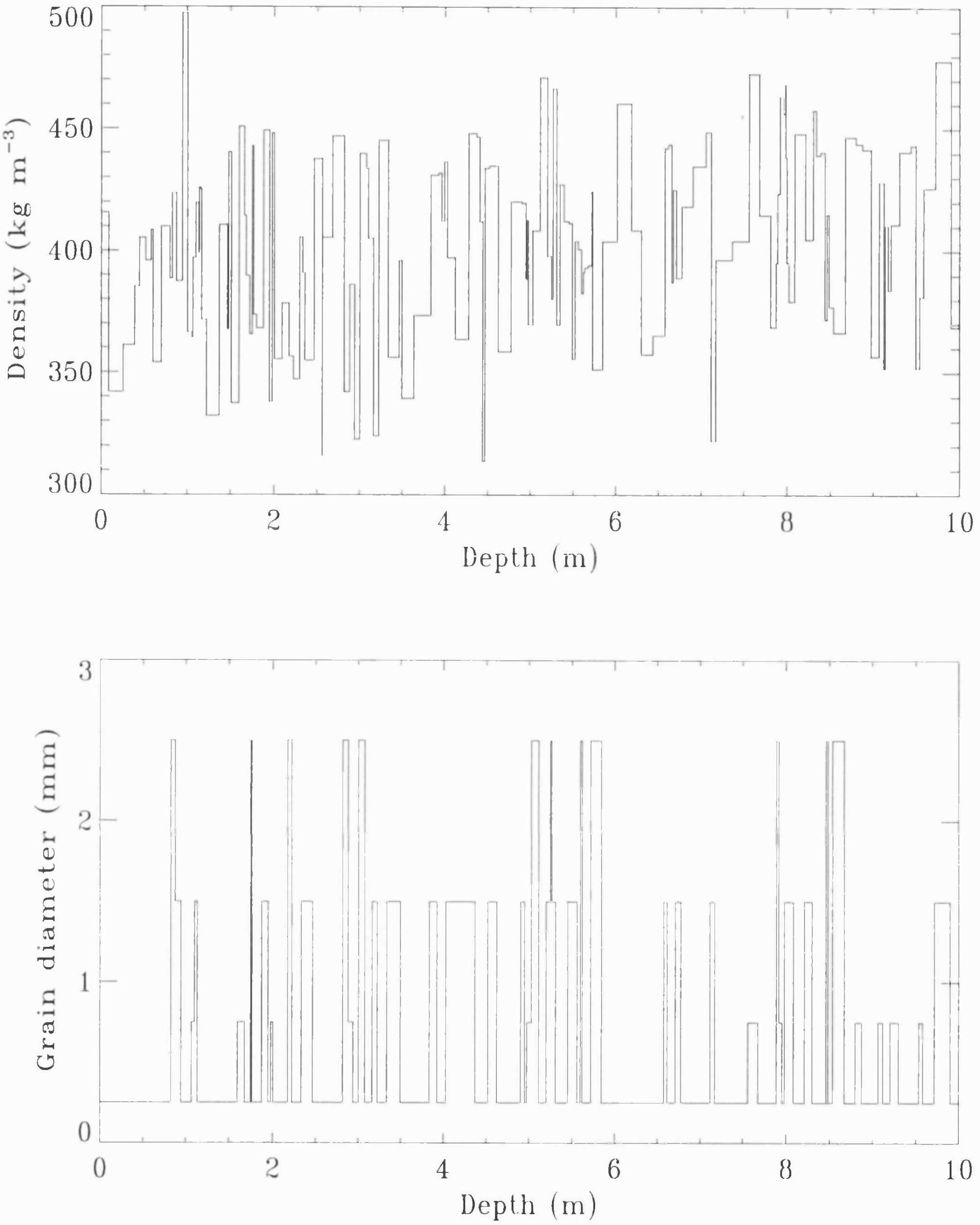

Figure 3.6 An example of simulated density and grain size profiles. The density profile was simulated by a stack of layers, with exponentially distributed thickness (mean 7 cm), mean density 400 kg m^{-3}, *and Gaussian distibuted fluctuations in density with standard deviation 40* kg m^{-3}. *Within each layer the grain size distribution was lognormal, with mean diameter chosen randomly from five possible classifications distinguished in the field. The probability of occurrence of each classification was chosen to match the observed frequencies in table 3.2.*

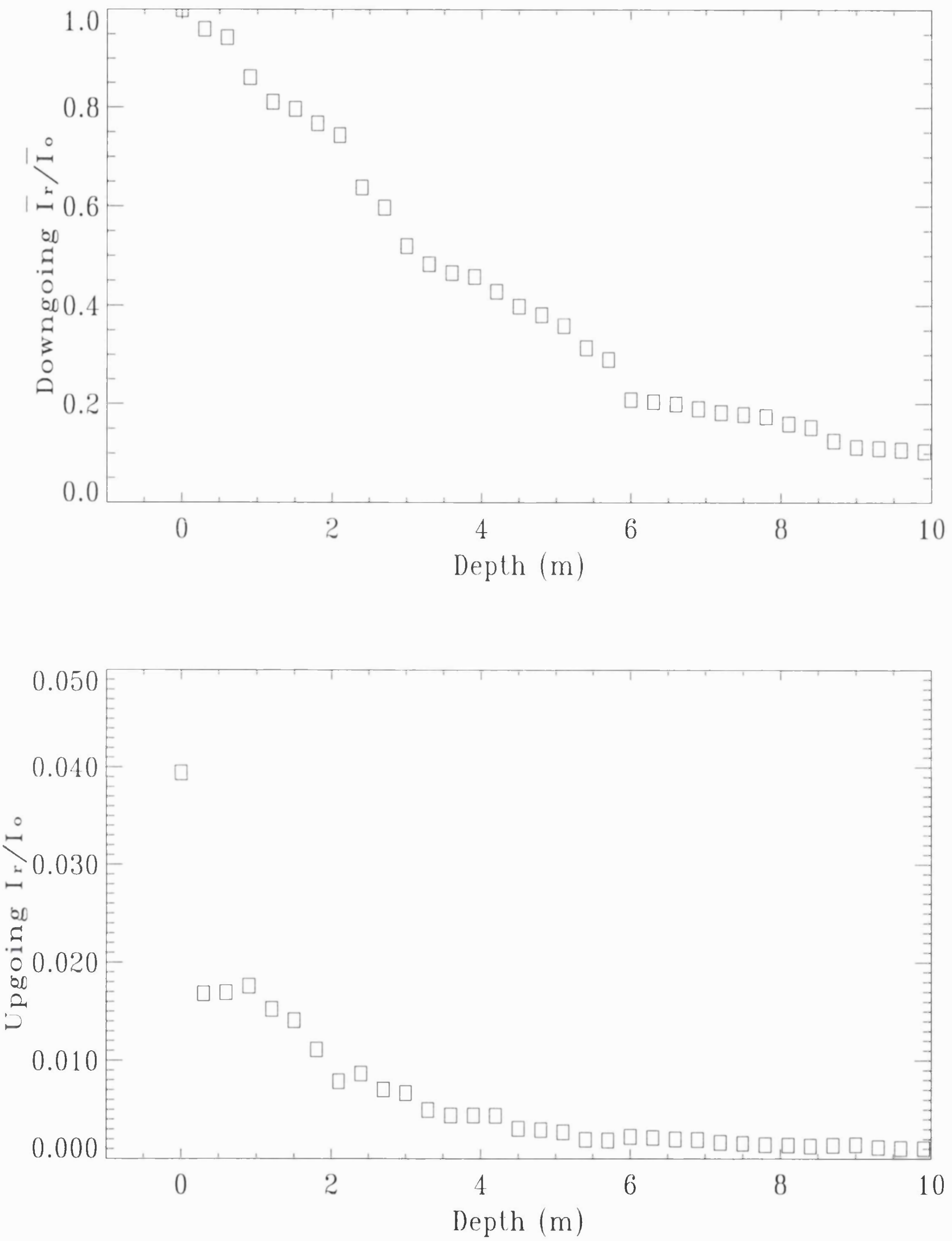

Figure 3.7a The downward propagating reduced intensity, simulated as a function of depth, for the density and grain size distribution shown in figure 3.6. The downward propagating plane wave is attenuated by absorption, scattering and reflections. Figure 3.7b The upwardly propagating reduced intensity arising from reflections at layer interfaces. Values are normalised with respect to the incident intensity.

When the incident radiation is a linearly polarised plane wave, the reduced intensity can be described everywhere by a single Stokes parameter (the plane-wave intensity), so a scalar notation can be adopted. Figure 3.7 shows the solution for reduced plane-wave intensity I_r as a function of depth for downgoing ($\theta = 0$) and upgoing ($\theta = \pi$) directions. The values are normalised by the incident intensity I_0. Scattering, absorption and reflection at layer interfaces all attenuate the downgoing solution: the extinction coefficient can be determined by fitting an exponential to the decay. The upgoing specific intensity is the sum of the reflection from the surface, visible in figure 3.7b as a sudden increase in $I_r(z, \theta = \pi, \phi)$ at $z = 0$, and an exponentially decaying contribution from reflections at deeper layer interfaces.

In practise, the layer interfaces are rough, not planar as assumed in the model. According to geometric optics (Tsang et al. 1985), the relationship between the surface backscatter $\sigma^{\circ}_{\mathrm{surf}}$, at vertical incidence, and S_{surf}, the RMS surface slope of the air-snow interface, is

$$\sigma^{\circ}_{\mathrm{surf}} = \frac{|R_{\mathrm{surf}}|^2}{2S^2_{\mathrm{surf}}} \qquad (3.4.3)$$

where R_{surf} is the Fresnel reflection coefficient of a planar air-snow interface, which may be calculated from the effective permittivity of the uppermost layer in the simulated snowpack. Figure 3.8 shows the dependence of $\sigma^{\circ}_{\mathrm{surf}}$ upon density and surface roughness of the uppermost layer. The observed range of $\sigma^{\circ}_{\mathrm{surf}}$ from -8 dB to 13 dB can be explained by variations in snow density from 200 to 450 kg m^{-3} and RMS slopes from 0.025 to 0.14 - these ranges correspond to the extremes of density and roughness reported from field measurements (Schytt 1958; Long and Drinkwater 1994).

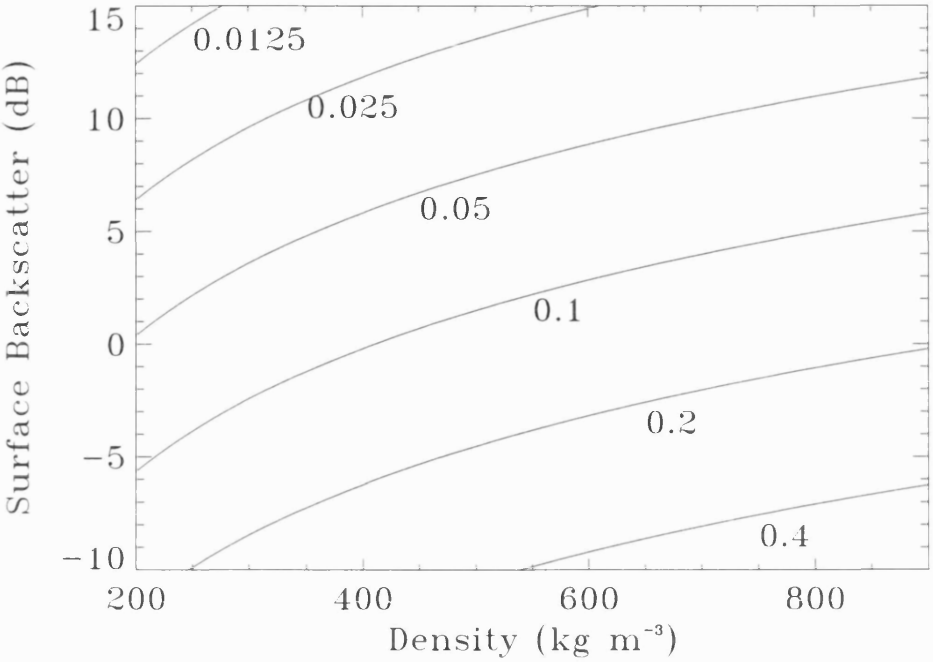

Figure 3.8 The variation in σ^{o}_{surf} *calculated as a function of density for several RMS roughnesses of the air-snow interfaces. The range of* σ^{o}_{surf} *values observed in figure 2.12 can be explained by plausible variations in surface roughness and density.*

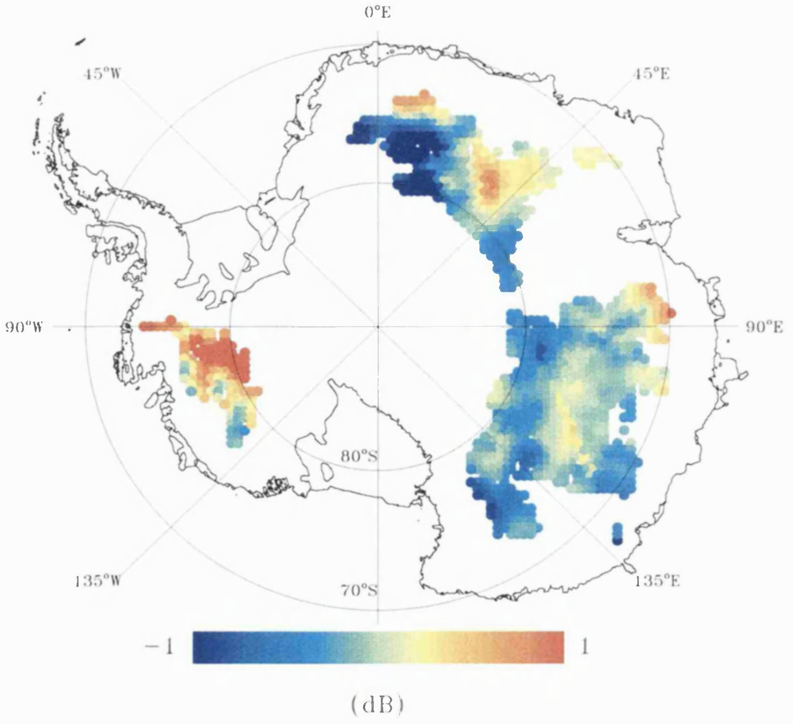

Figure 3.9 The change in backscatter between September 1992 and September 1993.

Subtracting the surface reflection from $I_r(z=0^+,\theta=\pi,\phi)$ gives the contribution to the volume backscatter $\sigma^{\mathrm{o}}_{\mathrm{vol}}$ caused by reflections at deeper layer interfaces. Assuming a representative value S_{vol} for the RMS slope of buried layer interfaces, the contribution to the backscatter from this source can be approximated by

$$\sigma^{\mathrm{o}}_{\mathrm{vol}}=\frac{1}{2S^2_{\mathrm{vol}}}\left[\frac{I_r(z=0^+,\theta=\pi,\phi)-\left|R_{\mathrm{surf}}\right|^2 I_r(z=0^+,\theta=0,\phi)}{I_r(z=0^+,\theta=0,\phi)}\right] \qquad (3.4.4)$$

Equation (3.4.4) is only an approximation because it neglects the effects of refraction, the variation of the transmission coefficient at each interface with incidence angle and the additional spreading undergone by multiple reflections. For vertical incidence, and for the relatively smooth interfaces and weak dielectric discontinuities found in snowpacks, these effects are assumed to be small.

Table 3.3 shows the predictions of equations (3.4.3) and (3.4.4) for the likely extremes of S_{surf} and S_{vol}, compared with the values retrieved from ERS-1 data at the location of the snowpit (72S, 141E). To match the measured backscatter data exactly, values of S_{surf}=0.11 and S_{vol}=0.05 must be assumed: both are plausible values, although, since one might expect similar roughnesses for buried interfaces and the present air-snow interface, it seems possible that the model slightly underestimates the contribution from buried layer interfaces. If so, this may be because no attempt was made to model reflections from thin ice crusts reported in the snowpit (2 thin crusts in 3 m depth). The extinction coefficient from the model is slightly lower than observed, perhaps because no attempt was made to simulate grain growth beyond 3 m depth, where the snow pit data ends.

Table 3.3 Comparison between the observed parameters and the predictions of the numerical model for plausible variations in roughness.

Parameter	Measured	Rough Interfaces RMS slope = 0.14	Smooth Interfaces RMS slope = 0.025
σ^o_{surf} (dB)	- 0.1	- 3	12
σ^o_{vol} (dB)	4.0	- 4	11
k_e (m^{-1})	0.24	0.19	0.19

The contribution of the diffuse intensity $\bar{I}_d(z,\theta,\phi)$ to σ^o_{vol} was calculated to be -20 dB, independent of the RMS slope of buried interfaces. This is less than 1% of the observed value, and less than 1% of the contribution from $\bar{I}_r(z,\theta,\phi)$ given in table 3.3, even for rough layers, so the model supports the conclusion that scattering by grains is relatively unimportant in generating backscatter at vertical incidence. Scattering from snow grains certainly does seem to comprise less than 10% of the total backscatter as suggested by Remy et al. (1995) based on Seasat scatterometer observations.

The sensitivity of k_e to layering was determined by replacing the stochastic density profile with the mean value of 400 kg m^{-3}. The extinction coefficient obtained differed by less than 10% from the value calculated with layering included, showing that k_e is mostly determined by the grain size; this agrees with the observations of earlier sections. When the mean density was increased from 400 kg m^{-3} to 500 kg m^{-3}, the extinction coefficient fell from 0.19 m^{-1} to 0.16 m^{-1}, suggesting that k_e is somewhat sensitive to the mean density profile - note that, because DMRT accounts for the correlation in position of neighbouring particles, this sensitivity has the opposite sign to that predicted by a model assuming independent scattering centres. As the density increases, the grains are forced closer together, interference effects become greater, and the scattering efficiency is reduced.

3.5 The impact of scattering upon elevation change measurements

So far, this chapter has clarified the role of each of the mechanisms pictured in figure 2.1. This will aid the analysis of the time varying changes in backscatter, shown in figure 1.1b, and the backscatter anisotropy, shown in figure 1.2b. This analysis aims to explain the elevation anomalies, shown in figure 1.1a and 1.2a and determine the likely errors from other changes in snow structure which may occur on longer timescales.

Time variant scattering

Figure 3.9 shows the difference between the total backscatter σ^o measured in cycles 87 and 97, almost exactly a year apart. Changes of up to 2 dB are observed. These changes are correlated over length scales of several hundred kilometres. Figure 3.10 shows deconvolutions $\tilde{r}$ from 78 S, 37 W (near Plateau Station) for cycles 87 and 97; the difference between the two deconvolutions is also shown. The change in backscatter is clearly associated with a change in the strength of the reflection from the air-snow interface. Scattering from beneath the surface is stable to within the errors expected in the deconvolutions. This is exactly what one would expect. The properties of the surface layer are altered by each snowfall, and there is evidence from snowpits that only snow within 10 - 15 cm of the surface undergoes rapid metamorphosis in-situ (Alley 1988).

Figure 3.8 shows that halving the RMS slope should cause an increase in σ^o_{surf} of roughly 5 dB. If backscatter were split equally between σ^o_{surf} and σ^o_{vol} before such a change, this would cause a 2dB increase in the total backscatter σ^o, similar to that observed. The same change in backscatter would be expected for an increase in the density of the surface snow from 200 $kg\ m^{-3}$ to 400 $kg\ m^{-3}$. In reality, the observed backscatter changes are probably caused by simultaneous changes in roughness and density, as the surface layer of snow is replaced, or weathered between snowfalls.

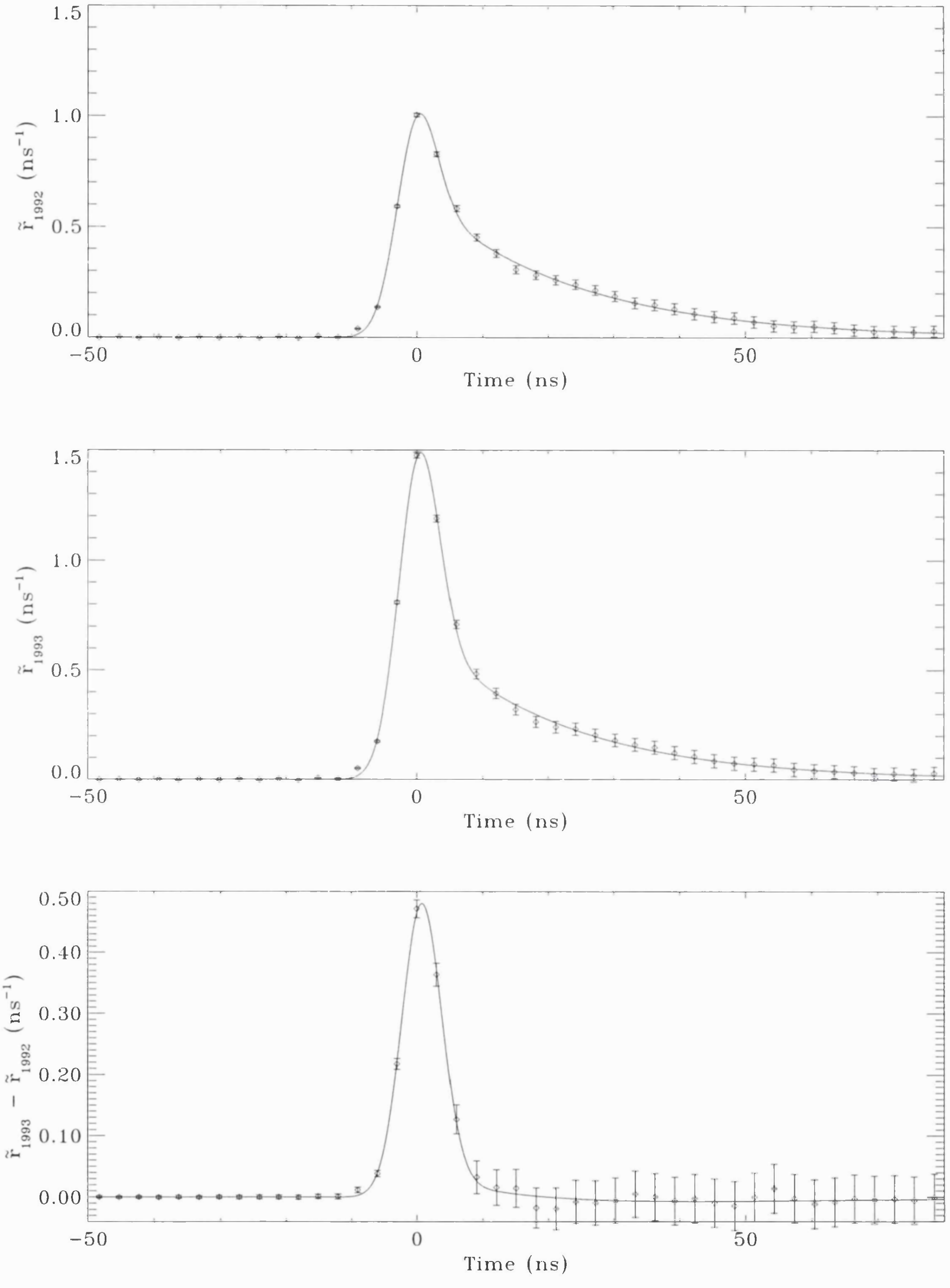

Figure 3.10 Deconvolutions from near Plateau Station, in September 1992 (top), September 1993 (middle), and their difference (bottom). The change in backscatter is clearly localised at the surface (times near zero). Note the Gaussian shape of the difference, indicating that topographic distortion of the echoes is minimal in this region.

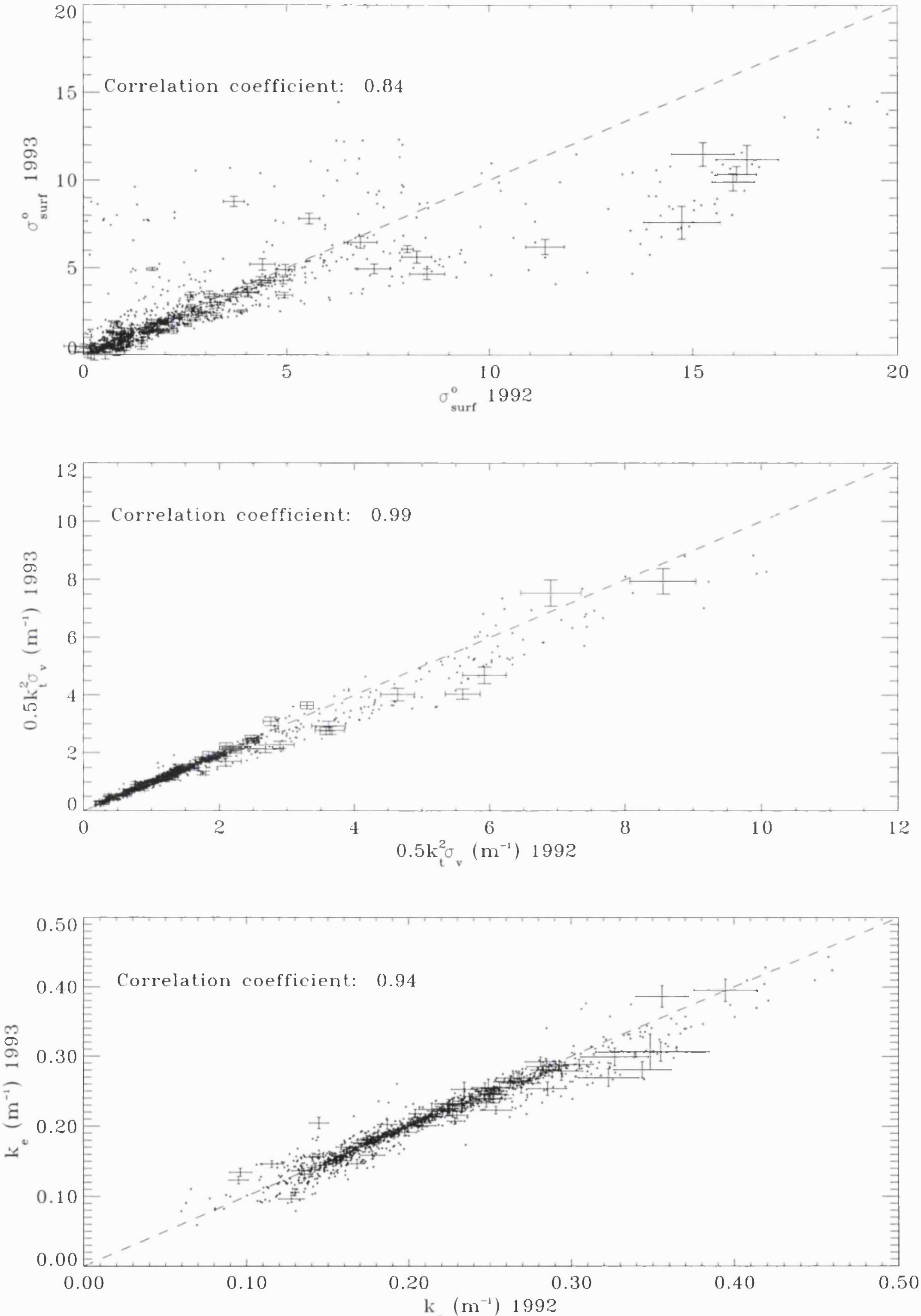

Figure 3.11 The decorrelation of σ^o_{surf} *(top),* $k_e\sigma^o_{vol}\left(=0.5k_t^2\sigma_v\right)$ *(middle), and* k_e *(bottom) between September 1992 and September 1993. The decorrelation of* σ^o_{surf} *is substantially greater than for the other two quantities. The 95% confidence intervals for errors caused by speckle noise and instrumental fluctuations are shown on a representative selection of points.*

Figure 3.11 shows the change in parameters for all 1195 regions. The pattern seen in figure 3.10 is borne out across the ice sheet: the decorrelation of $\sigma^{\text{o}}_{\text{surf}}$ over the year is much more pronounced than the decorrelation of k_e, or of the product $0.5k_t^2\sigma_v$, which is obtained by multiplying $\sigma^{\text{o}}_{\text{vol}}$ and k_e (this was done to eliminate the dependence of $\sigma^{\text{o}}_{\text{vol}}$ upon k_e through equation 2.2.13, so giving three independent quantities).

Because the reflection at the air-snow interface is weak (see figure 3.7a), the transmission coefficient is high and $k_t \approx 1$. This means that most of the variation in the product $0.5k_t^2\sigma_v$ reflects changes in the backscatter per unit volume σ_v. Since both σ_v and k_e relate to buried snow, it does seem physically reasonable that they should be stable on timescales of a year or so. Nevertheless, the error bars on figure 3.11 show that, in some regions, the scatter in these quantities is larger than the 95% confidence intervals predicted from speckle noise and IF fluctuations alone. However, most of these locations are in West Antarctica, where the surface is very undulating. Bearing in mind the findings of section 2.5, the most likely reason for this scatter is the distortion of the echoes caused by topographic undulations. Table 2.1 shows that the errors in $\sigma^{\text{o}}_{\text{vol}}$ and k_e will change when $\sigma^{\text{o}}_{\text{surf}}$ changes, even though the topography remains unchanged, and this would mimic temporal changes in $\sigma^{\text{o}}_{\text{vol}}$ and k_e. These data therefore provide no evidence for a significant change in the structure of the subsurface snow between 1992 and 1993.

It is worth asking what the temporal changes in $\sigma^{\text{o}}_{\text{surf}}$ can reveal about the topographic distortion of the echoes. Assuming that $\sigma^{\text{o}}_{\text{surf}}$ changes, while $\sigma^{\text{o}}_{\text{vol}}$ and k_e remain stable, then the difference between deconvolutions separated in time will reveal the shape of the function J. This can be seen by altering $\sigma^{\text{o}}_{\text{surf}}$ in equation (2.2.12) and noting the effect upon equation (2.2.42). It is clear from figure 3.10 that, on the extremely flat plateau of East Antarctica, the assumption that J is Gaussian is justified.

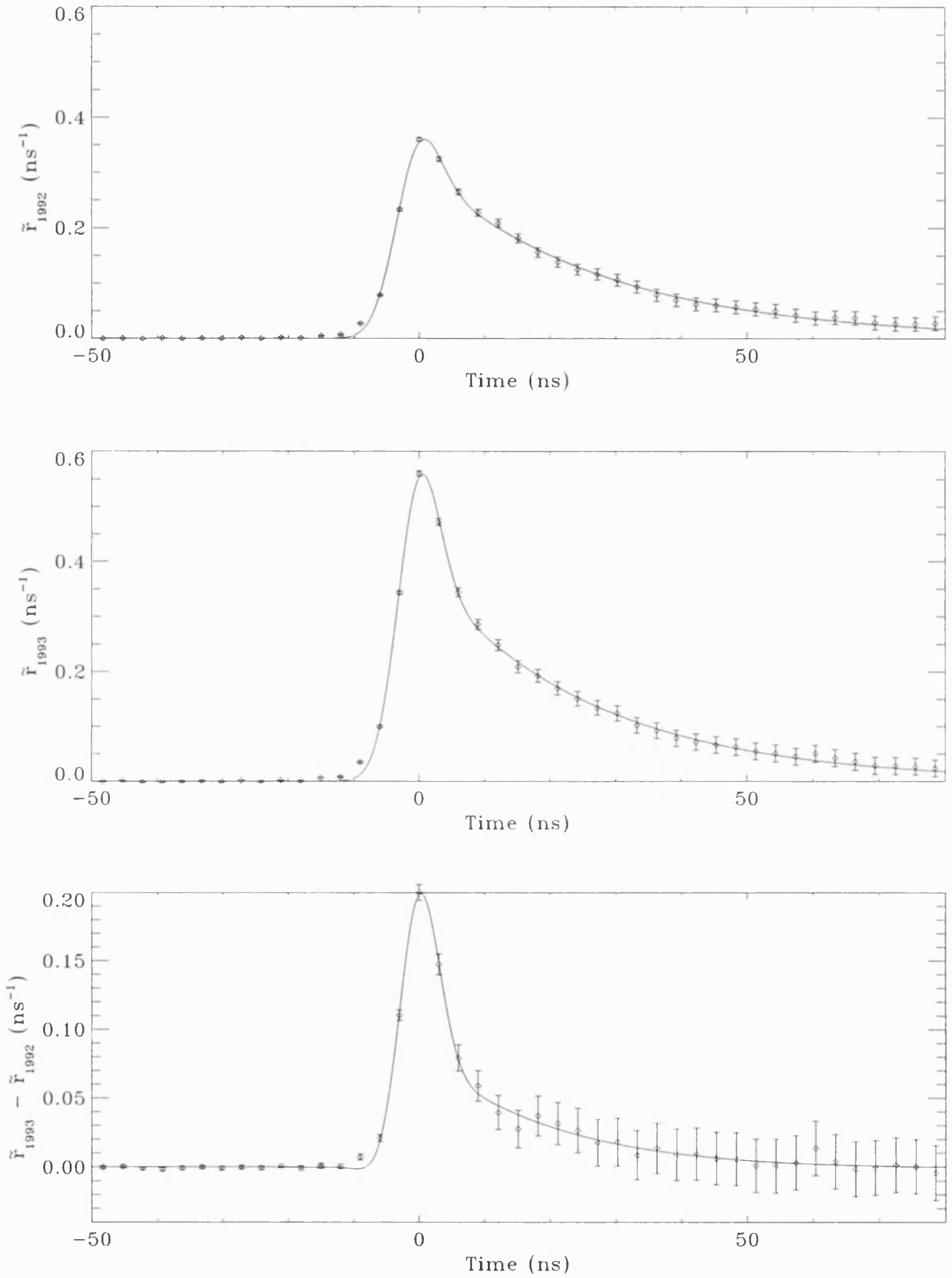

Figure 3.12 Deconvolutions from West Antarctica in September 1992 (top), September 1993 (middle), and their difference (bottom). In contrast to figure 2.25, the change in backscatter extends to large times, so either the scattering from beneath the surface has changed, or the echoes in this region are distorted by undulating topography. The latter seems more likely given the extremely undulating topography of West Antarctica.

Figure 3.12 however, shows the temporal change from (80 S, 95 W) in West Antarctica, where topographic undulations are more pronounced. Here, J is clearly not Gaussian, but resembles the simulations from undulating topography shown in figure 2.11. In the absence of detailed information about the topography on the kilometre scale, the time varying changes provide a useful means for assessing where the echoes are heavily distorted by topography. Inspection of the deconvolutions reveals that all of West Antarctica is affected by this distortion, while the region of East Antarctica considered here is unaffected. Echoes from the margins of East Antarctica, which were not investigated in this study, are likely to be distorted, since the margins exhibit more pronounced undulations than the plateau.

It seems very likely that the failure of the model defined by equation (2.4.24) to fit the deconvolutions over much of West Antarctica is due to the distortion of the altimeter echoes as a result of the more undulating terrain there. The simulations of section 2.5 suggest that in West Antarctica the retrieved value of $\sigma^{\circ}_{\mathrm{vol}}$ may be several dB too high, $\sigma^{\circ}_{\mathrm{surf}}$ several dB too low, and k_e underestimated by more than 20%. The retracking algorithm developed by Davis and Moore (1993) uses the same assumptions as were used to derive equation (2.4.24), so this algorithm will also be subject to errors in West Antarctica and any regions of East Antarctica or Greenland with comparable undulations.

The anisotropy in backscatter

The ratio between ascending and descending measurements of total backscatter σ° is shown in figure 3.13; the data were taken from cycle 87. Large discrepancies are seen in Wilkes Land, Princess Elizabeth Land and the Mizuho Plateau region. In Princess Elizabeth Land the ratio is greater than 2 dB - larger than anywhere else on the ice sheet.

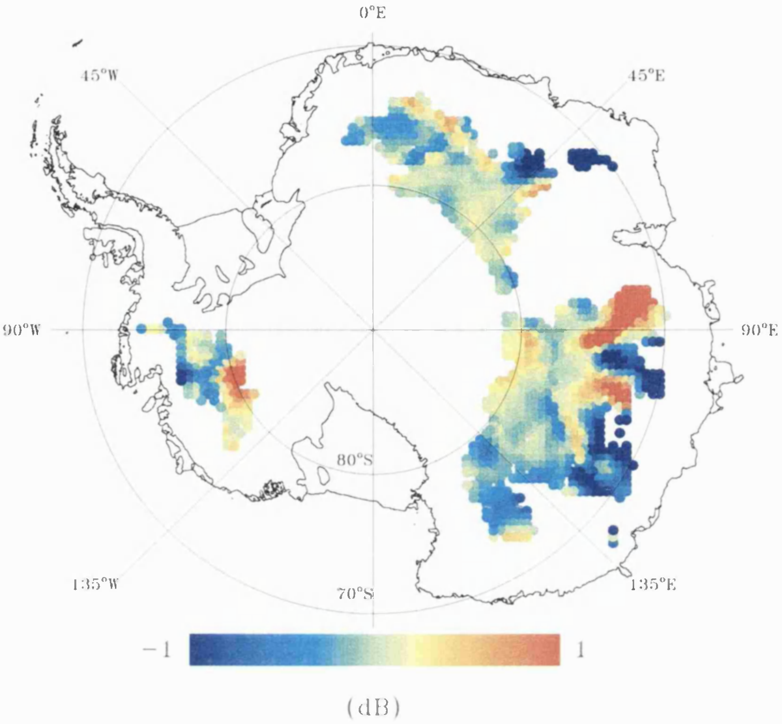

Figure 3.13 The discrepancy in backscatter between ascending tracks and descending tracks. Large discrepancies are seen in regions of strong katabatic winds, in particular Princess Elizabeth Land, Wilkes Land and Mizuho Plateau.

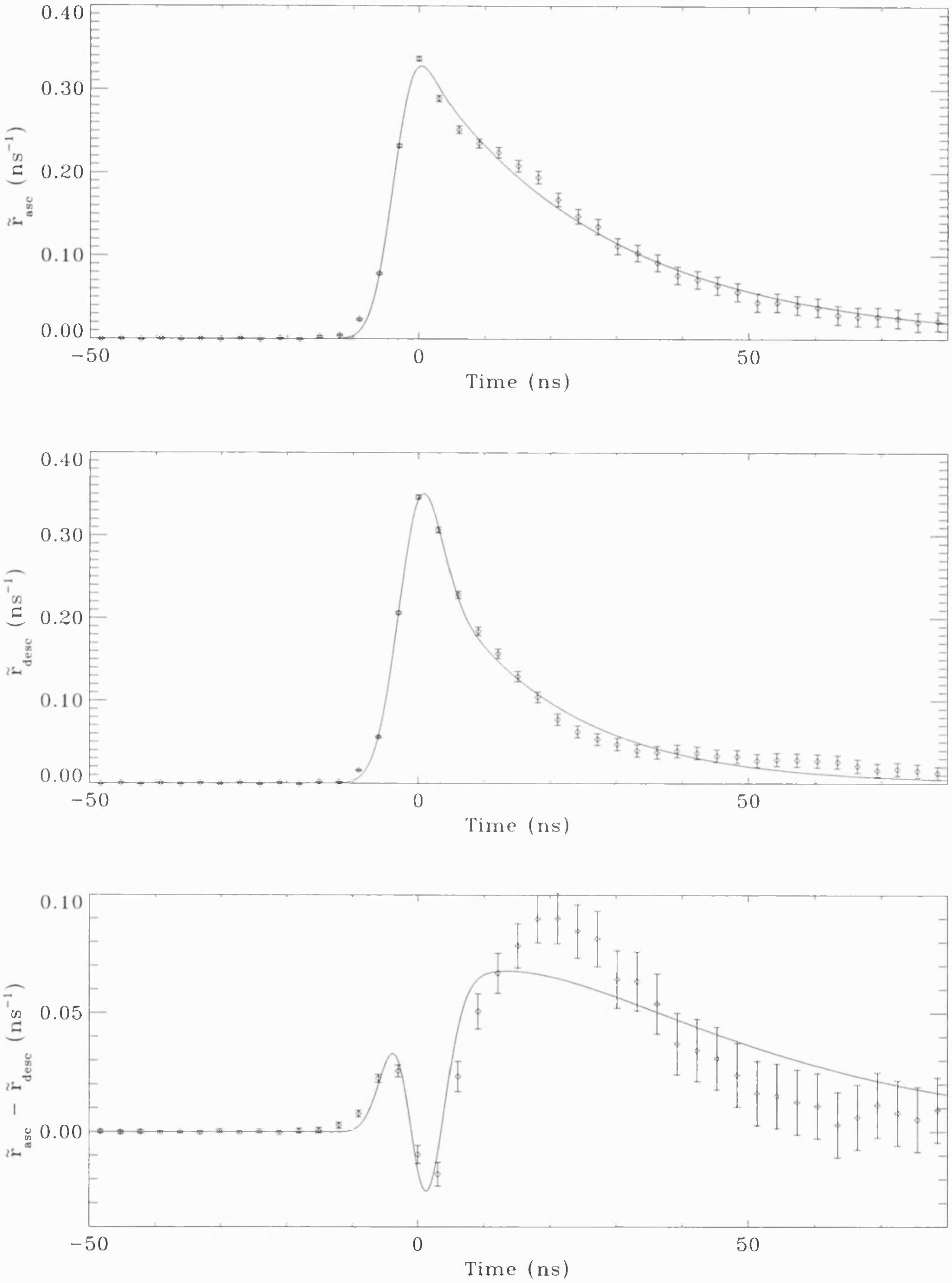

Figure 3.14 The deconvolutions from ascending tracks (top), descending tracks (middle), and their difference (bottom) from Princess Elizabeth Land. The difference is associated with scattering from beneath the surface. The failure of the model to fit the data within the expected errors is caused by the non-exponential decay.

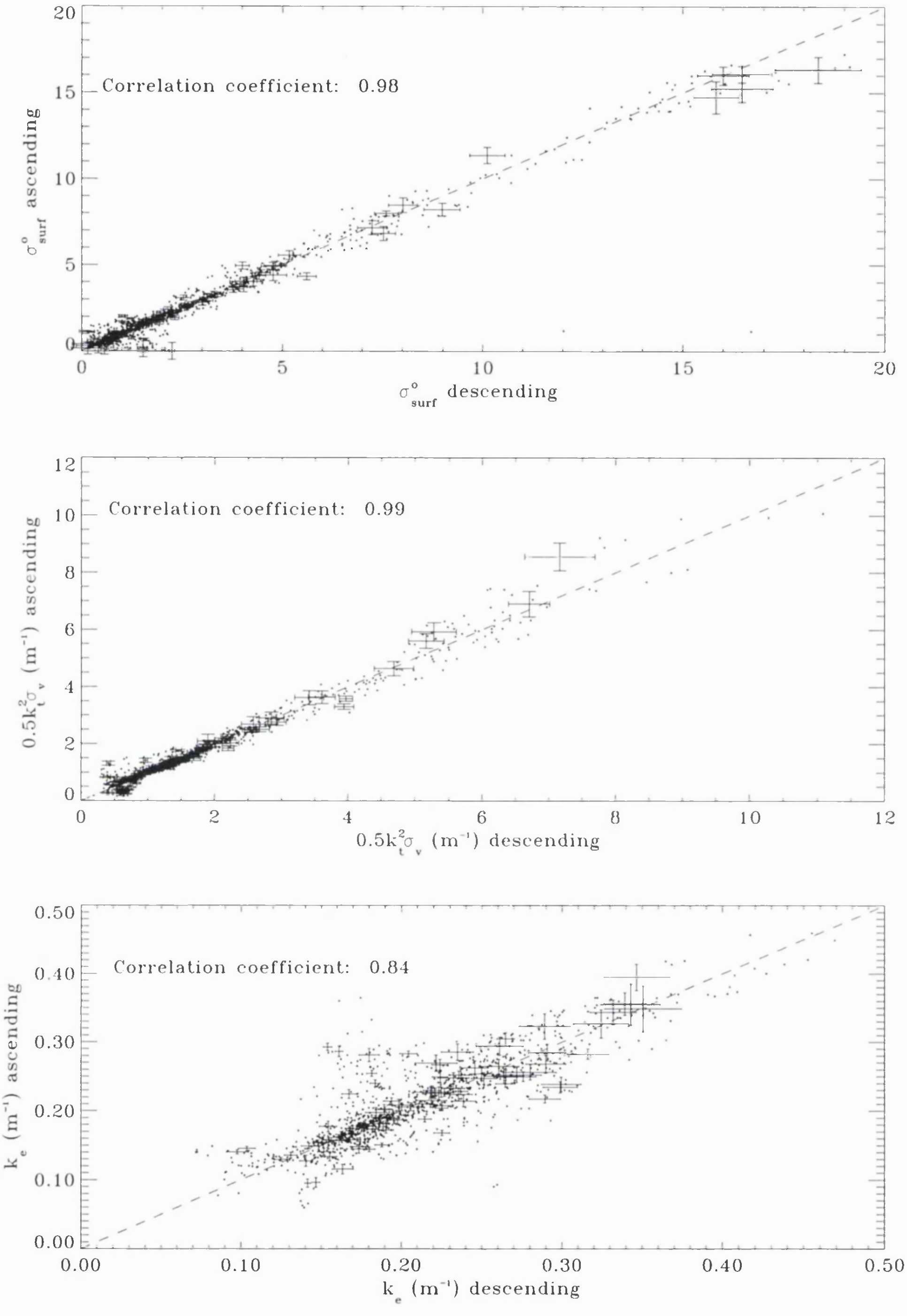

Figure 3.15 The decorrelation of $\sigma^{o}_{\mathrm{surf}}$*(top),* $k_e\sigma^{o}_{\mathrm{vol}}\left(=0.5k_t^2\sigma_v\right)$ *(middle), and* k_e*(bottom) between ascending and descending tracks. The decorrelation of* k_e *is substantially greater than for the other two quantities. The 95% confidence intervals for errors caused by speckle noise and instrumental fluctuations are shown on a representative selection of points.*

Figure 3.14 shows deconvolutions $\tilde{r}$ from ascending and descending tracks separately: the difference between the two deconvolutions is also shown. In contrast to the temporal change shown in figure 3.10, the anisotropy is seen most strongly at large delay times. Inspection of the time varying changes at this site reveals that the topographic distortion is minimal, so the anisotropy must be associated with the subsurface snow. The small peak near zero time delay is an artefact of a slight misalignment of the echoes by the OCOG algorithm - shifting the deconvolutions slightly before differencing removed this peak, but otherwise left the main features of the curve unchanged.

Figure 3.15 shows the decorrelation between ascending and descending parameters for all 1195 locations for which $\sigma^{\text{o}}_{\text{surf}}$, $\sigma^{\text{o}}_{\text{vol}}$ and k_e were retrieved. Most of the decorrelation is seen in k_e: neither $\sigma^{\text{o}}_{\text{surf}}$, nor the product $0.5k_t^2\sigma_v$ is anisotropic with respect to the direction of satellite travel. The mechanism for the anisotropy in k_e is difficult to establish without more detailed observations of the firn structure than are available at present. However, the earlier findings of this chapter provide some grounds for speculation. In sections 3.2, 3.3 and 3.4, it was established that the backscatter is dominated by reflections, while the extinction is dominated by scattering from snow grains. The fact that the backscatter anisotropy is isolated in k_e, and does not affect $\sigma^{\text{o}}_{\text{surf}}$ or $0.5k_t^2\sigma_v$, provides strong evidence that the effect is controlled by scattering from snow grains.

Because ERS-1 transmits at linear polarisation, with the orientation of the electric field fixed with respect to the satellite, any azimuthal anisotropy in the grain structure, such as elongated snow grains oriented in a preferred direction, could produce different extinction on ascending and descending tracks. The largest extinction would be expected when the exciting electric field was parallel to the preferred orientation of larger grain dimensions.

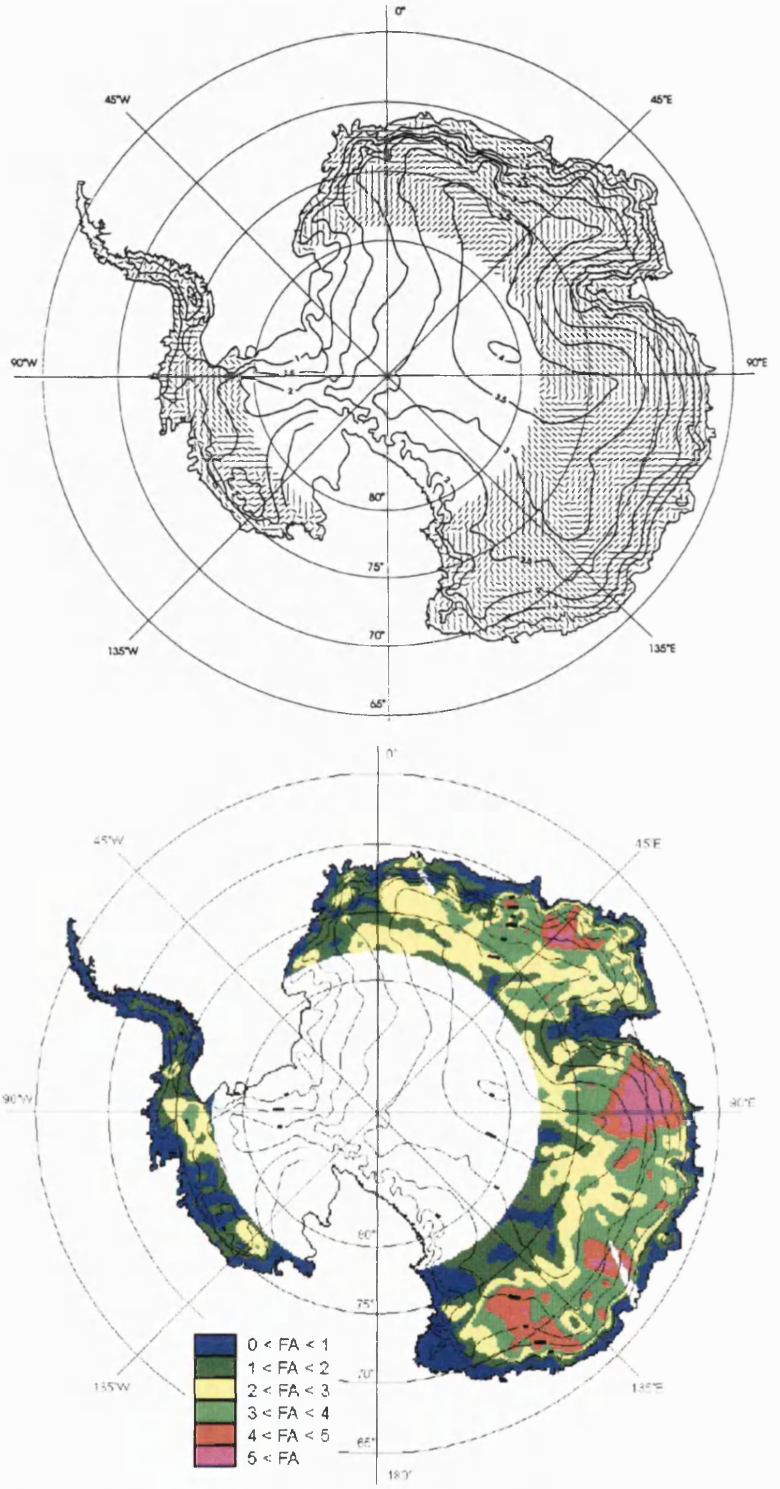

Figure 3.16 The direction and magnitude of the azimuthal anisotropy in backscatter measured with the ERS-1 scatterometer (from Rott and Rack 1995 and Rack 1995). The figures show the amplitude and direction of elongated surface relief, which indicates the strength and direction of the wind. Note the correlation with figure 3.13 the largest amplitude is seen in Princess Elizabeth Land, Wilkes Land and Mizuho Plateau regions. The changes in sign in the backscatter anisotropy seem to mirror changes in wind direction.

The locations of greatest backscatter anisotropy are coincident with regions of strong katabatic winds. Comparison of figure 1.2 and figure 3.13 with ERS-1 scatterometer data shown in figure 3.16 (Rott and Rack 1995; Rack 1995), provides further evidence that the backscatter anisotropy is associated with the wind.

Laboratory experiments (Keller and Hallet 1982; Colbeck 1983) and snowpack observations (Sturm and Johnson 1991) reveal that crystal growth is sensitive to the direction of vapour transport within the snowpack, so it seems plausible that persistent winds from a particular direction could impart anisotropy into the granular structure of the snow by influencing grain growth. Another possibility is that the wind mechanically aligns non-spherical crystals in fresh snow or surface hoar before they become sintered in place. Alternatively, the wind may cause the anisotropy in grain structure indirectly, through its influence upon the surface microrelief: in windy regions, sastrugi are oriented parallel to the prevailing wind, and seem to be preferential sites for the development of large depth hoar crystals (Alley et al. 1990). A horizontal component to the vapour transport would be expected within sastrugi because of the difference in temperature between the sunlit and shaded sides, and this may enhance crystal growth in a preferred horizontal direction. More detailed field observations are needed to reveal which of these mechanisms (or some other) is responsible for the backscatter anisotropy.

If the anisotropy in k_e is caused by an azimuthal anisotropy in grain structure due to the wind, it should decay with depth as the grains become buried and adopt more spherical equilibrium forms. Some evidence of this is provided by figure 3.14. Neither the ascending nor descending backscatter decays exponentially with depth: the ascending curve has a slight shoulder at shallow depths, while the descending curve decays rapidly to begin with before levelling out.

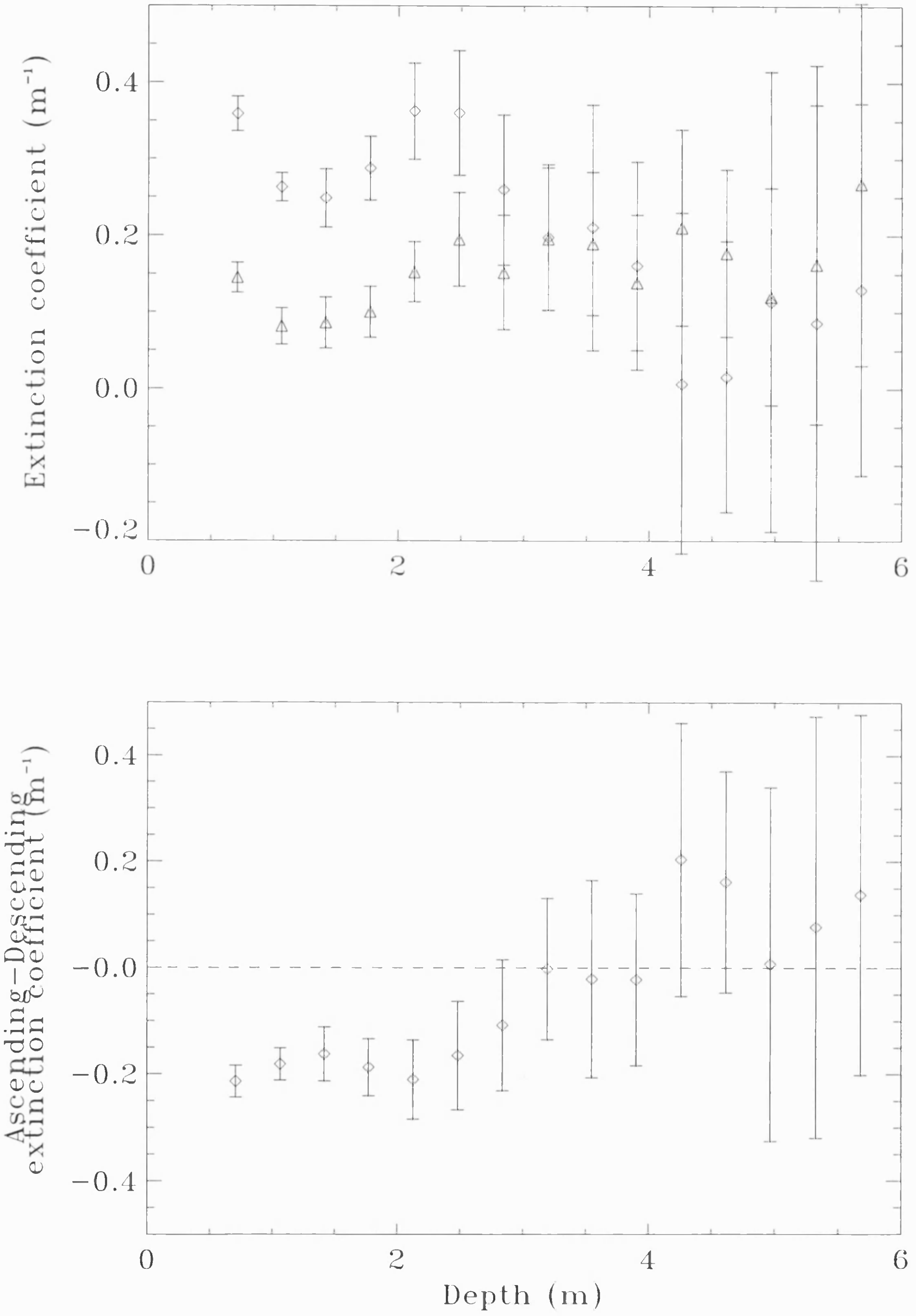

Figure 3.17 The difference between extinction coefficients on ascending and descending tracks as a function of depth. The anisotropy in extinction coefficient decreases with depth. Significant differences are only seen in the upper 3 m of snow.

Figure 3.17a shows the variation of extinction with depth, obtained by differentiating the logarithm of the deconvolutions $\tilde{r}(t)$ shown in figure 3.14. The difference between ascending and descending extinction is also plotted as a function of depth in figure 3.17b. The anisotropy in the extinction coefficient decreases with depth - below 3m no significant difference is seen. This explains the failure of the model defined by equation (2.4.24) to fit the data in this region (recall figure 2.15) - the model does not allow for any depth dependence in the extinction coefficient.

It is worth pointing out that neither the elevation change estimate Δ_h nor the backscatter change Σ_h will be affected by the anisotropy in k_e. This is because equations 1.1 and 1.2 weight ascending and descending tracks equally on earlier and later cycles. If, on the other hand, the algorithm of Zwally (1983) were used to obtain the height change, the elevation changes would be corrupted whenever the proportion of ascending and descending measurements changed over time. Since most satellite systems suffer periods of inoperation, and radar altimeters in particular often lose lock on the surface over ice sheets, there is no reason to suppose the proportion of ascending and descending measurements will not change.

From now on it is assumed that equation 1.1 is used, so that only temporal changes in backscatter will cause errors in the geodetic method. Next, the likely magnitude of these errors will be considered.

The sensitivity of the elevation change measurement to changes in scattering

The elevation error ε caused by scattering can be considered as a function of three variables, σ^{o}_{surf}, σ_v and k_e (it is assumed that the transmission coefficient k_t is always close to 1, so hardly affects ε). The change $d\varepsilon$ between measurements can be written

$$d\varepsilon \approx \frac{\partial \varepsilon}{\partial \sigma^{o}_{\text{surf}}} d\sigma^{o}_{\text{surf}} + \frac{\partial \varepsilon}{\partial \sigma_v} d\sigma_v + \frac{\partial \varepsilon}{\partial k_e} dk_e \tag{3.5.1}$$

where $d\sigma^{o}_{\text{surf}}$, $d\sigma_v$ and dk_e are the changes in σ^{o}_{surf}, σ_v and k_e respectively.

The partial derivatives in equation (3.5.1) determine the sensitivity of the elevation change estimate to small changes in the scattering parameters. Their magnitude was estimated by numerical simulation. Ice mode echoes were simulated by evaluating equation (2.2.20) analytically, for the case $\Delta = 0$, using Gaussian approximations for q, D_{short} and using Appendix A, equations (A.4) - (A.7) for $I(t)$. Changes in the scattering conditions were simulated by altering the values of σ^{o}_{surf}, σ_v and k_e used in equations (2.2.12) and (2.2.13) which define the scattering distribution s. These simulated echoes were processed in the same way as the real data to reveal the effect of the scattering changes upon the elevation measurement.

Two alternative ways of processing the echoes were investigated - the cross-correlation method, and the OCOG retracking method (Bamber 1994) - a variety of other retracking algorithms are used by different researchers to calculate the elevation change from the altimeter echoes, and each will suffer from different errors. The cross-correlation method, which was used to produce figures 1.1a and 1.2a, obtains the crossover differences by cross-correlating the echoes measured on ascending and descending passes (it is assumed that any change in elevation of the ice sheet causes a translation of the echoes in time delay, once any difference between the satellite altitude on ascending and descending tracks has been accounted for). The OCOG retracking algorithm estimates the elevation of the surface by locating the leading edge of the echo. In these simulations this was assumed to lie at the point where the echo power first exceeds 50% of the eventual amplitude (Bamber 1994). Although these simulations are specific to the algorithms tested here, a similar approach could be used to estimate the sensitivity of any processing scheme to changes in σ^{o}_{surf}, σ_v and k_e.

Figure 3.18 shows the simulated ice mode echo for $\sigma^{o}_{\text{surf}}=7$ dB $\sigma^{o}_{\text{vol}}=10$ dB and $k_e=0.2$, taken as a typical reference state, and the change in shape for a +2 dB (+ 3.0 linear) change in σ^{o}_{surf}, with k_e and σ_v fixed. Even though both echoes were calculated assuming the same range to the surface, the highest correlation between them is achieved with a relative shift of 2.0 ns. This shift corresponds to a 30 cm height error. Thus, for the cross-correlation method, the partial derivative of ε with respect to σ^{o}_{surf} is of order 0.1 m. Because the echoes are normalised before they are cross correlated, the absolute power level is irrelevant, so the same simulation can equally be considered a -2dB change in σ_v. This gives a value of about -0.2 m^2 for the partial derivative of ε with respect to σ_v. Figure 3.19 shows the change in shape from the same reference state when k_e changes from 0.2 to 0.15 while σ^{o}_{surf} and σ_v remain constant. This gives a 57 cm height error, and a value of about 11.4 m^2 for the partial derivative of ε with respect to k_e.

For the 50% OCOG threshold retracking algorithm, the partial derivatives were calculated from the same echoes to be 0.08 m, -0.17 m^2 and 5.8 m^2 with respect to σ^{o}_{surf}, σ_v and k_e respectively. These are of the same order of magnitude as for the cross-correlation method, although the OCOG method is about half as sensitive to changes in k_e.

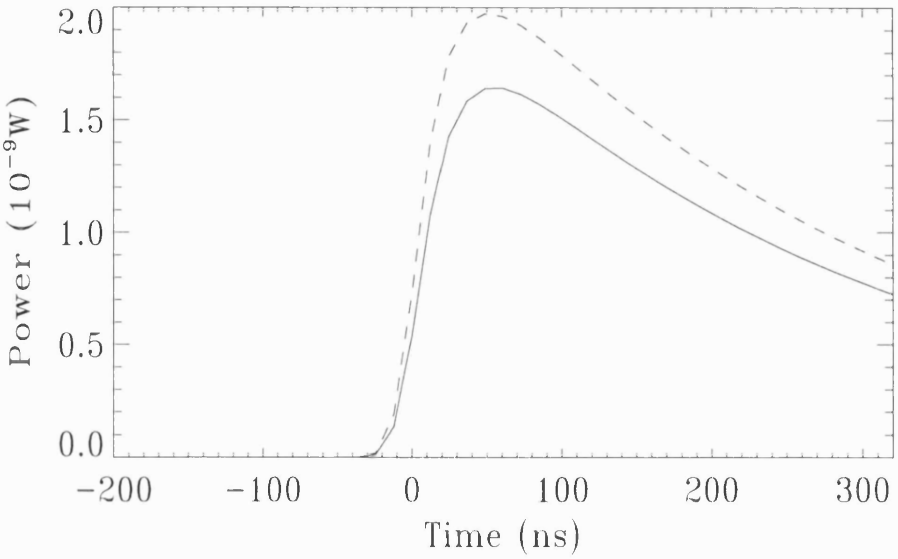

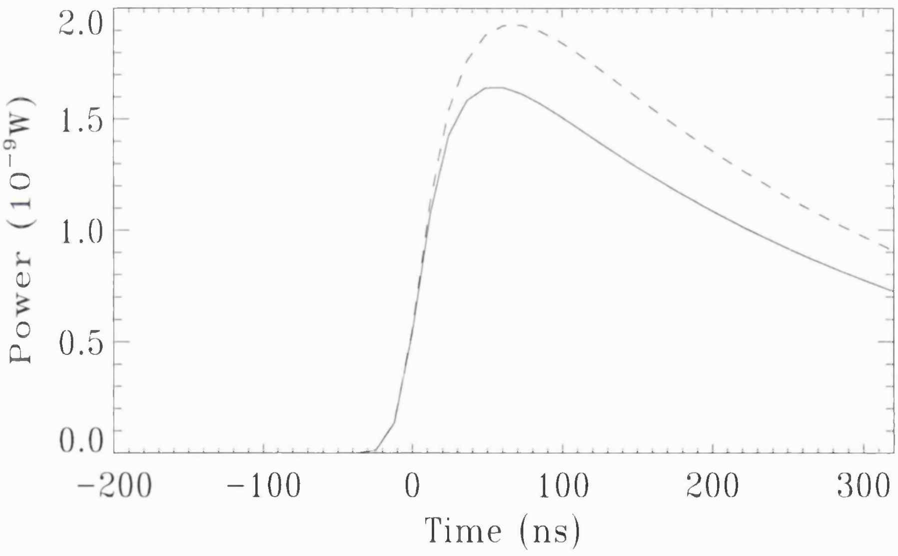

Figure 3.18 (top) Simulated ice mode echoes for σ^o_{surf}*=7 dB,* σ^o_{vol}*=10 dB and* k_e*=0.2 (solid line) and a 2 dB increase in* σ^o_{surf} *(dashed line).*

Figure 3.19 (bottom) Simulated ice mode echoes for σ^o_{surf} *=7 dB,* σ^o_{vol}*=10 dB and* k_e*=0.2 (solid line) and a 25% decrease in* k_e *(dashed line).* σ^o_{vol}*was recalculated using equation (2.2.13), assuming* k_t *and* σ_v *remain constant.*

Similar simulations about other reference states suggest that the values for the partial derivatives calculated above are fairly representative. In support of this claim, it should be noted that the changes in σ^{o}_{surf} and k_e simulated are typical of those observed, and the elevation errors agree in sign, and magnitude, with the elevation anomalies in figures 1.1a and 1.2a.

More accurate estimates of the partial derivative of ε with respect to σ^{o}_{surf} can be obtained empirically at any particular site by calculating Δ_h and Σ_h, using equations (1.1) and (1.2), and using data such that the time interval T is a few months or shorter. For such a short time interval, the measured height change Δ_h will be dominated by errors caused by changes in σ^{o}_{surf}, rather than the true elevation change. Similarly, it is very unlikely that the structure of the deeper snow would have changed over such a short time interval, so the backscatter change Σ_h can be ascribed to changes in σ^{o}_{surf} with some confidence. Thus, an estimate of the partial derivative of ε with respect to σ^{o}_{surf} is provided by the ratio $\mu = \Delta_h(\text{for short } T)/\Sigma_h(\text{for short } T)$.

The estimated partial derivative μ is useful because it allows measurements of Δ_h over longer time intervals to be corrected for changes in σ^{o}_{surf}, giving an improved estimate of the true elevation change (Ridout, manuscript in preparation). The corrected estimate Δ_h' is

$$\Delta_h' = \Delta_h - \mu\Sigma_h \tag{3.5.2}$$

Now the impact of various scattering changes upon Δ_h' can be studied. Using $\sigma^{o} = \sigma^{o}_{\text{surf}} + \sigma^{o}_{\text{vol}}$ and equation (2.2.13) gives

$$d\sigma^{o} \approx d\sigma^{o}_{\text{surf}} + \frac{k_t^2}{2k_e} d\sigma_v - \frac{k_t^2 \sigma_v}{2k_e^2} dk_e \tag{3.5.3}$$

Using equation (3.5.1) for the error in Δ_h and equation (3.5.3) to predict the effect of changes in $\sigma^{\circ}_{\mathrm{surf}}$, σ_v and k_e upon Σ_h, the error in Δ'_h caused by scattering changes can be written

$$d\varepsilon' = \left(\frac{\partial \varepsilon}{\partial \sigma^{\circ}_{\mathrm{surf}}} - \mu \right) d\sigma^{\circ}_{\mathrm{surf}} + \left(\frac{\partial \varepsilon}{\partial \sigma_v} - \frac{\mu k_t^2}{2k_e} \right) d\sigma_v + \left(\frac{\partial \varepsilon}{\partial k_e} + \frac{\mu k_t^2 \sigma_v}{2k_e^2} \right) dk_e \tag{3.5.4}$$

If μ is accurate, the first bracket will be zero and Δ'_h will be insensitive to changes in $\sigma^{\circ}_{\mathrm{surf}}$ as desired. The second and third brackets can be calculated using the partial derivatives found above; for the cross correlation method, the values are -0.45 m^2 and 16.4 m^2 respectively; for the OCOG method they are -0.4 m^2 and 15.4 m^2 respectively.

It should be stressed that, unlike the NASA S/V retracking algorithm (Davis and Moore 1993), which also tries to limit the sensitivity of the elevation measurement to scattering changes, the correction procedure defined by equation (3.5.2) does not rely upon the assumption (2.2.16), so it may be used even in undulating regions. The two approaches are not mutually exclusive however, and a similar correction could be applied to elevation changes measured using the NASA S/V algorithm; indeed there may be advantages to such an approach, because, even in the presence of undulations, the partial derivatives of ε with respect to $\sigma^{\circ}_{\mathrm{surf}}$, σ_v and k_e are likely to be smaller for the NASA S/V algorithm than those considered here for the OCOG and cross-correlation methods.

The sensitivity of snowpack structure and scattering to plausible changes in climate

Even though, Δ_h' is insensitive to changes in σ^o_{surf}, the structure of the deeper snow may change over measurement intervals lasting many years, causing changes in σ_v and k_e. In fact, comparing equations (3.5.1) and equation (3.5.4) it is obvious that the corrected estimate Δ_h' will be more sensitive to such changes than the uncorrected estimate Δ_h, so there may be a price to pay for removing the effects of changes in σ^o_{surf}. The likely magnitude of the errors $d\varepsilon$ and $d\varepsilon'$ is considered below for plausible changes in temperature, accumulation rate, snow density, and roughness. The results are shown in table 3.4, where they are compared with the errors caused by the observed changes in σ^o_{surf} and the anisotropy in k_e.

Gow (1969) showed that the grain-size profile is sensitive to the accumulation rate and the mean annual temperature. Change in temperature and accumulation rate could therefore affect k_e and cause errors in the elevation change measurement. The following empirical equation (Zwally 1977; Davis 1995) predicts the increase in grain radius r_g as a function of depth z

$$r_g^3 = r_0^3 + \gamma z \tag{3.5.5}$$

where the grain growth coefficient γ is determined as follows

$$\gamma = \frac{k_0 \rho}{A} exp\left[-\frac{E}{R\overline{T}}\right] \tag{3.5.6}$$

In equations (3.5.4) and (3.5.5) r_0 is the radius of grains at the surface; $k_0 = 10^7 \text{mm}^3 \text{ yr}^{-1}$ is a constant derived from the data given by Zwally (1977); $\rho = 400 \text{ kg m}^{-3}$ is a typical snow density; A is accumulation rate; $E = 43.2 \text{ kJ mol}^{-1}$ is the activation energy for grain growth; $R = 8.314 \text{ J mol}^{-1} \text{K}^{-1}$ is the gas constant; and

$\bar{T}$ is the mean annual surface temperature. Because r_0 is small, and reasonably constant between sites, the average grain size of the snow contributing to the altimeter echo is largely determined by the grain growth coefficient γ.

If the temperature or accumulation rate changes, then the grain-diameter profile will tend towards a new equilibrium satisfying equations (3.5.5) and (3.5.6). To find the sensitivity of k_e to changes in the grain-size profile, γ was calculated for each of the snowpit locations along the SPQMLT3 route using equation (3.5.6) and the measured values of A and $\bar{T}$. Figure 3.20 shows these values plotted against values of k_e retrieved from the altimeter at the same sites. The data suggest a linear relationship of the form

$$\gamma = b(k_e - a) \tag{3.5.7}$$

with a=0.069 m^{-1} and b=0.043 mm. The functional form of equation (3.5.7) was justified theoretically using the scattering model (see figure 3.21). Appendix B describes this calculation, and an investigation into the feasibility of using equation (3.5.7) to derive estimates of accumulation rate. Here though, the focus is upon mass balance measurements, so equation (3.5.7) will only be used to estimate the sensitivity of k_e to changes in temperature and accumulation rate, and the subsequent effect upon the elevation measurements.

Equations (3.5.6) and (3.5.7) show that, for an initial k_e value of 0.2 m^{-1}, a 1K increase in temperature would cause an increase of about 0.013 m^{-1} in extinction coefficient, assuming the accumulation rate remained unchanged. This sensitivity was calculated for a temperature of -40°C, but the effect changes by less than 50% for temperatures from -70°C to 0°C, so it can be considered typical for all ice sheet conditions. The resulting elevation errors in Δ_h and Δ'_h for the cross correlation and OCOG methods, can be calculated using equations (3.5.1) and (3.5.4), and are shown in table 3.4.

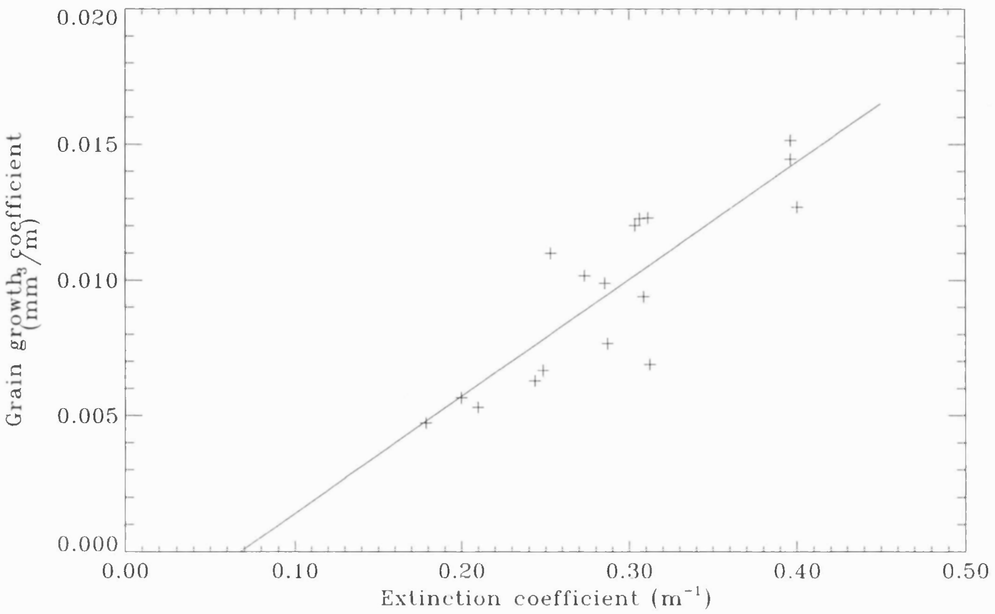

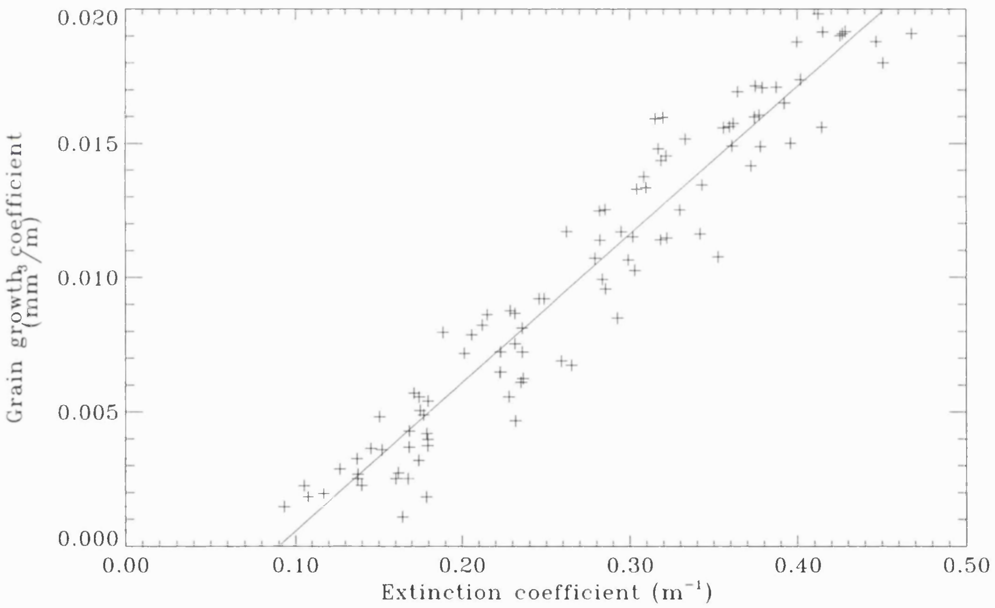

Figure 3.20 (top). The grain growth coefficient γ, calculated using equation (2.10.6) for points along the SPQMLT3 traverse, compared with the measured extinction coefficient from ERS-1. The data suggest the linear relationship of equation (2.10.7). In appendix 2B, this relationship is justified theoretically and its potential for deriving estimates of accumulation rate is assessed.

Figure 3.21 (bottom).The results of the Monte-Carlo simulation used to justify equation (2.10.7) - the model predicts the linear relationship, the intercept at $\gamma=0$ and the scatter caused by density variations fairly accurately, but the gradient cannot be constrained without accurate measurements of the grain size distribution.

Equations (3.5.4), (3.5.6) and (3.5.7) predict that a change in k_e of -0.013 m^{-1} would accompany a 10% increase in accumulation rate, assuming the temperature remained unchanged. If the accumulation rate increased because layers of the same thickness were deposited at shorter intervals, the errors for a 10% increase in accumulation would be comparable to those for a 1K temperature increase, but opposite in sign. If, on the other hand, the higher accumulation rate gave rise to thicker layers, σ_v would decrease too, because there would be less reflecting layer interfaces per unit volume. This would cause smaller errors than those quoted in table 3.4.

The effect of a density increase from 400 $\mathrm{kg\ m}^{-3}$ to 440 $\mathrm{kg\ m}^{-3}$ was found using the scattering model. For this density change $\sigma^{\circ}_{\mathrm{surf}}$ increased by 20%, σ_v decreased by 7% and k_e decreased by 3%. Snow density is roughly proportional to windspeed so these changes might accompany a 10% increase in windspeed (see extract from Kotlyakov 1961 in Mellor 1964). However, a change in wind speed would probably increase the roughness of the surface as well. A 10% increase in the RMS slope of the air-snow interface would only change $\sigma^{\circ}_{\mathrm{surf}}$, so would not affect Δ'_h. If this change in surface roughness persisted though, the RMS slope of buried layer interfaces would change too. Table 3.4 shows the effects of density and roughness changes separately.

Table 3.4 The errors in the elevation changes calculated using the cross-correlation and OCOG methods, with and without correction for changes in the surface reflection. The perturbations are assumed to persist for long enough that the upper 5 m or so of the snowpack equilibrates to the new conditions (about twenty years in Antarctica and about five in Greenland).

	Cross correlation		OCOG 50%	
	Uncorrected $d\varepsilon$(cm)	Corrected $d\varepsilon'$ (cm)	Uncorrected $d\varepsilon$(cm)	Corrected $d\varepsilon'$ (cm)
Observed changes in σ^{o}_{surf}	30	Cancels	25	Cancels
Observed anisotropy in k_e	Cancels	Cancels	Cancels	Cancels
Temperature +1K	15	21	8	13
Accumulation rate +10%	-15	-21	-8	-13
Density +10%	3	-4	5	-1
RMS slope +10%	5	31	4	25
Total (absolute values)	38	77	25	52

The OCOG method generally performs better than the cross-correlation method. The price of using the corrected estimate Δ'_h is that it is more sensitive to changes in the subsurface structure of the snow. However, these changes will occur more slowly than changes in σ^{o}_{surf} so the effect upon estimates of the rate of change of elevation will be less.

Most of the backscatter comes from the upper 5 m of snow, which, in Antarctica, represents about twenty years accumulation. This seems a likely timescale for elevation changes in table 3.4 to occur, so errors of the order 3 $\mathrm{cm\,yr^{-1}}$ might be expected using the corrected OCOG method. In Greenland, where the accumulation rate is about four time higher, five years seems a more appropriate timescale. This would translate into errors in the elevation change measurement of order 10 $\mathrm{cm\,yr^{-1}}$. In fact, the errors are likely to be smaller than this, because the meteorological forcing is unlikely to occur as an abrupt change, coincident with the start of the measurement interval, and persisting throughout.

3.6 Chapter summary

The investigations described in this chapter clarified the mechanisms responsible for backscatter from the Antarctic plateau. In most regions reflections from internal layer interfaces are responsible for most of the backscatter. Reflection from the air snow interface usually account for less than half the backscatter, although it may contribute up to 60% in regions prone to surface crusts. Backscatter from snow grains contributes only about 1% to the total: however, scattering from snow grains is the dominant mechanism for the extinction of the signal as it propagates into the snow.

Temporal changes in the strength of reflection from the surface, in response to changes in the roughness and density of the uppermost layer of snow, cause the temporal changes in backscatter, denoted Σ_h in section 1.3. These backscatter changes cause a change in echo shape which affects the elevation measurements. Errors in elevation change measurements of several tens of centimetres can be expected from this source, which explains the anomalously large values of Δ_h encountered in section 1.3. However, over periods of a few months, the subsurface scattering remains stable, and the anomaly in Δ_h can be removed by empirically determining the sensitivity of Δ_h to Σ_h. Once this sensitivity is known, it can be used to correct measurements of Δ_h over longer measurement intervals.

The corrected estimate Δ_h' may be affected by changes in the subsurface scattering, but, for measurement intervals of order ten years, the errors are unlikely to exceed 3 cm yr^{-1} in Antarctica and 10 cm yr^{-1} in Greenland, even for step changes of about 1K in temperature, and 10% in accumulation rate, density and roughness. If the climate changes are not persistent but simply the result of interannual variability, smaller errors would be anticipated.

The backscatter anisotropy, denoted Σ_0 in section 1.3, is caused by differences in the extinction coefficient on ascending and descending tracks. A possible cause for this is an azimuthal anisotropy imparted to the grain structure of the snow by the wind - more ground based observations of snow microstructure in the katabatic wind regions are needed to support or refute this hypothesis. The anisostropy persists to a degree as the snow is buried, so it affects the extinction within the body of the snowpack, although it does become weaker with depth. The anisotropy causes discrepancies of several tens of centimetres in satellite altimeter crossovers. The effect is more stable over time than the surface reflection because it is associated with buried snow. As long as it remains stable, this process will not affect the geodetic determination of mass balance, provided equation (1.1) is used to derive the estimate of elevation change.

4. Time variant densification of snow

4.1 Introduction

The density profile through the upper hundred metres is a function of the rate at which snow becomes denser as it is buried - there is almost no melting in Antarctica so each years snowfall is simply buried by the next. The densification rate depends upon the temperature, pressure and density of the snow. The temperature is determined by the air temperature at the surface and the rate of heat conduction and advection within the snow and ice; the pressure on any parcel of snow increases as fresh snow is deposited above it; and the initial density is altered by the action of the winds which compact the surface layer. Any change in surface air temperature, accumulation rate or wind intensity could therefore alter the density profile. Section 4.2 presents a one dimensional model of snow densification. Section 4.3 describes some numerical simulations which were performed to predict the density changes. The results of these simulations are presented in section 4.4 and their accuracy is discussed in section 4.5. Finally, a summary is given in section 4.6.

4.2 Modelling the density profile within firn

The one-dimensional densification of firn is described by a system of partial differential equations expressing the conservation of mass, momentum and energy

$$\frac{\partial\rho}{\partial t}+\frac{\partial(\rho v)}{\partial z}=0 \tag{4.2.1}$$

$$\frac{\partial p}{\partial z}-\rho g=0 \tag{4.2.2}$$

$$\rho c\frac{DT}{Dt}-\frac{\partial}{\partial z}k(\rho)\frac{\partial T}{\partial z}=0 \tag{4.2.3}$$

relating the density ρ, pressure p and velocity v, together with a constitutive law

$$-\frac{1}{\rho}\frac{D\rho}{Dt} = f(p, \rho, T) \tag{4.2.4}$$

In equation (4.2.3) c and k are the specific heat capacity and thermal conductivity of the firn. In equations (4.2.3) and (4.2.4) D / Dt is the material derivative. Equations (4.2.2) and (4.2.4), date from the earliest models of snow densification (Bader 1960; Bader 1962; Kojima 1964). Equation (4.2.3) describes the evolution of temperature in firn (Paterson, 1994). Equations (4.2.1) and (4.2.2) have been obtained by Gray and Morland (1995) as approximations to a more detailed treatment of the ice-air mixture.

Equations (4.2.1) - (4.2.4) remain valid when z is regarded as the depth of firn from a possibly moving surface, provided v is taken as the velocity relative to the surface, and

$$\frac{D}{Dt} \equiv \frac{\partial}{\partial t} + v\frac{\partial}{\partial z} \tag{4.2.5}$$

Henceforth this coordinate system is used, with the surface located at $z = 0$.

Equations (4.2.1) - (4.2.3) have to be solved subject to initial conditions

$$\begin{aligned} \rho(z,0) &= \rho_I(z) \\ T(z,0) &= T_I(z) \end{aligned} \tag{4.2.6}$$

and boundary conditions

$$\begin{aligned} \rho(0,t) &= \rho_s(t) \\ T(0,t) &= T_s(t) \end{aligned} \tag{4.2.7}$$

$$\rho_s v(0,t) = b_s(t) \tag{4.2.8}$$

$$p(0,t) = p_s(t) \tag{4.2.9}$$

which specify the surface density, temperature, accumulation rate and pressure respectively, and

$$T(\infty,t) = T_i \tag{4.2.10}$$

which requires the temperature at great depth to equal that of the underlying ice. Generally the boundary conditions are functions of time.

The functional form for the strain rate f was taken from theoretical models in the literature of the pressure sintering of ice. The strain rate is treated as the sum

$$f = f_{GBS} + f_{DC} + f_{BD} + f_{LD} \tag{4.2.11}$$

of the strain rates arising from four mechanisms: grain-boundary sliding (GBS), dislocation creep (DC), boundary diffusion (BD) and lattice diffusion (LD). The expression used for f_{GBS} was taken from Alley (1987) and the others from a review by Maeno and Ebinuma (1983): the expressions are presented in appendix C.

Equation (4.2.11) does not describe the strain-rate in the layers closest to the surface, where wind and large temperature gradients can cause significant redistribution of mass through sublimation. In these layers equation (4.2.11) was replaced with

$$f = f_0 \tag{4.2.12}$$

a constant.

4.3 Numerical simulations of time variant densification

Assuming that the surface pressure is constant and the surface accumulation rate is strictly positive, the numerical solution of equations (4.2.1) through (4.2.3) may be simplified by introducing the variables $q(t)$ and $q_0(z,t)$ whose definitions are

$$q(t) = g\int^{t} du\, b_s(u) + p_s \tag{4.3.1}$$

$$\left.\begin{aligned} \frac{Dq_0}{Dt} &= 0 \\ q_0(0,t) &= q(t) - p_s \end{aligned}\right\} \tag{4.3.2}$$

The variable q is the sum of the surface pressure and the total weight of material accumulated at the surface. The variable q_0 is the total weight of material accumulated at the time of a particle's deposition at the surface. By the definition equation (4.3.2), q_0 is constant along the particle path.

With this change of variables, equations (4.2.1) - (4.2.4) become

$$p = q - q_0, \tag{4.3.3}$$

(which simply states that the pressure experienced by a particle equals sum of the surface pressure and the weight of material accumulated since the particle's deposition), and

$$\frac{d\rho}{dq} = -\frac{\rho f(p,\rho,T)}{b_s g} \tag{4.3.4}$$

$$\frac{\partial T}{\partial q} - \frac{1}{cb_s}\frac{\partial}{\partial q_0}\left(k\rho g\frac{\partial T}{\partial q_0}\right) = 0 \tag{4.3.5}$$

which are derived in appendix D. Equations (4.3.4) and (4.3.5) were solved on the space

$$\begin{gathered} q \geq p_s \\ q - p_s \leq q_0 \leq q - p_s - P \end{gathered} \tag{4.3.6}$$

that is, between the upper surface of the firn and a surface of constant pressure $p_s + P$. The initial conditions were determined by setting $T = T_s = T_I$ in equation (4.3.5) and integrating equation (4.3.4) to determine the initial density $\rho(q_0, p_s)$. The boundary conditions become $\rho(q - p_s, q) = \rho_s(q)$ and $T(q - p_s, q) = T_s(q)$ at the upper surface, and $T(q - p_s - P, q) = T_i$ at the surface of constant pressure $p_s + P$.

Equations (4.3.4) and (4.3.5) were solved using finite-difference methods. Equation (4.3.4) was solved using an explicit scheme; equation (4.3.5) was solved using a 6-point Crank-Nicholson scheme. The step sizes in q and q_0 were equal. For the numerical calculations described in this thesis, the step size had a value of 100 Pa, the pressure P a value of 4 MPa and the surface pressure p_s a value of 0.1 MPa. Equation (4.2.12) was applied in place of (4.2.11) in the upper 2 m of firn. The thermal conductivity was calculated with the formula $k(\rho) = 2.1(\rho / \rho_i)^2$ W m^{-1} K^{-1}, which provides a good fit to the observations summarised by Yen (1981) for densities up to 600 kg m^{-3} and tends to the thermal conductivity of ice at high densities (Paterson, 1994). The specific heat was also taken from Paterson (1994) as 2009 J kg^{-1} K^{-1}.

Some checks were performed to confirm the correctness of the numerical calculations. A number of calculations were repeated with step sizes between 10 and 500 Pa. In all cases the position of the 4 MPa surface converged to within 1 cm for step sizes less than or equal to 100 Pa. Equation (4.3.5) has the same form as the advectionless thermal diffusion equation. The numerical scheme was tested by solving the constant density slab problem analytically and numerically. The differences between the numerical solution and the analytic solution were insignificant compared with the variations reported in the next section. Finally, a number of calculations were repeated with P set equal to 6 MPa - there was no evidence that the fixing of the temperature at the 4 MPa boundary was significant for the range of times reported on here. For longer timescales, a deeper boundary may be necessary.

With this choice of parameters, the isothermal, steady-state solution for the density and strain rate with the boundary conditions $T_s = T_i = 245$ K, $b_s = 120$ kg m^{-2} a^{-1}, $\rho_s = 360$ kg m^{-3}, $\rho_i = 917$ kg m^{-3} and $f_0 = -10^{-9}$ s^{-1} is shown in figure 4.1. The figure shows the density profile with depth, together with the total strain rate f. The strain rate has a discontinuity at a depth near 40 m. This is the result of an assumption of the densification model that at a density of 834 kg m^{-3} pores within the compact are sealed, and further densification results in an increase in gas pressure within the pores which resists further compression. A detailed discussion of this curve is given in Maeno & Ebinuma (1983).

In the steady-state case one may use equations (4.2.1) and (4.2.8) to show that the strain rate

$$-\frac{1}{\rho}\frac{D\rho}{Dt} \equiv -\frac{v}{\rho}\frac{\partial \rho}{\partial z} = -\frac{b_s}{\rho^2}\frac{\partial \rho}{\partial z} \qquad (4.3.7)$$

Also shown on figure 4.1 is the strain rate from Byrd, West Antarctica, determined using (4.3.7) and the density profile taken from (Gow 1968), for which the boundary conditions given above are appropriate (Gow et al. 1972; Robin 1983).

Figure 4.2 shows the isothermal, steady-state strain rate f with the boundary conditions $T_s = T_i = 250$ K, $b_s = 400$ kg m^{-2} a^{-1}, $\rho_s = 360$ kg m^{-3}, $\rho_i = 917$ kg m^{-3} and $f_0 = -1.6\text{x}10^{-9}$ s^{-1}. These boundary conditions are characteristic of the warmer, higher accumulation rate conditions of the Site 2 core, Greenland (Langway 1967).

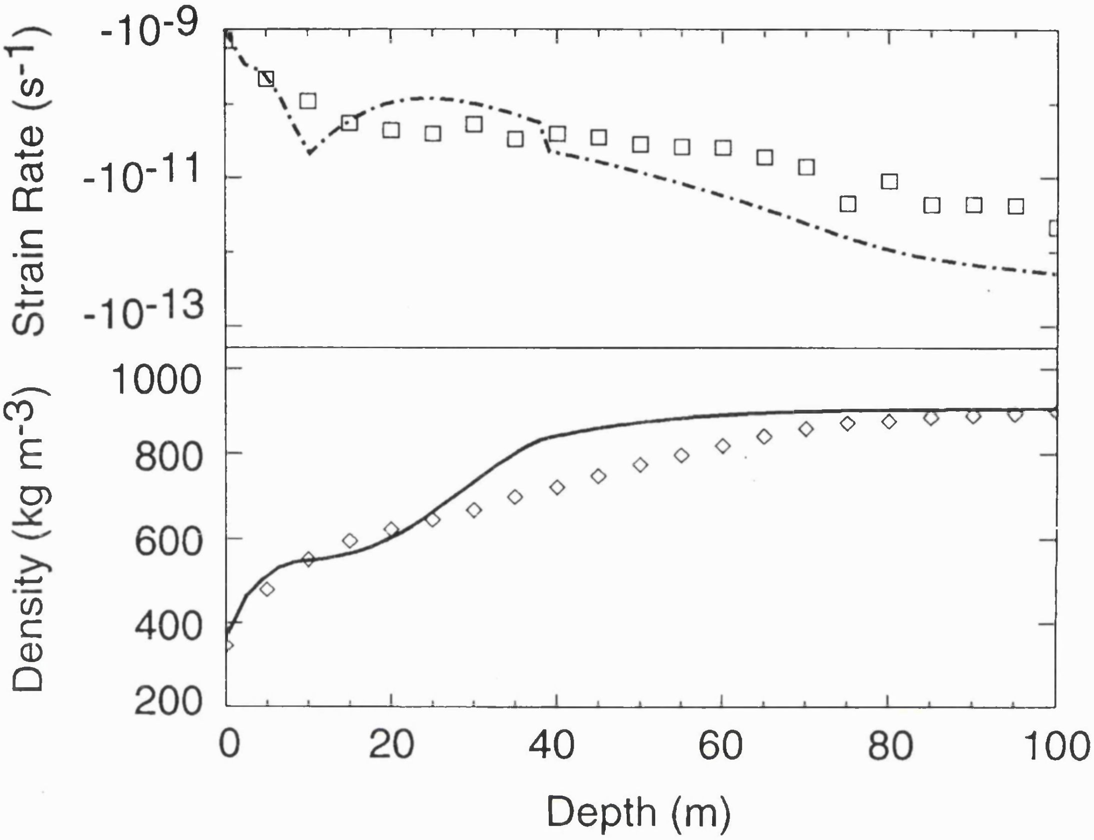

Figure 4.1. Steady state densification at Byrd. The plot shows the observed density profile (diamonds), the modelled density profile (solid line), the observed strain rate (squares) and the modelled strain rate (dashed line).

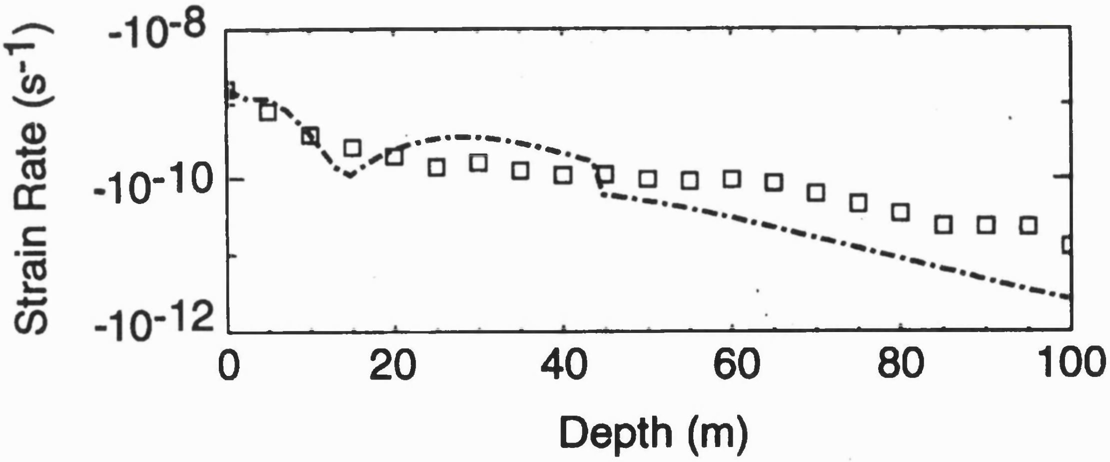

Figure 4.2. The strain rate at Site 2 (squares) and the modelled strain rate (dashed line). The magnitude of the strain rate is greater than at Byrd because of the higher temperature and accumulation rate.

The strain rate derived with equation (4.3.7) from the observed density profile (Langway 1967) is also shown in figure 4.2.

For the low accumulation, cold Byrd conditions, and the higher accumulation, warmer Site 2 conditions, the model predicts the density to within 10% throughout the column. The model overestimates the dislocation creep strain-rate term f_{DC} when the pores are open, and underestimates the strain rate when the pores are sealed. It is the former that causes the over-estimation of the density: once the pores are closed the density is anyway close to that of ice.

4.4 Numerical results for Byrd station, Antarctica and Site 2, Greenland.

Geodetic measurements provide the rate of change of height of the upper surface of an ice sheet. The specific mass balance of the ice sheet, however, is proportional to the rate of change of a constant pressure surface deep within the ice sheet. This arises as follows. Beyond some depth the density of ice is effectively constant. The height of any surface below this depth, with respect to the bed, is linearly related to the mass beneath that surface per unit bed area. If this surface is also a surface of constant pressure, the overlying mass per unit area is constant. It follows that the rate of change of the height of a constant pressure surface, lying sufficiently deep within the ice sheet, is linearly related to the specific mass balance of the ice sheet. Therefore, to geodetically determine the mass balance, the rate of change of the difference between the upper surface and a deep surface of constant pressure must be usefully small.

In this section, the results are described of numerical calculations of the dynamic response of these surfaces to changes in the surface boundary conditions.

Time-variant response to step-function boundary conditions

Figure 4.3 shows the response of the firn to a +1 K step in temperature, applied at $t = 0$, from the equilibrium state shown in figure 4.1 which corresponds to the Byrd surface conditions. The figure shows the perturbation of the 0.1, 0.2, 0.3, 0.4, 0.5 and 0.6 MPa constant pressure surfaces relative to the 4 MPa surface. The dashed line gives the unperturbed depth of the pressure surfaces. The solid line gives the perturbation as functions of time with a scale given in the inset. At 4 MPa, the firn is at the density of ice for all practical purposes. The 0.1 MPa displacement is the displacement of the upper surface relative to the 4 MPa surface.

For the time scales considered here, advection of ice has little significance. Over 200 years, firn will have advected 30 m or so below the surface. The effect of a step change in temperature with depth depends primarily on conduction. The time taken for the temperature step to propagate downwards is clearly seen on figure 4.3. At the 0.2 MPa surface, no perturbation occurs until 40 years after the temperature change at the surface. The bulk of the change occurs at depths between 10 and 30 m, because dislocation creep, the dominant mechanism at these depths, is strongly dependent on temperature. At greater depths the effect of the increase in temperature is very small.

Figures 4.4 and 4.5 show the corresponding curves that result from respectively a 10% increase in accumulation rate and a 10 % increase in surface density.

The effect of a step change in accumulation rate (figure 4.4) is felt immediately throughout the column as an increase in the pressure. The change is fairly evenly distributed throughout the upper 30 m of the column. The response time is shorter than that of temperature. In contrast (figure 4.5), a step change in density (with a fixed accumulation rate) has no instantaneous effect on the column as a whole, but alters the density profile solely as a result of the advection of the denser ice. For the

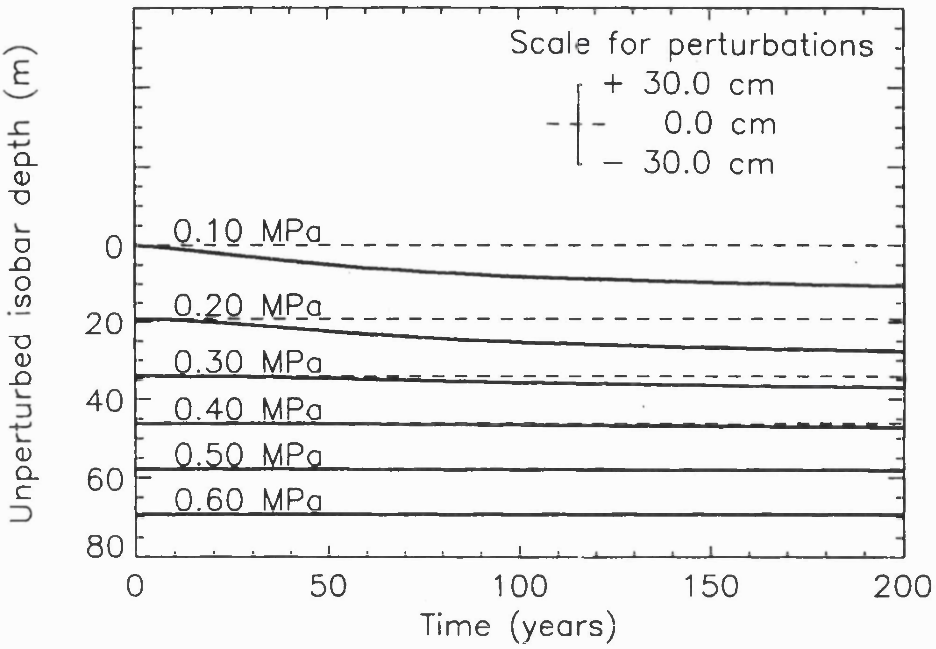

Figure 4.3. The response of the dynamic model to a stepped 1K temperature increase at t=0. The dashed lines show the depth of various constant pressure surfaces prior to the perturbation. For each surface, the solid line shows magnified changes in position relative to the 4 MPa surface (scale provided). The 0.1 MPa surface defines the upper boundary of the ice sheet.

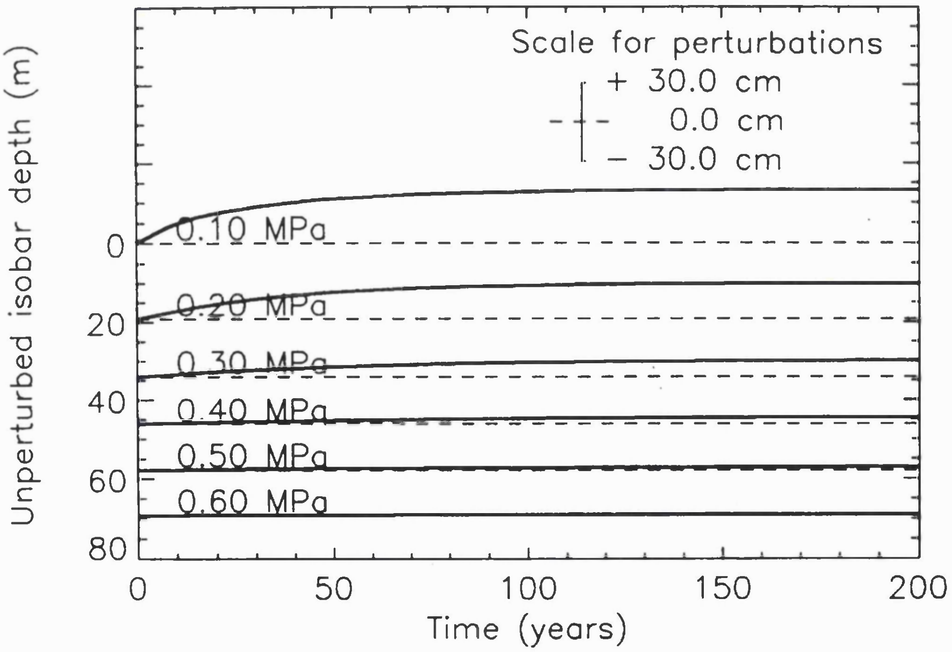

Figure 4.4. The response of the dynamic model to a stepped 10 % increase in accumulation rate. The response time is shorter than for the temperature perturbation although the equilibrium thickness change and the range of depths affected are comparable.

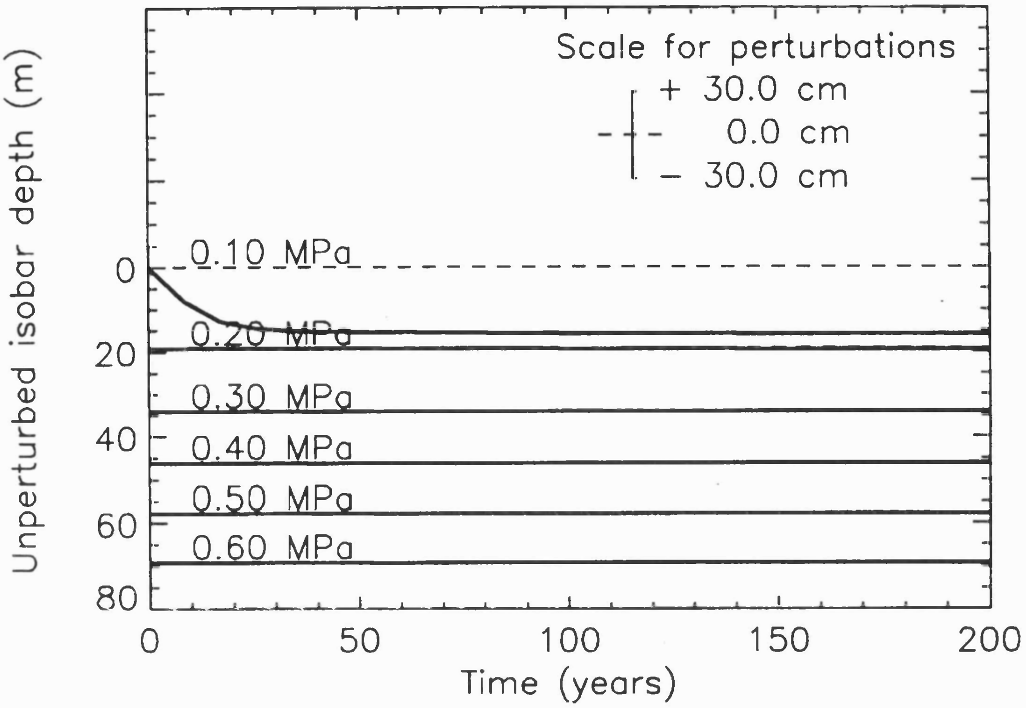

Figure 4.5. The response of the dynamic model to a stepped 10 % increase in surface density. The response time is shorter than for both temperature and accumulation rate perturbations. The density changes are confined to the uppermost 20 m.

	Byrd, Antarctica		Site2, Greenland	
Perturbation	Equilibrium change (m)	Half time (years)	Equilibrium change (m)	Half time (years)
Temperature + 1K	- 0.46	90	- 0.53	45
Accumulation rate + 10 %	+ 0.40	16	+ 0.46	6
Surface density + 10 %	- 0.48	8	- 0.55	3

Table 4.1. The response of the model to step perturbations of the boundary conditions. For each perturbation and location, the table gives the equilibrium change in firn density, expressed as an equivalent change in ice-sheet thickness, and the time taken for half of this equilibrium response to occur.

timescales considered here, this effects only the shallow firn. Moreover, denser ice at the surface simply results in reduced densification lower down the column at a later time. The displacement of the 0.2 MPa surface, just visible on figure 4.5 after 140 years, is very small.

The results show that changes in the density profile due to a change in surface conditions will continue for decades after the change at the surface. In all cases, the response is a gradual rise or fall to an asymptote describing the new, equilibrium profile. This rise can be characterised by the time taken for the surface perturbation to reach half its new equilibrium value. Table 4.1 gives the value of the asymptote and the half times for the cases shown in figures 4.3, 4.4 and 4.5, together with those values corresponding to the strain rate profile shown in figure 4.2, characteristic of the Site 2 surface conditions.

Time-variant response to randomly fluctuating boundary conditions

Random fluctuations of the surface boundary conditions were simulated with a Gaussian time series with an exponential correlation function with a correlation duration of one year. (The precise form of the correlation function is of little significance when its correlation duration is less than the response times of the firn.) Figure 4.6 shows the perturbation of the profile of figure 4.1, corresponding to the Byrd surface conditions, driven by a random perturbation in accumulation rate with a standard deviation equal to 10% of the unperturbed accumulation rate. The time origin of in figure 4.1 occurs 200 years later than the start of the perturbation to ensure any transient effects are small.

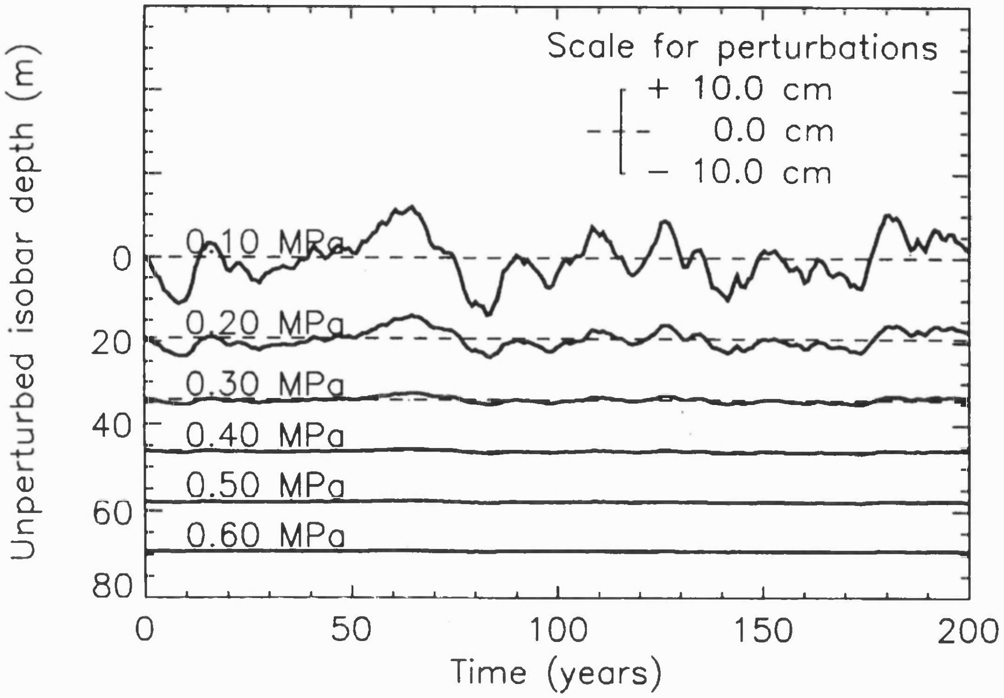

Figure 4.6. The response of the dynamic model to a randomly fluctuating accumulation rate with correlation duration of one year and standard deviation 10 % of the mean. The response of the firn density is correlated over intervals of about a decade.

	Standard deviation of d/τ (mm yr^{-1})					
	Byrd, Antarctica			Site 2, Greenland		
Perturbation, standard deviation	τ = 10 yr	τ = 20 yr	τ = 30 yr	τ = 10 yr	τ = 20 yr	τ = 30 yr
Temperature 1K	1	1	1	1	1	1
Accumulation rate 10 %	6	4	3	10	7	5
Surface density 10 %	13	7	5	22	16	11

Table 4.2. The response of the model to random perturbations of the boundary conditions. Over any measurement duration τ, some component d of the observed thickness change will be due to density changes. The table gives the standard deviation of d / τ for various perturbations, locations and measurement durations. Only secular changes in ice thickness larger than these values can confidently be ascribed to changes in the mass of the ice sheet.

Some of the character of the response in figure 4.4 to a step in accumulation are visible on figure 4.6. The fluctuations in accumulation rate at the surface are immediate, with advection playing little role. The fluctuations in surface accumulation rate, that would appear a white process on the time-scale of figure 4.6, are smoothed, and are correlated over an interval similar to the 16-year half time of the step response. (Since the processes dealt with here are not linear, one should not necessarily expect any simple relation between these two intervals.) The magnitude of the effects at depth is less pronounced than was the case with the step response; compare, for example, the fluctuations of the 0.2 MPa surface in figure 4.6 with the corresponding curve in figure 4.4. Allowing for the differences in the step responses, very similar remarks may be made concerning random fluctuations in surface temperature and density.

Geodetic measurements often estimate mass-balance by differencing two height measurements separated by an interval τ, and the question arises as to the contribution of the densification over this interval. It is obvious from figure 4.6 that when τ is rather less than the half-time, the average rate of change in height between the upper and deep pressure surfaces can be greater than when τ is much larger than the half time. If $d(\tau,t)$ denotes the change in the separation of the two surfaces between times t and $t+\tau$, then Table 4.2 gives the standard deviation of d/τ for a number of values of τ. Assuming normally distributed errors, doubling the values in table 4.2 gives an estimate of the 95% confidence interval for measured elevation changes - about ± 4 cm yr^{-1} (Antarctica) and ± 7 cm yr^{-1} (Greenland) for a measurement interval of ten years. These values assume that the temperature, accumulation rate and density changes occur simultaneously, and are correlated to give the maximum error - in practise smaller errors might be anticipated.

4.5 Limitations of the model

The strain rates predicted by the constitutive relationship sometimes disagree with the ice core data by a factor of ten. There are large uncertainties associated with many of the material parameters used in the constitutive relationship. In addition, the models used in equation (4.2.11) may oversimplify the stresses experienced by grains within the firn (Maeno et al. 1983; Alley 1987).

To estimate the sensitivity of the results to errors in the constitutive relationship, the calculations were repeated with the strain rate artificially increased by a factor of ten, and with the strain rate reduced by a factor of ten. The results of this exercise suggest that the equilibrium thickness changes in table 4.1, and the timescales upon which they are reached, are accurate to within a factor of two. As the strain rate was artificially increased, the magnitude of thickness changes and their timescales decreased together - as a consequence, rates of elevation change remained rather similar to the unperturbed case. The values presented in table 4.2 are thus reasonably insensitive to the likely errors in the constitutive relationship, and are certainly accurate within a factor of two.

The treatment of heat transfer could have been more sophisticated. Following Paterson (1994), a source term could have been added to equation (4.2.3) to account for the small amount of heat generated by the densification itself. Also, perturbing the surface temperature about a positive trend would allow the change in surface temperature caused by horizontal advection of the firn column to be incorporated. Some calculations were performed in which the surface temperature was perturbed about a seasonal cycle rather than the mean annual temperature; this did not change the effect of the perturbations greatly.

The treatment of mass transfer could also have been refined. A higher dimensional model may be needed to predict the densification in areas where the divergence of the horizontal velocity is large: there is evidence that densification under these conditions is also influenced by deviatoric stresses within the firn (Alley and Bentley 1988). Around the margins of Greenland, melting may give rise to larger density changes than occur in the dry snow considered here (Braithwaite et al. 1994). A fuller treatment of the air, ice and water mixture would be necessary to model the densification in areas where melting occurs, or to explicitly include the effects of sublimation in the upper 2 m of firn. Given the large uncertainties in the constitutive relationship these refinements were considered unlikely to increase the usefulness of the model.

4.6 Chapter Summary

This chapter was concerned with whether the natural variability of climate at the surface of ice sheets gives rise to changes in the densification of firn large enough to affect geodetic estimates of their mass balance. To deal with this question, a time-variant one-dimensional numerical model of the densification of dry firn was constructed to simulate the fluctuations in ice sheet thickness.

Temperature-driven changes are transmitted due to conduction and principally effect the density of the upper 30 metres. Accumulation-driven changes are felt immediately throughout the firn column, with the largest changes in density in the upper 30 metres. Density-driven changes are advected through the column, but mainly effect only the upper 10 m; below this the initial differences in density at the surface are greatly diminished.

The variations in the density profile at a low temperature, low accumulation rate site in Antarctica and a warmer, higher accumulation site in Greenland were simulated.

Two types of meteorological forcing were considered: a step change, representing a sudden and persistent change in the climatic conditions at a site; and random forcing, representing the natural variations in weather expected from year to year. Persistent changes of order 1K in temperature, and 10% in accumulation rate and initial density, could cause errors of about 5 $\mathrm{cm\,yr^{-1}}$ in Antarctica and about 14 $\mathrm{cm\,yr^{-1}}$ in Greenland. Interannual variability with standard deviation of 1K in temperature, and 10% in accumulation rate and initial density, could cause errors of 4 $\mathrm{cm\,yr^{-1}}$ in Antarctica and 7 $\mathrm{cm\,yr^{-1}}$ for Greenland.

5. Overall summary and conclusions

5.1 Summary

The backscatter is mostly generated by reflections at layer interfaces within the snow. Backscatter from snow grains accounts for only about 1% of the total backscatter - much less than assumed by some previous models of the altimeter signal. The main influence that scattering by snow grains has upon the radar echo is through attenuating the signal as it propagates into the snow.

In Antarctica, over periods of up to a year, the scattering from beneath the surface does not change. However, the reflection from the air snow interface changes almost everywhere from month to month as the density and roughness of the surface layer vary. This variation would cause large errors in the elevation change of the type shown in figure 1.1a, but these may be corrected using measurements of the backscatter over the measurement interval. The corrected measurements are sensitive to changes in the structure of the deeper snow which may occur on timescales of many years. The sensitivity of the subsurface scattering to changes in temperature, accumulation rate and density was investigated, and the possibility of using this sensitivity, together with passive microwave observations, to measure accumulation rates on the plateau was discussed. For changes in climate comparable to those simulated, the errors caused by time variant snow densification are unlikely to exceed 3 cm yr^{-1} in Antarctica and 10 cm yr^{-1} in Greenland.

Satellite crossover measurements in windy regions of Antarctica are affected by an anisotropy in the grain structure of the upper few metres of snow. The mechanism responsible for the anisotropy could not be established unambiguously in this thesis, since this would require detailed, three dimensional observations of the grain structure from regions of strong katabatic winds, and these were not available. The anisotropy was observed to be stable over periods of about a year. If it remains stable over much longer intervals it will not affect measurements of mass balance, provided that elevations from ascending and descending tracks are given equal weight throughout the measurement interval. There is some evidence that the effect is associated with the direction and speed of the wind, so if the atmospheric circulation changes, errors in the elevation change measurement might be anticipated.

Temporal changes in the density profile throughout the ice sheets were investigated using a numerical model. Changes in the surface temperature affect the temperature of the upper hundred metres or so, principally by conduction. This causes changes in the density profile, which can affect the elevation of the surface independently of the mass balance. The effect may be several tens of centimetres for a 1K change in temperature. Changes in accumulation rate similarly alter the density profile, by altering the pressure experienced by the underlying ice. Finally, changes in the density of the surface layer of snow can affect the profile as the denser ice is advected downwards - a negative feedback operates in this case though, because the denser ice is compressed less readily. The timescales for changes in the density profile in Antarctica are about 100 years for changes in temperature, about 20 years for changes in accumulation rate and about 10 years for changes in initial density. In Greenland the timescales are about half as long. For changes in climate similar to those simulated, the errors caused by time variant snow densification are unlikely to excede 5 cm yr^{-1} in Antarctica and 14 cm yr^{-1} in Greenland.

5.2 Conclusion

The main question addressed by this thesis has been whether it is realistic to expect radar altimeters to improve upon current estimates of the mass balance of the Greenland and Antarctic ice sheets. In chapter 1, the present uncertainties in mass balance were stated in terms of elevation change as ±5 $\mathrm{cm\,yr^{-1}}$ for Antarctica and ±25 $\mathrm{cm\,yr^{-1}}$ for Greenland.

This thesis has studied the effect of changes in climate of about 1K in temperature and 10% in accumulation rate and surface density and surface roughness. These changes are similar to observed variations at sites in the polar regions (Langway 1967; Gow 1968; Schwerdtfeger 1984; Goodwin 1991; Isaksson and Karlen 1994). The resulting errors in the geodetic measurement of mass balance, described in section 5.1, are comparable to the present uncertainties in mass balance. However, it should be stressed that these are the maximum errors that could realistically be expected at a single site, and a significant reduction would be expected when averaging these measurements over areas the size of Greenland and Antarctica. It therefore seems very likely indeed that satellite radar altimeters will improve upon current estimates of the mass balance of Greenland and Antarctica as a whole; although more regional investigations of the mass balance may well be hampered by changes in the snow properties brought about by the varying climate.

Even though they may be smaller than the current uncertainties, the results of this thesis suggest that errors from the effects of climate upon the snowpack may well turn out to be the largest error in measurements of mass balance using satellite radar altimetry. Therefore, in order to estimate confidence intervals for these mass balance measurements, it will be essential to accompany the altimeter surveys with investigations into climatic conditions during the measurement interval and the preceding decades. Similarly, the scattering should be monitored throughout the measurement interval, using the methods described in chapter 2, or some other means. The more stable the average climate and scattering properties are when averaged over the survey region, the greater the confidence in measurements of ice sheet mass balance from satellite radar altimeters will become.

5.3 Limitations and further work.

The treatment of changes in scattering considered in chapter 3 was limited to step changes in the meteorological boundary conditions. To consider the effect of more realistic changes in climate upon the radar echo, the scattering model described in chapter 3 could be coupled to a model describing the time varying structure of the snow. The densification model developed in chapter 4 would provide the first step to such a model, although it would be essential to model the temporal evolution of the grain size profile as well to accurately determine the extinction. Changes in grain size are largely controlled by sublimation effects, so the vapour phase of the snowpack would have to be included in such a model. Including the vapour phase would also allow a more realistic treatment of the upper two metres of snow than that assumed in chapter 4.

Once a coupled model describing the time varying scattering and densification had been developed, it could be used to study the effect of observed changes in climate upon the mass balance measurement, as opposed to the somewhat idealised perturbations considered in chapters 2 and 3. In the last few years, the performance of General Circulation Models (GCMs) in the polar regions has improved to the extent that they could provide realistic estimates of the spatial and temporal variations in temperature, accumulation rate and wind speed, over any chosen measurement interval and survey region.

In this thesis, the meteorological boundary conditions have been expressed in terms of accumulation rate, temperature, surface density and surface roughness - the latter two were used to study the effect of changes in the weathering of the surface snow layer, and this is principally controlled by the action of the wind. The results of chapters 2 and 3 show that the effect of wind upon the snow structure is one of the most important factors determining the shape of the radar echo. More effort is needed to quantify the effect of wind upon the snow roughness, density and grain size before windfields from GCMs could be used to drive a coupled model of densification and scattering.

Assuming that the effects of the wind could be incorporated, a model of the scattering and densification driven by output from a GCM would reveal the spatial scale over which the elevation errors are correlated. Uncertainty in this matter, more than any other, limits the conclusions that can be drawn about the accuracy of measurements of ice sheet mass balance from radar altimeters.

Recent time series of elevation change from Antarctica show a pronounced seasonal cycle (Ridout, manuscript in preparation). The amplitude of this seasonal signal is larger than might be expected, given the seasonal fluctuations in accumulation rate predicted by the European Centre for Medium Range Weather Forecasting (ECMWF) GCM. The signal may be caused by seasonal variations in the densification rate driven by the annual temperature cycle - this is being investigated at MSSL using the densification model developed in chapter 4.

It should be stressed that all the results obtained in this thesis are applicable to dry snow only. While this is appropriate for virtually all of Antarctica, a sizeable fraction of the Greenland ice sheet undergoes seasonal melting. This complicates the scattering problem because even small amounts of liquid water have a large effect upon the effective dielectric permittivity of the snow. Even during the winter, when all water is frozen, the presence of ice lenses and pipes (formed by the percolation and refreezing of meltwater during the summer) adds to the complexity of modelling the densification and scattering of the snow.

The investigation into measuring accumulation rate from space described in appendix B must be viewed as preliminary at this stage. Some potential techniques for reducing the errors were discussed in that appendix. Further work will also be needed to quantify these errors and assess the value of the method compared to other approaches.

References

Abramowitz, M. and I. Stegun, Eds. (1965). Handbook of Mathematical Functions. New York, Dover Publications, Inc.

Alley, R. B. (1987). "Firn densification by grain-boundary sliding: a first model." Journal de Physique **48**(Colloque C1, Supplement au no. 3): 249-256.

Alley, R. B. (1988). "Concerning the deposition and diagenesis of strata in polar firn." J. Glaciol. **34**(118): 283-290.

Alley, R. B. and C. R. Bentley (1988). "Ice-core analysis on the Siple Coast of West Antarctica." Annals of Glaciology **11**: 1 - 7.

Alley, R. B., E. S. Saltzman, K. M. Cuffey and J. J. Fitzpatrick (1990). "Summertime formation of depth hoar in central Greenland." Geophysical Research Letters **17**(12): 2393-2396.

Bader, H. (1960). Theory of densification of dry snow on high polar glaciers, 1. CRREL Research Report 69.

Bader, H. (1962). Theory of densification of dry snow on high polar glaciers, 2. CRREL Research Report 108.

Bamber, J. L. (1994). "Ice sheet altimeter processing scheme." Int. J. Remote Sensing **15**(4): 925-938.

Bentley, C. R. and M. B. Giovinetto (1991). Mass balance of Antarctica and sea level change. Polar Regions and Climate Change, University of Alaska, Fairbanks, Braithwaite, R. J., M. Laternser and W. T. Pfeffer (1994). "Variations of near-surface firn density in the lower accumulation area of the Greenland ice sheet, Pakitsoq, West Greenland." J. Glaciol. **40**(136): 477 - 485.

Breuck, W. D. (1968). Queen Maud Land traverse 3, 1967-1968. Snow sampling program of the Centre of Polar Studies, Ohio State University. Ohio State University.

Bromwich, D. (1995). "Ice sheets and sea level." Nature **373**: 18-19.

Brown, G. S. (1977). "The average impulse response of a rough surface and its applications." I.E.E.E. Trans. antennas propagat. **Vol. AP-25**(No. 1): pp 67-74.

Budd, W. F., P. A. Reid and L. J. Minty (1995). "Antarctic moisture flux and net accumulation from global atmospheric analyses." Annals of Glaciology **21**: 149-156.

Coble, R. L. (1970). "Diffusion models for hot pressing with surface energy and pressure effects as driving stresses." Journal of Applied Physics **41**(12): 4798 - 4807.

Colbeck, S. C. (1983). "Ice crystal morphology and growth rates at low supersaturations and high temperatures." J. Appl. Phys. **54**(5): 2677 - 2682.

Colbeck, S. C. (1983). "Theory of metamorphism of dry snow." J. Geophys. Res. **88**(C9): 5475-5482.

Comiso, J. C. and H. J. Zwally (1982). "Radiative transfer modeling of microwave emission and dependence on firn properties." Annals of Glaciology **3**: 54 - 58.

Cudlip, W., D. R. Mantripp, C. L. Wrench, H. D. Griffiths, D. V. Sheehan, M. Lester, R. P. Leigh and T. R. Robinson (1994). “Corrections for altimeter low-level processing at the Earth Observation Data Centre.” Int. J. Remote Sensing **15**(4): 889-914.

Davis, C. H. (1995). “Synthesis of passive microwave and radar altimeter data for estimating accumulation rates of dry polar snow.” Int. J. Remote Sensing **16**(11): 2055 - 2067.

Davis, C. H. (1995). A reassessment of the growth of the Greenland Ice Sheet using Seasat and Geosat altimeter data referenced to the same geoid. IGARSS, Florence, IEEE.

Davis, C. H. and R. K. Moore (1993). “A combined surface- and volume-scattering model for ice-sheet radar altimetry.” J. Glaciol. **39**(133): 675-685.

Douglas, B. C., R. E. Cheney, L. Miller and R. W. Agreen (1990). “Greenland ice sheet: is it growing or shrinking?” Science **248**: 288-289.

Fily, M. and J. P. Benoist (1991). “Large-scale statistical study of Scanning Multichannel Microwave Radiometer (SMMR) data over Antarctica.” J. Glaciol. **37**: 129-139.

Giovinetto, M. B. and C. R. Bentley (1985). “Surface balance in ice drainage system of Antarctica.” Antarctic J. U.S. **20**: 6-13.

Giovinetto, M. B., N. M. Waters and C. R. Bentley (1990). “Dependence of Antarctic surface mass balance on temperature, elevation, and distance to open ocean.” J. Geophys. Res. **95**(D4): 3517-3531.

Goodwin, I. D. (1991). “Snow-accumulation variability from seasonal surface observations and firn-core stratigraphy, eastern Wilkes Land, Antarctica.” J. Glaciol. **37**(127): 383-387.

Gow, A. J. (1968). Deep core studies of the accumulation and densification of snow at Byrd Station and Little America V, Antarctica. CRREL Research Report 197.

Gow, A. J. (1969). “On the rates of growth of grains and crystals in south polar firn.” J. Glaciol. **8**(53): 241-252.

Gow, A. J., F. d. Blander, G. Crozaz and E. Picciotto (1972). “Snow accumulation at "Byrd" station, Antarctica.” J. Glaciol. **11**(61): 59 - 64.

Gray, J. M. N. T. and L. W. Morland (1995). “The compaction of polar snowpacks.” Cold Regions Science and Technology **23**: 109 - 119.

Huybrechts, P. (1990). “A 3D model for the Antarctic ice sheet: a sensitivity study on the glacial-interglacial contrast.” Clim. Dyn. **5**: 79-92.

Isaksson, E. and W. Karlen (1994). “Spatial and temporal patterns in snow accumulation, western Dronning Maud Land, Antarctica.” J. Glaciol. **40**(135): 399-414.

Ishimaru, A. (1978). Vol. I: Single scattering and transport theory; vol II: Multiple Scattering, Turbulence, Rough Surfaces and Remote Sensing. New York, Academic.

Jacobs, S. S., H. H. Helmer, C. S. M. Doake, A. Jenkins and M. Frolich (1992). "Melting of ice shelves and the mass balance of Antarctica." J.Glaciol. **Vol. 38**(No. 130): 375-387.

Kaspner, W. R., R. B. Alley, C. A. Shuman, S. Anandakrishnan and P. M. Grootes (1995). "Dominant influence of atmospheric circulation on snow accumulation in Greenland over the past 18,000 years." Nature **373**: 52-54.

Keller, V. W. and J. Hallet (1982). "Influence of air velocity on the habit of ice crystal growth from the vapor." Journal of Crystal Growth **60**: 91 -106.

Kojima, K. (1964). Densification of snow in Antarctica. Antarctic Snow and Ice Studies, Antarctic Research Series 2 Ed. M. Mellor. American Geophysical Union.

Kostecka, J. M. and I. M. Whillans (1988). "Mass Balance Along Two Transects of the West Side of the Greenland Ice Sheet." J. Glaciol. **34**: 31-39.

Kotlyakov, V. M. (1961). "Snow cover in the Antarctic and its role in modern glaciation of the continent." Moskow: Akad. Nauk SSSR (text in Russian) :

Langway, C. C., Jr. (1967). Stratigraphic analysis of a deep ice core from Greenland. CRREL Research Report 77.

Long, D. G. and M. R. Drinkwater (1994). "Greenland ice-sheet surface properties observed by the Seasat-A scatterometer at enhanced resolution." J. Glaciol. **40**(135): 213-230.

Maeno, N. and T. Ebinuma (1983). "Pressure sintering of ice and its implication to the densification of snow at polar galciers and ice sheets." J. Phys. Chem. **87**: 4103-4110.

Matzler, C. (1996). "Microwave permittivity of dry snow." IEEE Transactions on Geoscience and Remote Sensing **34**(2): 573-581.

Mellor (1964). Cold Regions Science and Engineering 2-C1. Snow and Ice on the Earth's Surface. Cold Regions Research and Engineering Laboratory, Hanover, New Hampshire.

Murphy, J. M. and J. F. B. Mitchell (1995). "Transient response of the Hadley Centre Coupled Ocean-Atmosphere Model to Increasing Carbon Dioxide. Part II: Spatial and Temporal Structure of Response." Journal of Climate **8**: 57-80.

Papoulis, A. (1991). Probability, random variables, and stochastic processes. New York, McGraw-Hill, Inc.

Partington, K. C., J. K. Ridley, C. G. Rapley and H. J. Zwally (1989). "Observations of the surface properties of the ice sheets by satellite radar altimetry." J. Glaciol. **35**(120): 267-275.

Paterson, W. S. B. (1994). The Physics of Glaciers. Elsevier Science Limited, Oxford.

Peltier, W. R. and A. M. Tushingham (1991). "Influence of glacial isostatic adjustment on tide gauge measurements of secular sea level." J. Geophys. Res. **96**(B4): pp 6779-6796.

Press, W. H., B. P. Flannery, S. A. Teukolsky and W. T. Vetterling (1986). Numerical recipies: the art of scientific computing. Cambridge, Cambridge University Press.

Rack, W. (1995). Streuverhalten und Morpologie der antarktischen Schneedecke aus Scatterometer-Messungen von ERS-1. Diploma Thesis, Science Faculty, University of Innsbruck.

Reeh, N. and N. S. Gundestrup (1985). "Mass Balance of the Greenland Ice Sheet at Dye 3." J. Glaciol. **31**: 198-200.

Remy, F. and J. F. Minster (1991). "A comparison between active and passive microwave measurements of the Antarctic ice sheet and their association with the surface katabatic winds." J. Glaciol. **37**(125): 3-10.

Remy, F., M. Ledroit and J. F. Minster (1992). "Intensity of a radar altimeter over continental ice sheets. A potential measurement of surface roughness and katabatic wind intensity." J. Glaciol. **36**: 133 - 142.

Remy, F., P. Femenias, M. Ledroit and J. F. Minster (1995). "Empirical microwave backscattering over Antarcica: application to radar altimetry." Journal of electromagnetic waves and applications **9**(3): 463 - 474.

Ridley, J. K. and K. C. Partington (1988). "A model of satellite radar altimeter return from ice sheets." Int. J. Remote Sensing **vol. 9**(No. 4): pp 601-624.

Robin, G. d. Q. (1983). The climate record in polar ice sheets. Cambridge University Press, Cambridge.

Rott, H. and W. Rack (1995). Characteristation of Antarctic firn by means of ERS-1 scatterometer measurements. Proceedings of IGARSS 95, Florence, IEEE.

Rundle, A. S. (1971). "Snow accumulation and stratigraphy on the Antarctic plateau." Antarctic Research Series **16**: 239-255.

Schwerdtfeger, W. (1984). Weather and Climate of the Antarctic. Elsevier Science Publishing Company, Amsterdam.

Schytt, V. (1958). "Snow studies inland." Glaciology II, **IV**: 65-115. Scientific results of the Norwegian-British-Swedish Antarctic Expedition. Oslo.

Skolnik, M. I. (1970). Radar Handbook. McGraw-Hill, Inc.

Stuart, A. W. and A. J. Heine (1961). IGC Antarctic glaciological data field work 1959 - 1960. The Ohio State University Research Foundation. Ohio State University, Boulder, Ohio.

Sturm, M. and J. B. Johnson (1991). "Natural convection in the subarctic snow cover." J. Geophys. Res. **96**(B7): 1,657 - 11,671.

Surdyk, S. and M. Fily (1995). "Results of a stratified snow emissivity model based on the wave approach: Aplication to the Antarctic ice sheet." J. Geophys. Res. **100**(C5): 8837-8848.

Torres, R. (1990). ERS-1 Radar Altimeter Antenna E.M. Test Report, European Space Agency, Paris.

Tsang, L., J. A. Kong and R. T. Shin (1985). Theory of microwave remote sensing. New York, Wiley-Interscience.

Ulaby, F. T., R. K. Moore and A. K. Fung (1986). Microwave remote sensing: active and passive. Norwood, MA 02062, Artech House, Inc.

van der Veen, C. J. (1993). "Interpretation of short-term ice-sheet elevation change inferred from satellite altimetry." Climatic Change **23**: 383 - 405.

van der Wal, R. S. W. and J. Oerlemans (1994). "An energy balance model for the Greenland ice-sheet." Global and planetary change **9**(1-2): 115-131.

Warrick, R. A., C. L. Provost, M. F. Meier, J. Oerlemans and M. Woodworth (1995). Changes in Sea Level. Climate Change 1995, The Science of Climate Change Eds. J. T. Houghton, L. G. M. Filho, B. A. Callanderet al. Cambridge, Cambridge University Press.

Warrick, R. and J. Oerlemans (1990). Sea level rise. Climate Change: the IPCC Scientific assesment Eds. J. Houghton, G. Jenkins and J. Ephraums. Cambridge, Cambridge University Press. pp 257-281.

West, R., L. Tsang and D. P. Winebrenner (1993). "Dense medium radiative transfer theory for two scattering layers with a Rayleigh distribution of particle sizes." IEEE Trans Geoscience and Remote Sensing **31**(2): 426-436.

Wilkinson, D. S. (1988). "A Pressure-sintering model for the densification of polar firn and glacier ice." J. Glac. **34**(No. 116): 40-45.

Wilkinson, D. S. and M. F. Ashby (1975). “Pressure sintering by power law creep.” Acta Metallurgica **23**: 1277- 1285.

Wingham, D. J. (1995). “A method for determining the average height of a large topographic ice sheet from observations of the echo received by a radar altimeter.” J. Glaciol. **41**(137): 125-141.

Wingham, D. J. (1995). “Elevation change of the Greenland Ice Sheet and its measurement with satellite radar altimetry.” Phil. Trans. R. Soc. Lond. A **352**: 335 - 346.

Yen, Y. C. (1981). Review of thermal properties of snow, ice and sea ice. CRREL Report 81 - 10.

Zwally, H. J. (1977). “Microwave emissivity and accumulation rate of polar firn.” J. Glaciol. **18**(79): 195-215.

Zwally, H. J., A. C. Brenner, J. A. Major, R. A. Bindschadler and J. G. Marsh (1989). “Growth of Greenland ice sheet: measurement.” Science **246**: 1587-1589.

Zwally, H. J., A. C. Brenner, J. A. Major, R. A. Bindschadler and J. G. Marsh (1990). “Greenland ice sheet: is it growing or shrinking? - Response.” Science **248**: 288-289.

Appendix A: Analytical Solution to equation 2.2.37 for Gaussian Antenna pattern.

This appendix gives an analytical solution for the resolvent kernel K_r using the Gaussian antenna approximation introduced by (Brown 1977). The results shown in this thesis were obtained by the numerical method described in section 2.4. Subsequently, however, this analytical solution was developed which should be simpler to implement and computationally faster.

Taking the Laplace transform of equation (2.2.24) gives

$$1 = L[I(t)]L[K_r(t)] \tag{A.1}$$

so that

$$K_r(t) = L^{-1}\left[\frac{1}{L[I(t)]}\right] \tag{A.2}$$

When the antenna beam pattern is Gaussian as approximated by (Brown 1977)

$$g(\sin\theta) = G_0 \exp\left[-\frac{2\sin^2\theta}{\gamma_b}\right] \tag{A.3}$$

the kernel $I(t)$ can be obtained by evaluating equation (2.2.18) analytically. The result is

$$I(t) = C_k e^{-\alpha t} I_0\left(\sqrt{\beta t}\right) \tag{A.4}$$

where I_0 is the modified Bessel function (Abramowitz and Stegun 1965) and

$$C_k = \frac{G_0^2 E_t \lambda^2 c}{4\eta(4\pi)^2 h_0^3 L_s} exp\left(-\frac{16}{\gamma_b \eta^2} sin^2\left(\tfrac{1}{2}\Delta\right)\right) \tag{A.5}$$

$$\alpha = \frac{4c}{\gamma_b h_0 \eta} \tag{A.6}$$

$$\beta = \frac{256 c\, sin^2\left(\tfrac{1}{2}\Delta\right)}{h_0 \eta^3 \gamma_b^2} \tag{A.7}$$

The Laplace transform of $I(t)$ can be found by replacing I_0 by the following expansion (Abramowitz et al. 1965)

$$I_0(\sqrt{\beta t}) = \sum_{n=0}^{\infty} \frac{1}{(n!)^2} \left(\frac{\beta t}{4}\right)^n \tag{A.8}$$

so that

$$L[I(t)] = L\left[C_k e^{-\alpha t} \sum_{n=0}^{\infty} \frac{1}{(n!)^2} \left(\frac{\beta t}{4}\right)^n\right] = C_k \sum_{n=0}^{\infty} \frac{1}{(n!)^2} \left(\frac{\beta}{4}\right)^n L\left[t^n e^{-\alpha t}\right] \tag{A.9}$$

From tables of Laplace transforms (Gradshteyn et al. 1965)

$$L\left[t^n e^{-\alpha t}\right] = \frac{\Gamma(n+1)}{(p+\alpha)^{n+1}} \tag{A.10}$$

substituting A.10 into A.9 and using the identity

$$\Gamma(n+1) = n! \tag{A.11}$$

provides

$$L[I(t)] = C_k \sum_{n=0}^{\infty} \frac{1}{n!} \left(\frac{\beta}{4}\right)^n \frac{1}{(p+\alpha)^{n+1}} = C_k \frac{1}{(p+\alpha)} exp\left(\frac{\beta}{4(p+\alpha)}\right) \tag{A.12}$$

Substituting equation (A.12) into equation (A.2) and using the shift theorem of Laplace transforms then gives

$$K_r(t) = \frac{1}{C_k} e^{-\alpha t} L^{-1}\left[p\, exp\left(-\frac{\beta}{4p} \right) \right] \tag{A.13}$$

Expanding the exponential gives

$$K_r(t) = \frac{1}{C_k} e^{-\alpha t} L^{-1}\left[p \sum_{n=0}^{\infty} \frac{1}{n!} \left(-\frac{\beta}{4p} \right)^n \right] \tag{A.14}$$

The inverse Laplace transform may then be evaluated using the following identities (Gradshteyn et al. 1965)

$$\begin{aligned} &L^{-1}[p] = \delta'(t) \\ &L^{-1}[1] = \delta(t) \\ &L^{-1}\left[\frac{1}{p^{n+1}} \right] = \frac{t^n}{n!}, \quad n = 0, 1, 2, \ldots \end{aligned} \tag{A.15}$$

giving the resolvent kernel

$$K_r(t) = \frac{1}{C_k} e^{-\alpha t} \left(\delta'(t) - \frac{\beta}{4}\delta(t) + \left(\frac{\beta}{4} \right)^2 \sum_{n=0}^{\infty} \frac{1}{n!(n+2)!} \left(-\frac{\beta t}{4} \right)^n \right) \tag{A.16}$$

Using the identity for the Bessel function J_2 (Abramowitz et al. 1965)

$$J_2(z) = \left(\frac{z}{2} \right)^2 \sum_{n=1}^{\infty} \frac{1}{n!(n+2)!} \left(-\frac{z^2}{4} \right)^n \tag{A.17}$$

gives

$$K_r(t) = \frac{1}{C_k} e^{-\alpha t} \left(\delta'(t) - \frac{\beta}{4}\delta(t) + \frac{\beta J_2\left(\sqrt{\beta t}\right)}{4t} \right) \tag{A.18}$$

Appendix B: Measuring accumulation rate from space

It is worth considering the possibility of using the relationship (3.5.7) to derive maps of accumulation rate from the altimeter data. If γ can be determined from the extinction coefficient k_e using equation (3.5.7), then equation (3.5.6) can be solved for the accumulation rate A, using $\overline{T}$ from passive microwave data and equation (3.2.2).

To support equation (3.5.7) theoretically, a Monte-Carlo simulation was performed using the scattering model described in section 3.4. Figure 3.21 shows the calculated k_e values for 100 realisations of the simulated snowpack. For each realisation, the mean grain radius as a function of depth was calculated using equation (3.5.6), with γ varied randomly between 0.001 and 0.02 $\mathrm{mm}^3\ \mathrm{m}^{-1}$ and r_0 varied between 0.2 and 0.34 mm (these ranges are given by Zwally (1977) for sites in Greenland and Antarctica with diverse locations and climates). The parameters describing the density profile were also chosen randomly within plausible ranges, so the scatter in figure 3.21 represents the likely variance from differences in density and stratification between sites.

The model predicts the functional form of the relationship (3.5.7), the degree of scatter, and the value of the intercept a fairly accurately. The gradient b obtained from the Monte-Carlo simulation is very sensitive to the distribution of grain sizes about the mean value, and this is not accurately known. In figure 3.21 the distribution was assumed lognormal with standard deviation 0.57 times the mean, giving close agreement with the observed value of b. When the standard deviation was halved, the gradient b increased by more than a factor of six. In the absence of snow stereology data to constrain the grain-size distribution, the empirical values for a and b, derived from figure 3.20, were assumed to hold in the following calculations.

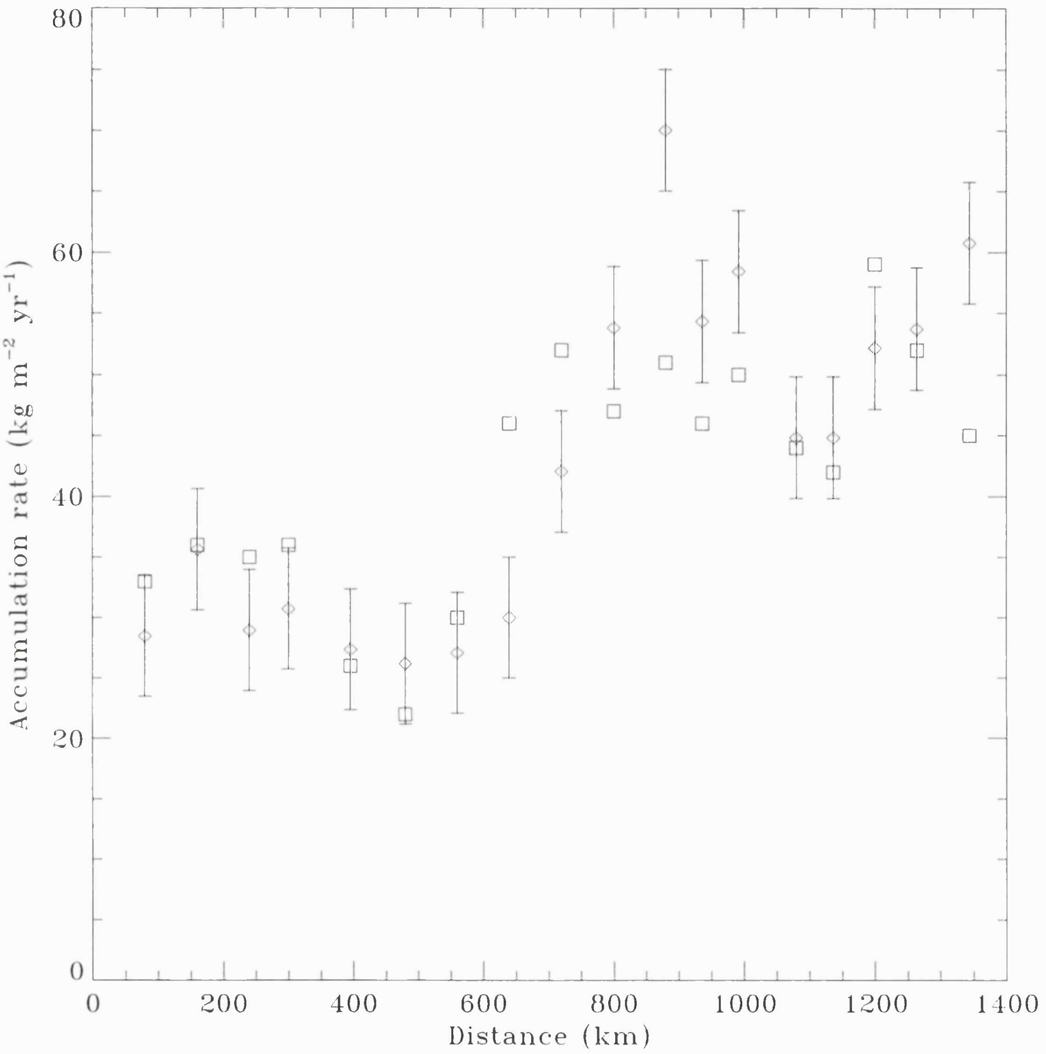

Figure B.1 The accumulation rate along the SPQMLT3 route, retrieved from the extinction coefficient and the SMMR-derived mean annual temperature (squares), compared with values measured in situ (diamonds). The latter were taken from Rundle (1971).

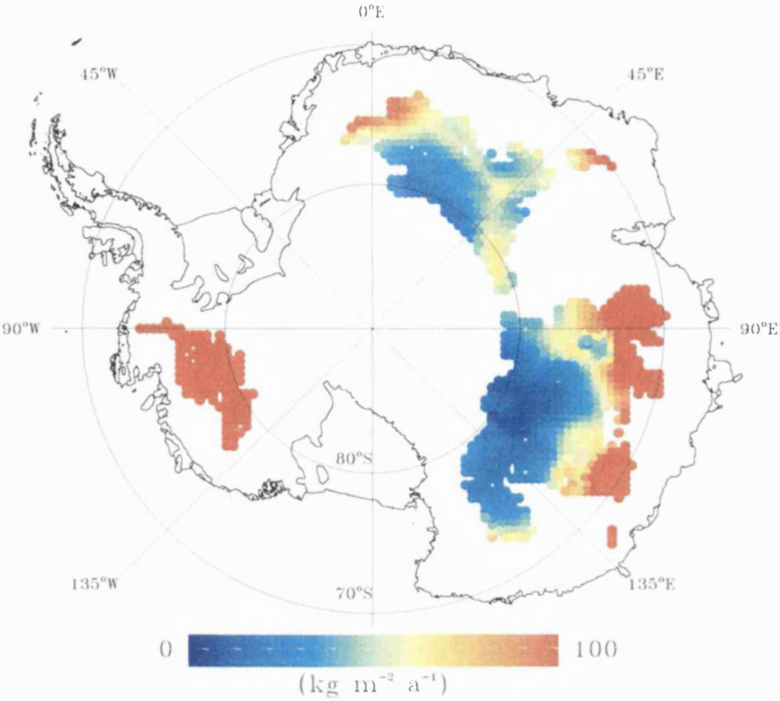

Figure B.2 Accumulation rate calculated from the extinction coefficient and the mean annual temperature derived from SMMR 6.6 GHz data. Values in West Antarctica are unreliable because of echo distortions caused by the undulating topography.

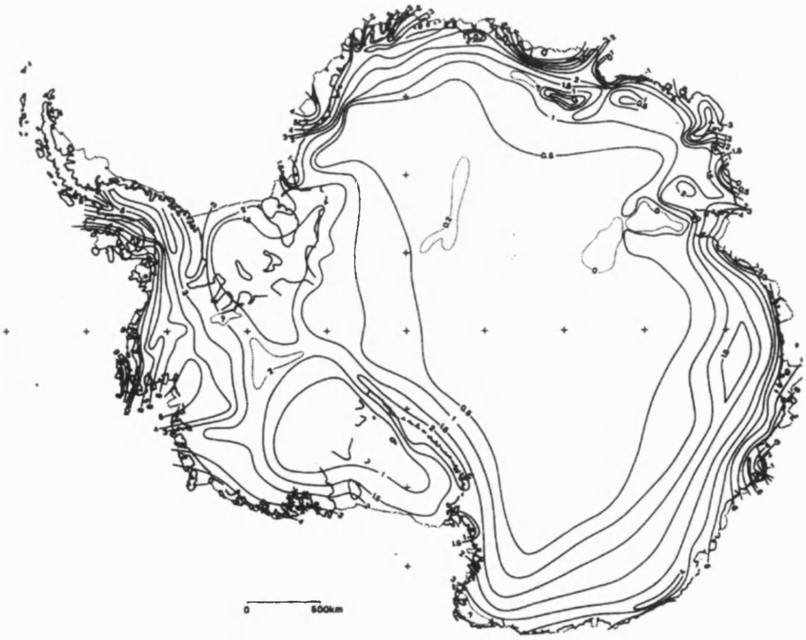

Figure B.3 Accumulation rate from direct glaciological observations. From (Giovinetto and Bentley 1985).

Figure B.1 compares the satellite and ground based measurements of accumulation rate along the SPQMLT3 route. Figure B.2 shows the satellite derived accumulation rate for the 1195 sites where k_e values were retrieved, while figure B.3 shows the contours obtained from direct glaciological observations. There is a general agreement between the satellite derived values and the ground based measurements, although discrepancies do exist. The satellite derived values in West Antarctica are too high, but it is known from section 3.4 that values of k_e there are underestimated because the echoes are heavily distorted by the undulating topography.

If this method is to be employed, k_e must be measured more accurately in regions where topography causes the function J to depart from Gaussian. This would allow the method to be extended to the margins of the ice sheet, and even in the flatter regions, it would remove the largest source of error in measurements of k_e.

The observation that $\sigma^{\circ}_{\mathrm{surf}}$ varies temporally, while $\sigma^{\circ}_{\mathrm{vol}}$ and k_e remain stable, suggests a possible approach to this problem. It was noted in section 2.5 that errors occur in undulating regions because, without a-priori information about the shape of the function J, it must be assumed Gaussian. However, the observations of section 3.4 show that the shape of J can be determined by differencing observations of deconvolutions $\tilde{r}_1$ and $\tilde{r}_2$ separated in time, provided there has been a change in $\sigma^{\circ}_{\mathrm{surf}}$. An alternative model to y defined by equation (2.4.24) is then given by

$$\tilde{r}_1(t) \approx \hat{y}\left(t; \sigma^{\circ}_{surf}, \sigma^{\circ}_{vol}, k_e, \tau_s\right) \tag{B.1}$$

where

$$\hat{y}(t) = \Delta_t \sum_{l=1}^{N_l} \tilde{s}(t - t_l)\hat{J}(t_l) \tag{B.2}$$

with $\tilde{s}$ defined by equation (2.5.11) and

$$\hat{J}(t_l;\tau_s)=\frac{\tilde{r}_2(t_l+\tau_s)-\tilde{r}_1(t_l)}{\Delta_t\sum_{i=1}^{N_l}\left(\tilde{r}_2(t_i+\tau_s)-\tilde{r}_1(t_i)\right)} \tag{B.3}$$

Equation (B.3) provides a suitably normalised estimate of J. The parameter τ_s, which accounts for any relative shift between the two deconvolutions can be estimated by minimising the norm of their difference $\Delta_t\sum_{l=1}^{N_l}\left|\tilde{r}_2(t_l+\tau_s)-\tilde{r}_1(t_l)\right|$. Having obtained τ_s, the model $\hat{y}$ can be fitted to the deconvolution $\tilde{r}_1$ to obtain $\sigma^{\text{o}}_{\text{surf}}$, $\sigma^{\text{o}}_{\text{vol}}$ and k_e. Provided that enough regions can be found where $\sigma^{\text{o}}_{\text{surf}}$ has changed between measurements, this method offers the potential to obtain a much more complete and accurate picture of accumulation patterns across Antarctica than is shown in figure B.2.

Appendix C: The constitutive relationship for snow

This appendix presents the equations and parameters which were used in equation (4.2.11) to provide the strain rate. The equations were taken from the literature of pressure sintering. Notation is as for chapter 4, except for the parameters introduced in table C.1.

It is common in sintering studies to regard the densification as taking place in three stages, each covering a different range of densities. Between stages, the arrangement of grains, the shape of pores and the permeability of the compact to air may change. For firn, stage I corresponds to densities less than $0.55\ \mathrm{kg\ m^{-3}}$, stage II the range 0.55 to $0.82\ \mathrm{kg\ m^{-3}}$, and stage III above $0.82\ \mathrm{kg\ m^{-3}}$. For each mechanism three equations are listed, one for each stage.

By considering the shear forces acting across the boundaries between approximately spherical ice grains Alley (1987) arrived at the following expression for the strain rate due to grain boundary sliding. Grain boundary sliding is assumed negligible for stages II and III because, by then, the grains are too closely packed.

$$\begin{aligned} f^{I}_{GBS} &= -\frac{16 D_{BDC} \Omega \delta_b \rho_{ice}^3}{15 k_B T h^2 r \mu^2 \rho^3} \left(1 - \frac{5\rho}{3\rho_{ice}}\right)(p - p_0) \\ f^{II}_{GBS} &= f^{III}_{GBS} = 0 \end{aligned} \tag{C.1}$$

The following expressions for dislocation creep were derived by (Wilkinson and Ashby 1975) by considering the plastic deformation of a cylindrical or spherical shell of material around the pore space.

$$f_{DC}^{II}=\frac{-2A_{DC}\left(1-\frac{\rho}{\rho_{ice}}\right)\left(\frac{2}{n}(p-p_0)\right)^n}{\left(1-\left(1-\frac{\rho}{\rho_{ice}}\right)^{1/n}\right)^n}$$

$$f_{DC}^{III}=\frac{-3A_{DC}\left(1-\frac{\rho}{\rho_{ice}}\right)\left(\frac{3}{2n}\left(p-p_0\frac{\rho(\rho_{ice}-\rho_c)}{\rho_c(\rho_{ice}-\rho)}\right)\right)^n}{2\left(1-\left(1-\frac{\rho}{\rho_{ice}}\right)^{1/n}\right)^n} \tag{C.2}$$

By solving the diffusion equation for cylindrical and spherical pore geometries (Coble 1970) arrived at the following expressions for densification by boundary diffusion and lattice diffusion.

$$f_{BD}^{II}=-\frac{37\delta_b D_{BDC}\Omega\rho_{ice}(p-p_0)}{2k_B T r^3\rho}$$

$$f_{BD}^{III}=-\frac{37\delta_b D_{BDC}\Omega}{2k_B T r^3}\left(\frac{\rho_{ice}}{\rho}(p-p_0)+p_0\left(1-\frac{\rho(\rho_{ice}-\rho_c)}{\rho_c(\rho_{ice}-\rho)}\right)\right) \tag{C.3}$$

$$f_{LD}^{III}=-\frac{10D_{LDC}\Omega\rho_{ice}(p-p_0)}{3k_B T r^2\rho}$$

$$f_{LD}^{III}=-\frac{\frac{3D_{LDC}\Omega\rho_{ice}}{\rho k_B T r^2}\left(\frac{\rho_{ice}}{\rho}(p-p_0)+p_0\left(1-\frac{\rho(\rho_{ice}-\rho_c)}{\rho_c(\rho_{ice}-\rho)}\right)\right)}{\left(\sqrt[3]{\frac{\rho_{ice}}{\rho_{ice}-\rho}}-1\right)} \tag{C.4}$$

During stage I the densification is dominated by grain boundary sliding (Alley 1987) so the choice of f_{DC}^{I}, f_{BD}^{I} and f_{LD}^{I} is not critical: the expressions presented above for f_{DC}^{II}, f_{BD}^{II} and f_{LD}^{II} were used.

Table C.1 - Parameters used in the densification model

A_{DC}	dislocation creep coefficient	$A_{DC} = B_{DC} \exp\left(-\frac{E_{DC}}{RT}\right)$
B_{DC}	pre-exponential for dislocation creep	$3.22 \times 10^{-11}\ (\mathrm{Nm}^{-2})^{-n}$
B_{BDC}	pre-exponential for boundary diffusion creep	$3.0 \times 10^{-2}\ \mathrm{m^2 s^{-1}}$
B_{LDC}	pre-exponential for lattice diffusion creep	$3.0 \times 10^{-2}\ \mathrm{m^2 s^{-1}}$
D_{BDC}	grain boundary diffusion coefficient	$D_{BDC} = B_{BDC} \exp\left(-\frac{E_{BDC}}{RT}\right)$
D_{LDC}	lattice diffusion coefficient	$D_{LDC} = B_{LDC} \exp\left(-\frac{E_{LDC}}{RT}\right)$
δ_b	width of grain boundary	$9 \times 10^{-10}\ \mathrm{m}$
E_{BDC}	activation energy for boundary diffusion	$44.1\ \mathrm{kJ\,mol^{-1}}$
E_{LDC}	activation energy for lattice diffusion	$66.2\ \mathrm{kJ\,mol^{-1}}$
E_{DC}	activation energy for dislocation creep	$74.5\ \mathrm{kJ\,mol^{-1}}$
h	size of grain boundary obstructions	$4.0 \times 10^{-6}\ \mathrm{m}$
k_B	Boltzmann's constant	$1.381 \times 10^{-23}\ \mathrm{J\,K^{-1}}$
μ	ratio of neck radius to grain radius	0.7
Ω	volume per H_2O molecule	$3.27 \times 10^{-29}\ \mathrm{m^3}$
r	grain radius	0.5 mm
R	gas constant	$8.314\ \mathrm{J\,mol^{-1}\,K^{-1}}$
ρ_c	density at moment of pore closure	0.82

Appendix D: The transformation of equations (4.2.1) - (4.2.4)

If $q(t)$ is the total weight of snow which has fallen over a time interval $[0,t]$ then

$$q(t)=\int_0^t b_s g dt' \tag{D.1}$$

where $b_s(t)$ is the accumulation rate and g is the acceleration due to gravity. If b_s(t) is strictly positive then there is a unique relationship between $q(t)$ and t. At any time t there is also a unique relationship between the depth z of a parcel of firn and the time t_0 at which it was deposited at the surface. Therefore, if $q_0 = q(t_0)$, the evolution of the firn may be described in the coordinate system (q,q_0) in place of the coordinates (z,t). This appendix describes the transformation of equations (4.2.3) and (4.2.4) into this coordinate system.

The partial derivatives in z and t may be written as follows

$$\frac{\partial}{\partial z}=\frac{\partial q}{\partial z}\frac{\partial}{\partial q}+\frac{\partial q_0}{\partial z}\frac{\partial}{\partial q_0} \tag{D.2}$$

$$\frac{\partial}{\partial t}=\frac{\partial q}{\partial t}\frac{\partial}{\partial q}+\frac{\partial q_0}{\partial t}\frac{\partial}{\partial q_0} \tag{D.3}$$

From equation (D.1)

$$\frac{\partial q}{\partial t}=b_s g \tag{D.4}$$

and

$$\frac{\partial q}{\partial z}=0 \tag{D.5}$$

Using equations (4.2.3), (4.3.3) and (D.5) gives

$$\frac{\partial q_0}{\partial z} = -\rho g \tag{D.6}$$

Substituting equations (D.4) - (D.6) into equations (D.2) and (D.3) provides

$$\frac{\partial}{\partial z} = \frac{\partial q_0}{\partial z}\frac{\partial}{\partial q_0} = -\rho g \frac{\partial}{\partial q_0} \tag{D.7}$$

and

$$\frac{\partial}{\partial t} = b_s g \frac{\partial}{\partial q} + \frac{\partial q_0}{\partial t}\frac{\partial}{\partial q_0} \tag{D.8}$$

The material derivative defined by equation (4.2.5) then becomes

$$\frac{D}{Dt} = b_s g \frac{\partial}{\partial q} + \left(\frac{\partial q_0}{\partial t} + v \frac{\partial q_0}{\partial z} \right) \frac{\partial}{\partial q_0} \tag{D.9}$$

but

$$\frac{\partial q_0}{\partial t} + v \frac{\partial q_0}{\partial z} = \frac{D q_0}{Dt} = 0 \tag{D.10}$$

which follows because the definition of q_0 requires that it is conserved along a particle path. Using equation (D.10), equation (D.9) becomes

$$\frac{D}{Dt} = b_s g \frac{\partial}{\partial q} \tag{D.11}$$

Substituting equations (D.7), (D.8) and (D.11) into equations (4.2.3) and (4.2.4) provides the transformed equations (4.3.4) and (4.3.5)